# TRANSIENT LASER ANNEALING OF ZINC OXIDE NANOPARTICLE INKS TO FABRICATE ZNO THIN FILM TRANSISTORS

A Dissertation

Presented to the Faculty of the Graduate School

of Cornell University

in Partial Fulfillment of the Requirements for the Degree of

Doctor of Philosophy

by

Michael Willemann

May 2013

TRANSIENT LASER ANNEALING OF ZINC OXIDE NANOPARTICLE INKS TO FABRICATE ZNO THIN FILM TRANSISTORS

Michael Willemann, Ph.D.

Cornell University 2013

Display technology, which relies exclusively on amorphous silicon as the active material for driver electronics, has reached multiple impasses that limit future progress. In order to deliver higher resolutions, higher refresh rates, new display technologies, and innovative form factors, driver electronics must transition to higher performance materials like amorphous oxide semiconductors (AOSs). Transient laser annealing offers an attractive means to maximize performance while minimizing thermal budget, making it compatible with flexible back plane materials and roll-to-roll processing. This research investigates the deposition and annealing of zinc oxide nanoparticle inks to form fully densified crystalline and amorphous zinc oxide films. Processing routes for nanoparticle annealing, including ligand removal, calcining, and excimer pulse laser sintering on the nanosecond time scale, will be introduced that minimize defect formation and suppress the anomalous n-conductivity which is a major challenge to zinc oxide processing. Resistivities as high as $6 \times 10^7$ Ω-cm have been demonstrated. Laser processing on longer millisecond time scales can control defect formation to produce ZnO films without extrinsic doping which have low resistivity for intrinsic oxides, in the range of $10^{-1} - 10^{-2}$ Ω-cm. Finally, a viable process for the production of backgated ZnO transistors with promising characteristics is presented and the future implications for AOSs and transient thermal processing will be discussed.

## BIOGRAPHICAL SKETCH

Michael Willemann was born on June 21, 1983 in Fairfax, Virginia, the first child of Paul and Deborah Willemann. He was joined shortly after by two younger twin brothers, Jeffery and Thomas, who have benefited greatly from his sagacious advice and tutelage over the years. The author does not have a peer-reviewed reference for this particular statement but feels that it is generally known and accepted.

Michael showed an early aptitude for annoying questions and creative destruction. Among his many victims were household appliances, power tools, and shiny things. Though his parents were supportive of his inquisitiveness, they found that discussions regarding circuit breakers, safety features, and instruction manuals were often too late. Surprisingly enough, Michael escaped his young childhood without electrocution, burning, drowning, or serious maiming.

His primary and secondary educations were completed at Martin Luther King Elementary School, Saunders Middle School, and Hylton Senior High School in Woodbridge, Virginia. There, he developed a keen interest in science and technology, so he decided to pursue an engineering degree at Virginia Tech. In his five years at Virginia Tech, he experienced a broad range of disciplines, finally deciding (under threat of never graduating) on the Department of Materials Science and Engineering. The department, along with the Hillcrest Honors Community, became his home away from home and he greatly enjoyed his time at Virginia Tech.

After graduation, Michael received a year-long Fulbright Fellowship to Germany, at the RWTH-Aachen and Forschungszentrum Jülich. There, he solidified his interest in advanced semiconductor devices and technology. After

his year abroad, he came to Cornell University and began study in the lab of Professor Michael Thompson, primarily because he was promised he would be allowed to shoot things with many Class IV lasers. Five years later and hopefully a little wiser, he departs Cornell with a strong foundation in semiconductor processing and the desire to pursue a career in semiconductor technology development.

To my Family and Friends,

For their love, support, & sacrifice over the many years of this endeavor

## ACKNOWLEDGEMENTS

The completion of this thesis would have been impossible without the help and support of many others. The words in this space are poor compensation for all they have given, but hopefully they understand their contributions have meant more to me than I can express.

First and foremost, to my advisor, Professor Michael Thompson, his teaching and his input have been invaluable to my five years at Cornell. His patience and enthusiasm have seen me through many bumps on the road to this goal, and I greatly appreciate his contributions to making the research and this document possible.

Secondly, thanks to my committee, Professors Emmanuel Giannelis and Michael Spencer, and the rest of the faculty of the department. Their suggestions, insight, and energy have enriched my experience at Cornell. I feel truly lucky to have had the opportunity to learn from such a gifted and dedicated faculty.

Many thanks are due to the members of the Thompson group: Alan, Bob, and most of all Byungki. They have been sources of sound advice, stalwart friendship, and good humor. I wish them all the best of luck. Bob - may you continue to meet interesting people with even stranger stories. Alan - may you never build a custom laser system ever again. Byungki - over the years, you were vital to making the day to day lab work seem lighter. Thanks for being there. May you go on to do great things and relocate to a place in closer proximity to a KFC.

I also want to thank my parents, to whom I owe more than I will ever know. Their effort and sacrifices over many years made this all possible. The values and lessons they taught me from day one have shaped the person I am

and allowed me to accomplish the things that I have.

And finally to Kari, for reasons I will never fully understand, has stuck with me and supported me through research, writing, and defending. All the more the amazing, she was writing and defending her thesis at the same time. Her strength and perseverance have been gifts for which I will never be able to thank her enough. Her constant encouragement has seen me through this long process, and I will treasure her for it always.

## TABLE OF CONTENTS

## LIST OF TABLES

## LIST OF FIGURES

CHAPTER 1

# INTRODUCTION

## 1.1 Flexible Display Electronics

Flexible electronics and displays have long been the purview of science fiction, but developments in the past decade have moved flexible electronics to a rapidly developing reality. In addition to the inherent uniqueness, compactness, and robustness of the display form factor, flexible substrates also create unique opportunities to reduce cost per area by introducing fabrication methods that take advantage of continuous, rather than batch, processing over large areas. Enabling technologies such as organic semiconductors, electrophoretic displays, light emitting diodes, barrier layers, and large scale roll-to-roll processing equipment have emerged. Despite these advances, fast, high resolution, and reliable flexible displays have remained elusive. The most likely candidates for such displays are active-matrix organic light emitting diode (AMOLED) displays because of their inherent flexibility, relatively simple structure, fast response times, good color accuracy, and wide viewing angle. The primary impediment to such displays is poor display driver electronics. In order to be viable, flexible AMOLED displays require thin film transistor (TFT) drivers with high yield, uniformity, fill-factor, current density, and stability. Unfortunately, current display technologies cannot meet all of the stringent requirements imposed by such displays. However, several recent developments in semiconductor materials and processing have brought scalable, high-performance flexible display closer to reality.

The form factor, processing, and functionality of flexible electronics and

displays begin with the substrate the devices are placed on (also known as the backplane). Proposed substrates include stainless steel (SS) foils, ultra-thin coated glass, polyethylene terephthalate (PET), polyethylene naphthalate (PEN), polyethersulfone (PES), and polyimide (PI). Their relevant physical properties are listed in Table 1.1. There are several unique constraints presented by the use of flexible substrates. Flexible substrates, by definition, bend and flex; the surfaces are not flat, and the thickness can vary widely. In use, the flexible electronic displays would be subjected to large normal and shear strains, so the materials must be mechanically robust. In addition to its mechanical strength, an ideal substrate would also be resistant to various solvents and enviromental chemicals found in fabrication and use. Stainless steel offers excellent thermal properties with high maximum use temperature and low coefficient of thermal expansion (CTE), but it is opaque and can have very poor surface characteristics. Ultra thin glass sheets are attractive because of their excellent thermal properties and previous process knowledge gained by making liquid-crystal display (LCD) panels could be leveraged. However, despite recent improvements to the glass coatings that have reduced defects associated with cracking and fracture, glass is still a relatively brittle material that is only marginally flexible. Polymers generally offer excellent optical properties and mechanical properties associated with flexibility, but they have very poor thermal performance. Polyesters such as PET and PEN cannot be processed above 150°C and 200°C, respectively. Polyimide can tolerate a relatively high processing temperature as compared to most polymers, but this must be balanced against its poor optical properties and high permeability to water.[11]

Virtually all commercial displays rely on amorphous silicon (a-Si) for driver electronics, but the low carrier mobility and instability under high cur-

Table 1.1: Physical properties of potential flexible substrates. Silicon is included for reference. *Transmission refers to light transmission in the visible spectrum (400-700 nm).[11]

| Material | Max.Temp. (°C) | CTE (ppm/°C) | Transmission (%)* | $H_2O$ Abs. (wt%) | Modulus (GPa) |
|---|---|---|---|---|---|
| SS | 900 | 17 | negligible | negligible | 190 |
| Glass | 600 | 3.7 | >90 | negligible | 64 |
| PET | 150 | 15 | >85 | 0.14 | 5.3 |
| PEN | 200 | 13 | >85 | 0.14 | 6.1 |
| PES | 220 | 54 | 90 | 1.4 | 2.2 |
| PI | 360 | 17 | varies | 1.8 | 2.5 |
| Silicon | 1400 | 3.0 | negligible | negligible | 150 |

rent load limit the technology in future applications. Amorphous silicon has a carrier mobility of approximately 1 $cm^2$/V-s, but direct drive of OLED devices require a carrier mobility in excess of 4 $cm^2$/V-s. In contrast to current LCDs, the brightness of the pixels on an LED display is directly proportional to the DC current drive.[18] After approximately 1000 hours under DC bias, a standard a-Si TFT will lose half of its output current in saturation, corresponding to a similar fractional loss in display brightness, as shown in Figure 1.1. This is not an acceptable lifetime for devices that are expected to last on the order of five to ten years. In order to extend the functionality of the current technology, efforts to recrystallize a-Si to form poly-crystalline silicon on low temperature substrates have yielded promising results.[13] An alternate path that still utilizes traditional silicon implant technology allows single or poly crystalline silicon devices to be fabricated on rigid substrates and subsequently released and transferred to flexible substrates.[55] These methods, while successful, are

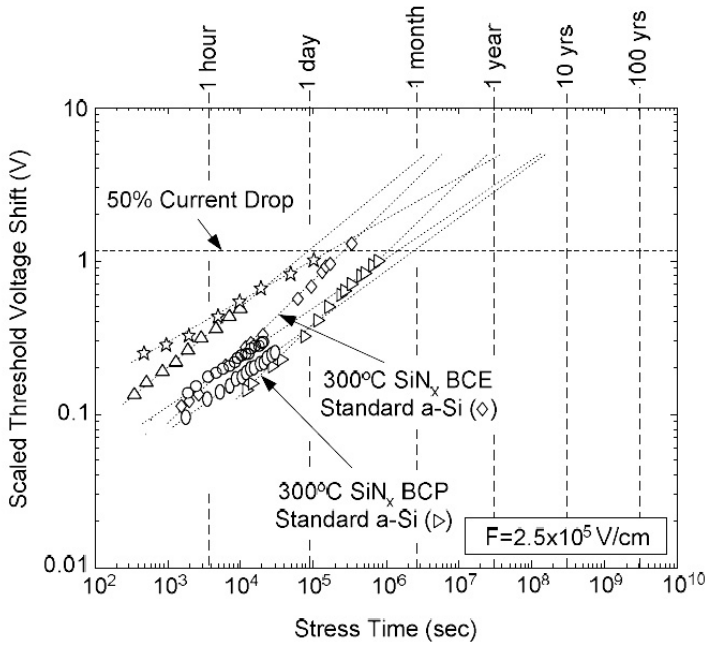


Figure 1.1: Threshold voltage shift as a function of DC bias stress time for standard a-Si transistors[18]

technically difficult and economically unfeasible to scale up.

Because they are inherently scalable and flexible, organic semiconductors have also been implemented as driver electronics. Due to the polymer chemistry required to make delocalized electron states sufficient to conduct charge, organic semiconductors are susceptible to degradation by oxygen and ultraviolet exposure. Additionally, the low work function contact metals required for efficient ohmic contacts to n-doped regions are also air and water reactive. Therefore, elaborate barrier layers are necessary to protect the devices and ensure long lifetimes.[11] Additionally, the carrier mobilities for organic electronics have remained stubbornly low. Despite more than a decade in development, the maximum carrier mobility for common classes of semiconducting polymers has stagnated, as shown in Figure 1.2.[39] Solution-processed pentacene, one of

the highest performance organic semiconductors, has transport properties comparable to a-Si, but other common organic electronics fair worse. Despite extensive efforts by many groups, concerns remain regarding processing, environmental stability, carrier mobility, and the maximum current density of organic electronics.

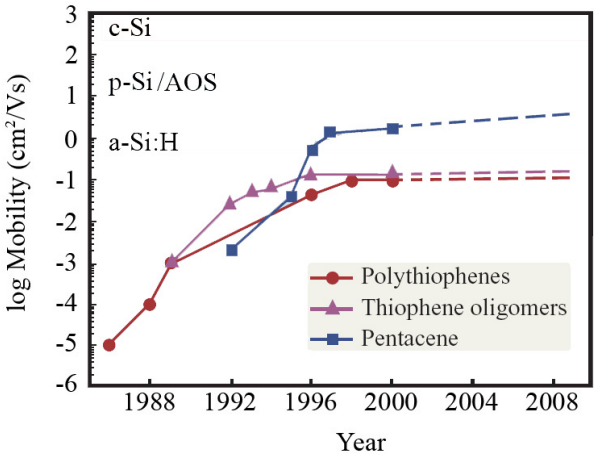


Figure 1.2: Graph of mobility versus year showing the development of pentacene and polythiophene organic semiconductors as compared to silicon technologies. Organic electronic performance continues to lag polycrystalline and crystalline silicon.[39]

Recently, amorphous transition metal oxides (AOSs) have been investigated extensively as a potential replacement for amorphous silicon. They have been shown to exhibit high carrier mobility and current density, in addition to uniformity and excellent environmental stability. Generally, the amorphous transition metal oxides include binary or ternary compositions of the oxides of zinc, indium, gallium, or tin, with the most common composition in literature being $InZnGaO_4$. In contrast to silicon, which has three orders of magnitude difference between the carrier mobility of the crystalline versus the amorphous phase, AOSs have carrier mobilities of 1%-10% of their crystalline

counterparts.[29] As the silicon conduction band is a $sp^3$ hybridized orbital, carrier density has strong directional dependence, hence the disruptions to regular crystalline order found in a-Si cause severe degradation of performance. Conversely, the conduction bands in AOSs are symmetric with respect to zone center because their conduction bands have a non-directional s-type character. As a result, AOSs retain more of the performance characteristics of their crystalline analogs. The tight binding model (Figure 1.3) predicts that the anti-bonding orbitals that make up the conduction band would have a character more like the s-orbital of the metal cation. Because of the less directional, ionic character of

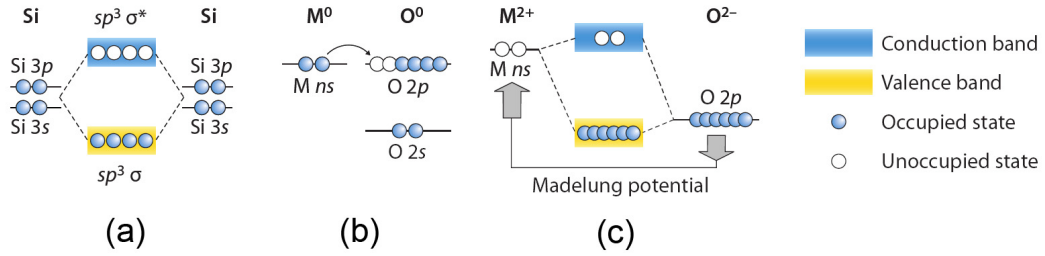


Figure 1.3: Tight-binding band schematic of silicon (a) and metal oxide semiconductor (b) & (c) illustrating the band splitting that creates the valance and conduction band of each.[29]

the bonds in AOSs, they are also inherently less susceptible to the formation of DC bias stress defects found in a-Si devices. Momentum transfer from carriers alters the overlap of the energy levels and reduces the performance of materials with strongly directional conduction bands, like a-Si. Most of the AOSs being investigated are wide band gap semiconductors which provide additional stability from hot carriers, breakdown, and short channel effects. Depending on the exact composition, AOSs can have excellent selectivity and etching characteristics compatible with processes already found in a-Si processing.

Despite all of the advantages, there are several challenges involved in fabricating flexible display drivers from AOSs which will be dealt with in later sections. These challenges include scalable deposition processing, post-deposition annealing, controlling charged oxygen vacancy concentration, and forming ohmic contacts. While most commerically interesting AOSs contain at least a binary metal oxide, we will focus primarily on the implications for zinc oxide, which is a well-characterized semiconductor in its own right, but also a primary component in many of the commerically interesting AOSs.

## 1.2 Research Goals

The goal of this research was to utilize crystalline ZnO nanoparticles as a precursor for active layers in thin film transistors (TFTs) on flexible substrates. Nanoparticles were synthesized via two different methods to evaluate their suitability for transient laser annealing. Deposition methods, including spin casting and electrophoretic deposition, were employed to fabricate green nanoparticle films. The green films were sintered into densified polycrystalline and amorphous thin films using transient laser annealing processes, including melt and non-melt annealing. The resulting films were characterized by scanning electron microscopy, x-ray diffraction, Fourier transform infrared spectroscopy, and electrical measurements to understand the effects of laser annealing on zinc oxide as a possible prototype system of the more general class of AOS materials. The films were integrated with a traditional lithographic process to form TFTs, and their electrical properties were measured also.

CHAPTER 2

# ZINC OXIDE FILMS: PROPERTIES AND PREPARATION

## 2.1 Properties of Zinc Oxide

Zinc oxide (ZnO) is a ubiquitous material used in a variety of industries. It is used extensively as an additive to increase UV resistance, as an anti-bacterial agent, and as a white pigment. Primarily sourced from the mineral zincite, it is non-toxic, air stable, and abundant. It is of specific interest to the electronics industry because of its large bandgap, high intrinsic mobility, transparency, and piezoelectricity.[19] It is a major constituent of the amorphous oxide semiconductors (AOSs) being studied to replace amorphous silicon (a-Si). Despite these interesting properties, ZnO also has a number of drawbacks that have limited its use in semiconductor applications in the past.

### 2.1.1 Structural Properties

Zinc oxide has only one stable allotrope at 1 bar of pressure, a hexagonal wurtzite phase, space group $P6_3mc$. This is in contrast to many common group IV and group III-V semiconductors, which are cubic, usually diamond or zincblende. The ZnO structure is shown in Figure 2.1. Experimental consensus via high resolution x-ray crystallography has shown that the lattice constants are $a$ = 0.325 nm and $c$ = 0.520 nm, for an a/c ratio of 1.60. This is slightly less than the mathematical ideal for wurtzite, 1.633. The structure is thermodynamically stable from cryogenic temperatures up to the decomposition temperature of approximately 1800°C.[44] Zincblende phases of ZnO have been reported, but

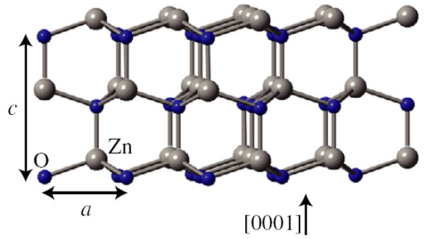


Figure 2.1: Hexagonal wurtzite crystal structure of ZnO.[44]

they are stabilized by being epitaxially grown on a cubic substrate. Amorphous ZnO forms readily at room temperature when deposited with physical vapor deposition techniques. However, the driving force for crystallization is so great that any post-deposition heat treatment in excess of 150°C causes spontaneous crystallization. The mechanical properties of ZnO compare favorably to other semiconductors. Its modulus of elasticity is 112 GPa, slightly less than that of silicon (150 GPa) but slightly more than that of gallium arsenide (86 GPa). Its linear expansion coefficient, reported in the range of $4.3-5.7$ ppm/K, is roughly equivalent to gallium arsenide and silicon.[44]

### 2.1.2 Electronic Properties

As mentioned previously, ZnO has a direct band gap of $3.1-3.3$eV, classifying it as a wide bandgap semiconductor. Its calculated energy band diagram with respect to the zone center is shown in Figure 2.2. As with most compound semiconductors, its electronic transport properties are dominated by charged defects. Despite decades of effort to produce a verifiable and reliable p-dopant for ZnO, none has been forthcoming. In a perfect undoped single crystal, the free carrier concentration would be effectively zero, based on the large bandgap.

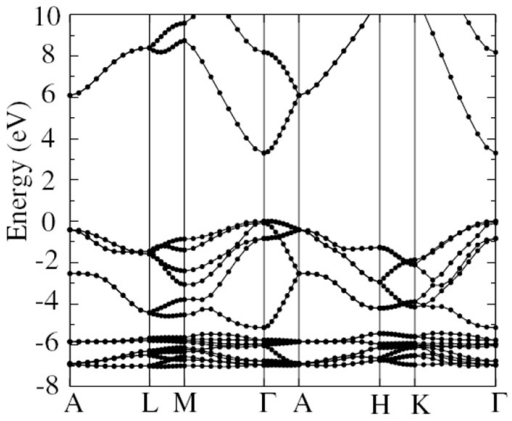


Figure 2.2: Calculated band diagram of ZnO using HSE hybrid functional theory, showing the large, direct bandgap at the zone center.[26]

However, virtually all measured samples are n-doped, and the values for electron concentration can vary as much as ten orders of magnitude depending on processing conditions. As purer crystals were fabricated in the 1970s and 1980s, the defect primarily responsible for the anomolous n-conductivity was narrowed to two possibilities: intrinsic oxygen vacancies or zinc interstitials, based data on similar to that shown in Figure 2.3. The conductivity of ZnO is almost an order of magnitude higher than one would expect based on intrinsic, thermally excited carriers.[26] The defects would be in a thermodynamic equilibrium with the ambient oxygen partial pressure and would exhibit similar same rate constants[62]:

$$\mathrm{Zn}_{Zn}\mathrm{O}_O \rightleftarrows \mathrm{Zn}_i + \frac{1}{2}\mathrm{O}_2(gas) \tag{2.1}$$

or

$$\mathrm{Zn}_{Zn}\mathrm{O}_O \rightleftarrows \mathrm{Zn}_{Zn} + \mathrm{V}_O + \frac{1}{2}\mathrm{O}_2(gas) \tag{2.2}$$

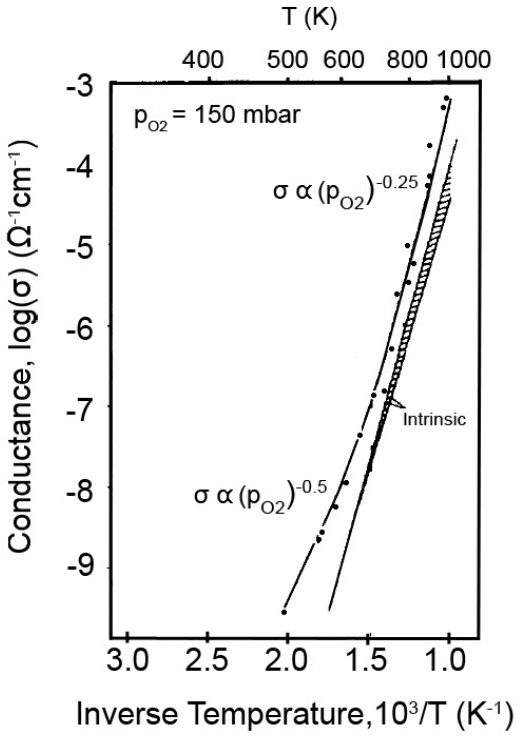


Figure 2.3: Conductivity versus inverse temperature for ZnO. The conductivity varies over six orders of magnitude from room temperature to 1000 K.[62]

While the extrapolated line in Figure 2.3 follows the rate law established by equations 2.1 and 2.2, the data seem to indicate a deviation to a different mechanism at temperatures above 600 K.

Electron spin resonance (ESR) is one of the few techniques available to probe for the unpaired electrons that might indicate which mechanism is dominant. Because the results have been conflicting and difficult to interpret, there has been no consensus on the interpretation of the data. Theoretical work using density functional theory (DFT) have also been difficult to interpret because many implementations do not even accurately predict the bandgap of ZnO, so placing the formation energy of the defects in reference to the band edge

is suspect. Adding to this controversy, Janotti and Van de Waale have published hybrid DFT results that accurately predict the band gap of ZnO. Their results, however, predicts formation energies for these defects, while still lower than all of the other intrinsic defects, are too high to meaningfully contribute to the observed n-type conductivity.[26] The calculated predictions are presented in Figure 2.4. They claim these mechanisms only become operative as compensating mechanisms for p-type defects that may be present. Their assertion is that the anomalous n-type conductivity is caused by hydrogen acting as an n-dopant. Hydrogen is present in high concentrations in virtually every deposition and annealing technique, it diffuses very quickly at deposition and annealing temperatures, and is not readily detected by analytical techniques such as secondary ion mass spectroscopy (SIMS) and X-ray photoelectron spectroscopy (XPS) because of its low atomic weight. Suffice to say, the issue of the source of the n-type conductivity remains an open question.

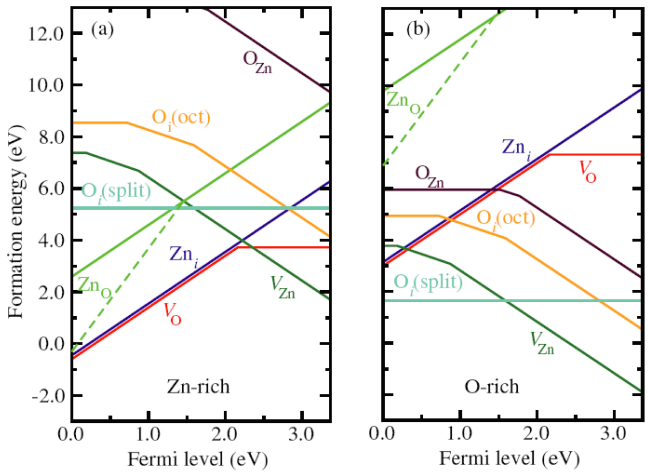


Figure 2.4: Formation energies of intrinsic defects in ZnO, calculated by a hybrid DFT method.[26]

Without a clear fundemental understanding of the source of the

anomolous n-doping in ZnO, it is difficult to address with direct migitation measures. However, minimizing time at temperature in reducing enviroments, or conversely maintaining an oxidizing environment during deposition and subsequent processing has been shown to be critical to device performance.

## 2.2 Thin Film Deposition

Deposition refers to any process that builds up material on an underlying substrate. In modern semiconductor processing, deposition is dominated by two broad types: physical vapor deposition and chemical vapor deposition. In many cases, these techniques have been successfully adapted to flexible substrates, but the adaptation requires increased complexity and infrastructure. These methods do not take advantage of the innately flexible nature of the substrate; instead, they attempt to make a flexible substrate function like a conventional rigid substrate. An alternative paradigm would be to leverage an existing additive technology that is already used at the manufacturing scale on flexible substrates. The logical choice is the printing industry, which has spent decades optimizing for throughput, registration between different layers, and image resolution on paper. Despite the natural parallels, there are several technical challenges. The additive media in printing, various dyes and inks, are typically small organic molecules dissolved in a solvent. In order to be useful in making high performance flexible electronics, printing must be able to deposit high-performance inorganic materials, including metals, insulators, and semiconductors.

### 2.2.1 Physical and Chemical Vapor Deposition

Physical vapor deposition (PVD) and chemical vapor deposition (CVD) are two broad classes of deposition processes traditionally used in semiconductor fabrication. The two are distinguished by how the thin film material is transported from the source to the substrate. As the name would suggest, PVD employs purely physical processes, such as evaporation, ion bombardment, or laser ablation to remove material from the source and deposit it on the substrate. The source and the deposited film generally have the same composition, but may have different structures.

In evaporation, the source material is heated in high vacuum, and atoms are vaporized in a controlled way from the source. The atoms ballistically traverse the distance between the source and the substrate where they adsorb onto the surface. Evaporation systems produce extremely high purity films and the incident atoms have comparatively little energy; consequently, the risk of substrate damage is minimal. Furthermore, growth can be monitored in situ via numerous methods, like quartz crystal microbalances or reflection high energy electron diffraction (RHEED). However, the drawbacks to evaporation systems are substantial. Because the deposition is done in high vacuum and relies on direct line-of-sight with the source, throughput is extremely limited, particularly for large substrates. Furthermore, refractory metals, ceramics, and multicomponent sources are difficult to evaporate. While an excellent research tool, evaporation systems have limited commercial viability. Pulsed laser deposition (PLD) solves some of the problems of evaporation by using a high power laser in short pulses, rather than a heat source, to ablate material off the surface of the target. Because the removal from the target is no longer a function of temper-

ature, refractory materials are more readily deposited by PLD as compared to evaporation. Additionally, PLD ablates a miniscule fixed volume per pulse, so the deposited film is uniform in composition and no component is preferentially evaporated. These features have made PLD popular for depositing complex oxides and carbides, but the throughput issues remain, making its commercial viability limited as well.[43]

By far, the most common PVD process is sputtering. There are several different varieties based on the geometry of the applied electric and magnetic fields, but the operating principle is shared. Inert gas, usually argon, is introduced into a vacuum chamber at a pressure in the range of several millitorr. A plasma is struck using a strong electric field, stripping the argon atoms of their valence electrons and accelerating the ions toward the target material. Upon impact with the target, the argon ions dislodge target atoms. After a series of complex collisions in the gas phase, the neutral target atoms are deposited onto the substrate to form the film. Because the mean free path is short during sputtering, the gas phase collisions cause the atoms to arrive with a range of incident angles to the substrate, improving step coverage and uniformity. The two main types of sputtering are direct current (DC) and radio frequency (RF). The type is primarily dictated by whether the target material is conductive or nonconductive. For conductive targets, DC sputtering is preferred because it yields higher deposition rates and is more straightforward. Electrically insulating targets require RF sputtering because the oscillating electric field can maintain the plasma without charging the target, which would reduce sputtering yield. As Figure 2.5 shows, there are only minor physical differences between the two configurations, and they can be done in the same chamber.[43]

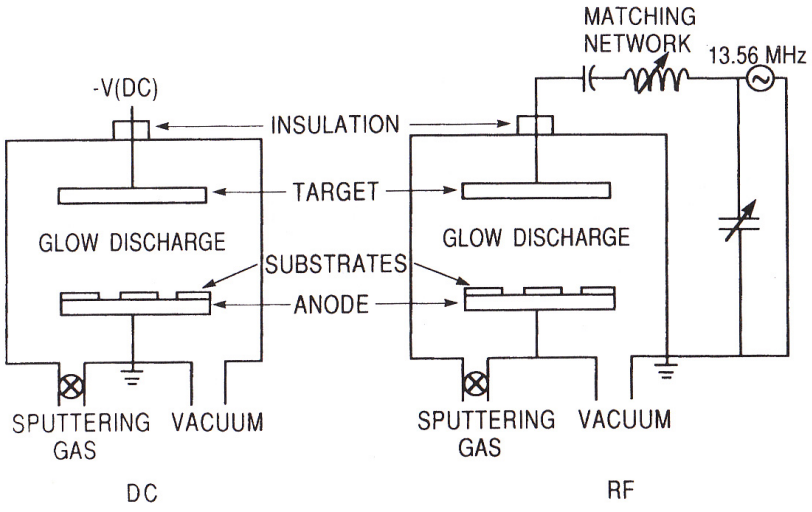


Figure 2.5: Schematic of DC (left) and RF (right) sputtering system, illustrating the primary functional components.[43]

Not only is sputtering more consistent and uniform as compared to evaporation and PLD, it is also more scalable than either of the technologies. Depending on the application, extremely high deposition rates have been achieved with acceptable film characteristics. However, sputtered films generally have more impurities and particle inclusions because the chamber is not at high vacuum. Furthermore, the high incident energy of the sputtered atoms can cause substrate damage under certain conditions. Because of its scalability, sputtering has been adapted for flexible electronic manufacturing. The planer magnetron configuration is used to generate a uniform line of deposition perpendicular to the direction of travel, and the web is spooled past at a set rate to achieve the necessary thickness, as depicted in Figure 2.6. While this method has been demostrated and is quite successful with webs up to a meter wide, it is only a semi-continuous process because the webs must be loaded and unloaded. During the load process the entire web handling system and sputtering chambers must be evacuated to base pressure. Both steps reduce throughput, and repre-

sent a bottleneck in the fabrication process.

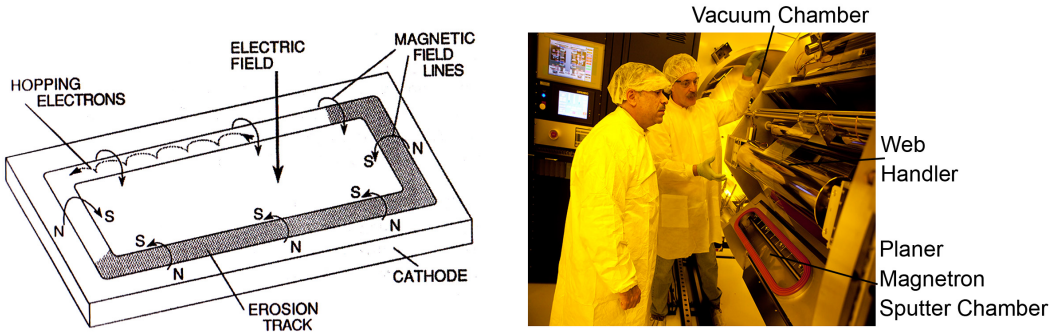


Figure 2.6: Planer magnetron sputtering target at the Center for Advanced Microelectronics Manufacturing (CAMM)[43]

In CVD, the source materials have different compositions from the final deposited film. The precursors are designed to react chemically in the gas phase or on the substrate to form the desired film, while the other chemical products are volatilized and removed. Today, a large catalog of extremely high-purity source materials is available. If one source does not work at a target temperature or pressure, there are several other possible halogens, hydrides, alkyls, or oxy-alkyls that may work. Mass flow controllers allow for precise control of the chamber conditions. While numerous variations of CVD exist, the two most common in electronics manufacturing are low-pressure chemical vapor deposition (LPCVD) and plasma enhanced chemical vapor deposition (PECVD). As a workhorse process of front-end-of-line (FEOL) semiconductor manufacturing, LPCVD generates the highest quality epitaxial and polycrystalline thin films. The chamber pressure is kept low (1-10 mtorr) to maximize mass transport and minimize contamination, so substrates can be densely packed in the furnace. Some of the common thin film LPCVD processes are listed in Table 2.1, along with examples of precursor gases and process temperatures.

Table 2.1: Common LPCVD and PECVD materials along with chemical precursors and approximate deposition temperature range.[43]

| **Process** | **Material** | **Precursors** | **Temperature (°C)** |
|---|---|---|---|
| LPCVD | c-Si | $SiCl_4$, $SiCl_2H_2$ | 1050-1200 |
| | p-Si | $SiH_4$+$H_2$ | 600-700 |
| | $Al_2O_2$ | $AlCl_3$, $CO_2$,$H_2$ | 850-1100 |
| | $SiO_2$ | $SiH_4$ + $O_2$ | 400-500 |
| | $Si_3N_4$ | $SiCl_2H_2$ + $NH_3$ | 750 |
| | $TiO_2$ | $Ti(OC_2H_5)_4$+$O_2$ | 1000 |
| | TiN | $TiCl_4$, $N_2$, $H_2$ | 1000 |
| PECVD | p-Si | $SiH_4$+$H_2$ | 400-600 |
| | a-Si | $SiH_4$+$H_2$ | 300-400 |
| | $Al_2O_3$ | $AlCl_3$+$O_2$ | 100-400 |
| | $SiO_2$ | $SiCl_4$+O2 | 100-400 |
| | $TiO_2$ | $TiCl_4$+$O_2$ | 100-500 |
| | $Si_3N_4$ | $SiCl_4$+ $NH_3$+$N_2$ | 25-500 |
| | TiN | $TiCL_4$+$N_2$+$H_2$ | 100-500 |

LPCVD relies exclusively on heat to activate the chemical reactions and is necessarily done at high temperature. It is not conducive for depositions on back-end-of-line (BEOL) processes or processes done on heat sensitive substrates. In order to extend the utility of the CVD techniques, PECVD was developed. The plasma in the reaction chamber provides additional activation energy which fractures precursor molecules into meta-stable species suitable for deposition at much lower temperatures. PECVD is routinely used for dielectrics on low temperature flexible substrates. Several PECVD processes are listed in Table 2.1 along with their corresponding precursors and process temperatures.

Like sputtering, PECVD also has its drawbacks when scaled to deposit on a roll-to-roll line. Because the PECVD needs a controlled atmosphere, it is a semi-continuous process and throughput is reduced. Additionally, PECVD is a dynamic process with complex gas flows, component mixing, and fluid boundary layers, any of which can dominate mass transport or affect growth parameters. As such, a continuously spooling web causes significant complications to operation and modeling. While plasma enhancement dramatically reduces the process temperature required, films of sufficient quality can not be obtained at the maximum use temperature for some materials. Additionally, the plasma can cause substrate damage.[43]

While traditional semiconductor deposition methods have successfully been adapted to deposit thin film flexible substrates, they are less than ideal for commercial applications. Due to the complex and variable geometry of the surface and the high demands on throughput imposed by continuous roll-to-roll processing, different paradigms for deposition have been explored.

### 2.2.2 Nanoparticle Inks and Ink Transfer Processes

As alluded to in the introduction to the section, ink transfer processes appropriated from the printing industry have had success in being modified to fabricate electronic devices on flexible substrates. One of the prerequisites for these techniques is incorporating high quality inorganic materials into stable solvent suspensions. The enabling technology was the solution-based synthesis of inorganic nanoparticles. This allowed for the creation of high purity, crystalline particles less than 100 nm in diameter. As techniques have improved

and the catalog of reactants has grown, it is now possible to create a wide variety of chemical compositions and morphologies. In order to hold these particles in suspension and study their properties, the field also developed ligand chemistries that would ionically or covalently bind to the surface of a particle (as in Figure 2.7), creating an ionic or steric repulsion between the particles that is robust and can suspend very high solids concentrations without additional dispersants.

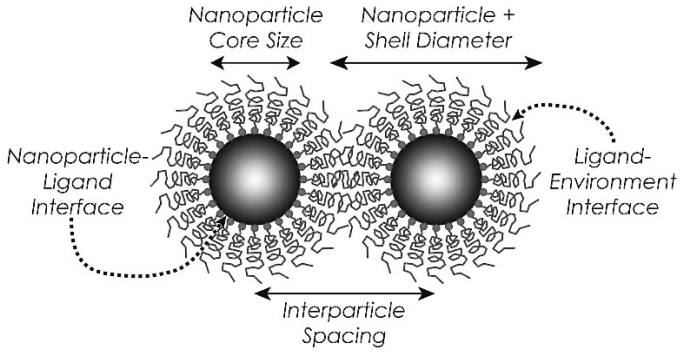


Figure 2.7: Schematic of nanoparticle-ligand interactions and interfaces. Steric or ionic interactions, alone or in concert, improve nanoparticle suspension stability.[49]

The first successful inks used in microfabrication were silver and gold nanoparticles.[12] [25] The applications were first demonstrated in 2002 by the Jacobsen group at MIT by creating a micromechanical motor (Figure 2.8).[12] Initially the material quality (in comparison to bulk material) and pattern fidelity were relatively poor, but improved source materials, thermal annealing, and ink control have allowed current state-of-the-art printing of lines at less than 20 microns.[33] The technique has been demonstrated on a variety of substrates, including silicon, glass, polyimide, and photo paper. Applications for the devices fabricated using nanoparticle inks have also expanded to included micro-electromechanical systems (MEMS), sensors, radio-frequency identifica-

tion (RFID) antennas, electrodes, and packaging interconnects.[11] For reasons that will become clear, applications have primarily been focused on conducting lines.

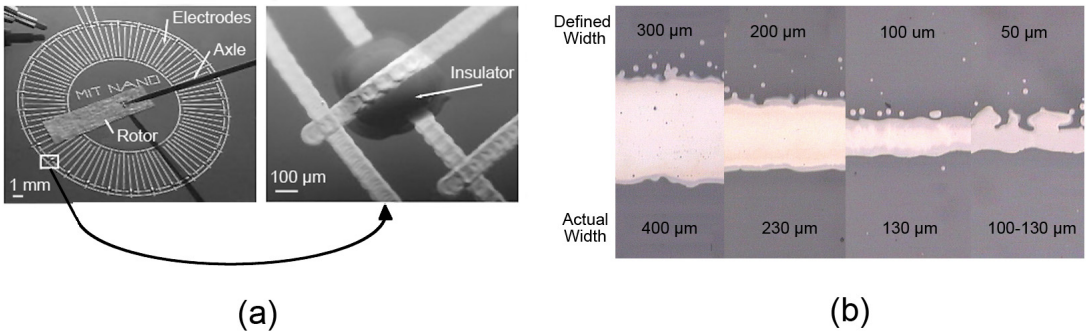


Figure 2.8: Silver nanoparticle ink applied by inkjet printing. (a) A micromechanical motor fabricated using silver nanoparticles for conductors and polyketone resin to insulate the conducting lines.[12] (b) A similar apparatus with improved ink control and post-deposition annealing showing 400-100 micron pitch lines.[33]

One of the advantages of ink transfer techniques is that they are generally insensitive to the composition or morphology of the nanoparticles. Far more critical to successful deposition is the viscosity of the ink and the surface energies between the ink solvent and the deposition surface. The precise viscosity required varies by technique. Sufficient viscosity is required to control of the deposition of the ink, but a high viscosity can cause printing errors and slow deposition rates. The ink viscosity must also be relatively independent of shear rate, because non-Newtonian fluid behavior can also cause printing errors and inconsistent results. Interaction of the surface energies creates a contact angle between the surface and the ink; the greater the contact angle, the greater the surface energy between the substrate and the ink. If the contact angle is too low,

the ink spreads over the substrate and pattern fidelity is lost. If the contact angle is too high, the ink remains in discrete drops and does not form continuous lines necessary for passive and active devices.[33]

A key advantage ink transfer processes is they drastically reduce the number of steps required to produce a patterned film. In traditional lithography, a patterned film requires at least nine steps: film deposition, photoresist application, pre-exposure bake, exposure, post-exposure bake, development, etch, and resist stripping. With additive ink processes, a patterned thin film can be obtained in one step, and the pattern can often be changed in real time with virtually no overhead. Additive processes also conserve material. In traditional deposition, the entire substrate is covered with the desired material and the material is selectively removed later. This leads to very low material utilization and efficiency, particularly for sparse arrays like displays. Conversely, additive process only deposit in the areas where the material is desired. Because these techniques are borrowed from the printing industry, there are virtually no theoretical limits to the width and length of the web that could be accommodated. However, engineering challenges to maintain uniformity across the web increase significantly as the web widens and, to a lesser extent, web handling becomes increasingly difficult as the web lengthens.

Specific ink transfer techniques, each with their advantages and challenges, are discussed in the following sections.

**Inkjet Printing**

Because of the relatively low cost of entry, straight forward programming, and reproducible results, significant research has gone into inkjet printing of nanoparticle inks. The basic process is identical to the process used in commercial inkjet paper printers. In fact, nanoparticle inkjet printing has been demonstrated on slightly modified commercial inkjet printers using standard print drivers, such as the designs shown in Figure 2.8. Inkjet printing (Figure 2.9) utilizes an ink reservoir with a pinhole orifice facing down and a piezoelectric actuator on top. The piezoelectric material strains according to the applied voltage waveform, forcing a small droplet of the ink out of the orifice. When the applied force is removed, surface tension holds the ink in the reservoir. Individual drops are built into the image by progressively scanning the print head over the substrate, scanning the substrate over the print head, or both (the print head has an axis of motion and the substrate has a perpendicular axis of motion).[12]

In order to achieve the highest resolution, pattern fidelity, and reproducibility, specialty printers for flexible electronics have also been created with 2 axes of travel, stabilized substrate support, surface proximity correction, and improved drop control, while still remaining relatively inexpensive. Just like inkjet paper printers, these systems are also scalable and very flexible. Various size webs can be accommodated on the same printer with few if any changes to the tooling. The pattern being printed can be changed in the middle of the web with little disruption to throughput. The disadvantages of inkjet printing are that features finer than 10-20 microns are difficult to achieve, and printing fine features reduces throughput as the individual drops must have a smaller

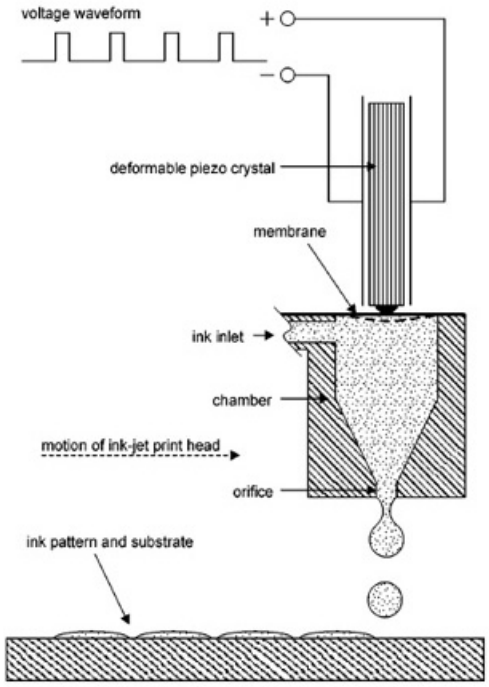


Figure 2.9: Schematic of an inkjet printing system showing ink being dispensed drop-wise in response to a voltage waveform.[12]

volume.[45] [33] Inkjet printers also require tight control of ink properties such that drops are uniform and the print heads do not become obstructed over time.

Despite the disadvantages, inkjet printing of nanoparticles offers a good balance of flexibility, scalability, throughput, and resolution for small to medium scale roll-to-roll processes.

**Gravure**

Gravure was developed for long runs and high throughput printing of periodicals. A schematic of the process is shown in Figure 2.10. A negative of the master pattern is etched into the gravure cylinder.[11] To begin the process, the gravure cylinder is inked from a reservoir. As the cylinder rotates, a doctor

blade removes excess ink from the surface, leaving ink only in the etched pattern. Finally, the ink is transferred to the web at the apex of the gravure roll. The gravure process has been demonstrated on several substrates with several different nanoparticle inks.[47] [57] Compared to inkjet, gravure has much higher throughput and is not as sensitive to variations in ink viscosity and surface tension. However, the patterns gravure can make generally have lower resolution and are limited in their geometries. While of less concern to high volume production, the gravure master is relatively difficult to fabricate. If the cylinder is damaged by the doctor blade or the web itself or layout needs to be altered, the master must be repaired or replaced at significant expense.

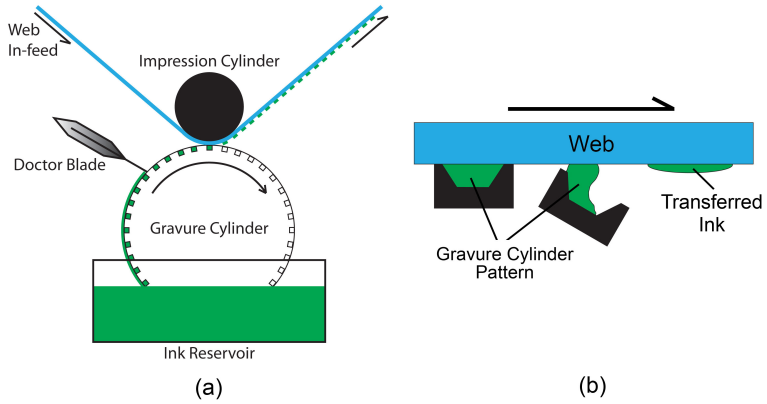


Figure 2.10: Schematic of a gravure printing system showing ink being dispensed onto an web via a rotating gravure cylinder. (a) Overview of the operation of a gravure cylinder. (b) A close up of the transfer process in sucessive grooves of the pattern.[57]

### Microcontact Printing

Microcontact printing, or pattern stamping, takes its inspiration from the oldest form of large-scale printing. It utilizes a positive stamp to transfer the de-

sired pattern to the substrate, identical to an ink stamp or printing press. Unlike gravure, the stamps that come in contact with the substrate are typically made of polydimethylsiloxane (PDMS) rather than metal. Figure 2.11(a) illustrates the microcontact printing process. The stamps can be easily fabricated from a rigid master mold by pouring the polymer mixed with a cross-linker and curing the polymer at 60 – 100°C for several hours. Once the PDMS stamp is released from the master, the nanoparticle ink is applied to the stamp surface. The excess ink is removed, and the stamp is applied to the permanent substrate, leaving a negative image of nanoparticle ink on the surface. The greatest advantage of microcontact printing over other inherently flexible pattern transfer techniques is the extremely high pattern resolution and fidelity. Lines with aspect ratios of 1:1 at less than 30 nm pitches can be fabricated.[51] Images of nanoscale features are shown in Figure 2.11 (b) and (c). Because only inexpensive PDMS copies of the master are used to physically transfer the ink, damage to the master is less of an issue than for gravure. Despite the technique's high resolution, it performs relatively poorly on layer-to-layer registration because of the dimensional instability of the stamp combined with the pre-existing instability of the flexible substrate.

## 2.3 Zinc Oxide Thin Films and Transistors

Despite the technical challenges to large scale production, research groups have been successfully fabricating n-channel ZnO field effect devices for decades. While early efforts were focused on single crystal substrates, improved substrates and deposition techniques, along with indium tin oxide (ITO) as a transparent conductor, led to a renewed interest in ZnO TFTs for possible trans-

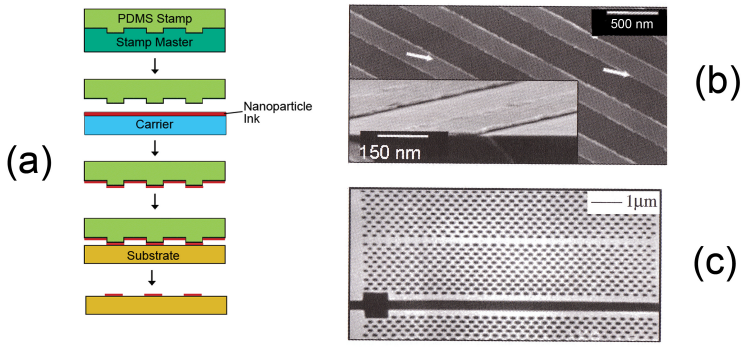


Figure 2.11: (a) Schematic of microcontact printing. Adapted from Santhanam and Andres. (b) Image of a microcontact deposited film showing 200 nm lines and spaces on a GaAs substrate. (c) Image of an array of 100 nm dots on GaAs substrate.[51]

parent electronics. Novel deposition methods, such as nanoparticle inks and solution crystal growth have also garnered some interest, but their performance has lagged significantly behind the devices fabricated using more conventional methods. The standardization of electrical testing of oxide transistors has been slow to develop. While key performance metrics like threshold voltage, mobility, and $I_{on}/I_{off}$ ratio are still cited, oxide transistors are prone to non-equilibrium charging defects and instabilities which can make absolute, repeatable measurements difficult if care is not exercised.

### 2.3.1 Transparent TFTs

One of the first transparent TFTs was demonstrated by Hoffman *et. al.*. They fabricated an enhancement mode ZnO TFT on a glass substrate with an ITO gate, source, and drain. The 220 nm gate dielectric was a sputtered alumina-titania multilayered structure. The 100 nm ZnO film was also RF magnetron sputtered at $10^{-4}$ torr in argon (80%) oxygen (20%) at room temperature.

Shadow masks were used to pattern the ZnO and the ITO layers; consequently, all of the devices are large (1.5 $mm^2$). The transfer curves for the device are shown in Figure 2.12. They reported a respectable mobility of 3 $cm^2$/V-s. Although the operating voltages were quite high, due to the thick gate dielectric, the transistor exhibited good saturation characteristics and an $I_{on}/I_{off}$ ratio of approximately $10^7$.[20]

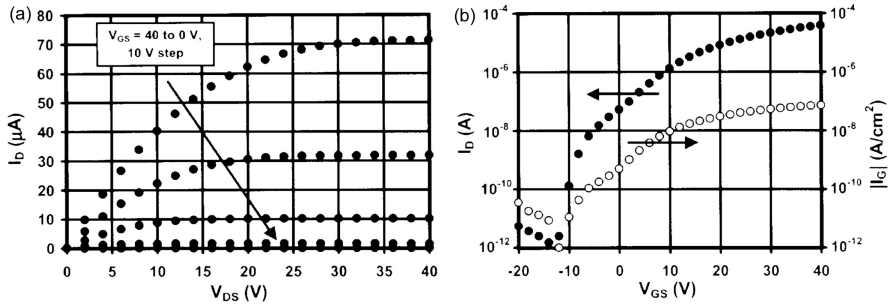


Figure 2.12: Transfer curves for a ZnO TFT fabricated on glass by Hoffman *et. al.* (a) $I_{ds}$ vs $V_{ds}$ for gate voltages of 0 to 40 V. (b) $I_{ds}$ vs $V_{gs}$ for $V_{ds}$ = 30 V.[20]

A year later, Nomura *et. al.* demonstrated an indium gallium zinc oxide (IGZO) TFT on 200 micron thick flexible PET. The amorphous oxide semiconductor, ITO conductors, and yttria gate dielectric were deposited at room temperature by PLD. The device characteristics were quite promising. Transfer curves are shown in Figure 2.13. The group reported mobilities up to 10 $cm^2$/V-s. Saturation and leakage characteristics were both good, but the $I_{on}/I_{off}$ ratio was only $10^3$, primarily because the on current was low. This might also be a result of the relatively thick gate dielectric.[42]

The final example that will be discussed here is work by Hsieh and Wua which showed a full lithographic and etch process by depositing the ZnO and

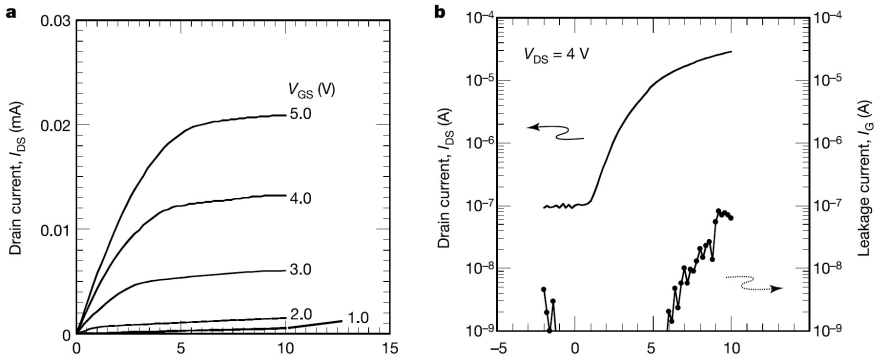


Figure 2.13: Transfer curves for an IGZO TFT fabricated on PET by Nomura *et. al.* (a) $I_{ds}$ vs $V_{ds}$ for gate voltages of 1 to 5 V. (b) $I_{ds}$ vs $V_{gs}$ for $V_{ds}$ = 4 V.[42]

then encapsulating it in silicon nitride. This encapsulation protected the ZnO from the strong bases used in photolithography and strong acids during etching. This increased processing flexibility permitted one of the few top gate ZnO TFTs reported in the literature (top gate and bottom gate structures are shown in Figure 2.14). Performance gains from this configuration are marked; the mobility was 25 $cm^2$/V-s and the extracted threshold voltage was 4.5 V. The $I_{on}/I_{off}$ ratio was excellent at approximately $10^7$.[21]

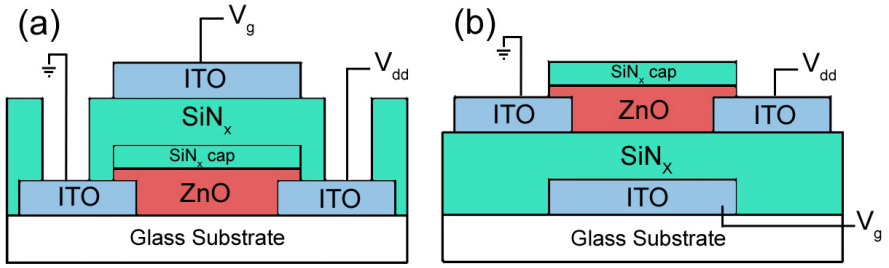


Figure 2.14: Two common geometries for thin film transistors, (a) top gate and (b) bottom gate. Bottom gate requires fewer mask levels and is more straight forward to fabricate, but top gate devices generally performed better because of a higher quality gate dielectric.[21]

### 2.3.2 Solution-processed ZnO TFTs

Several groups have explored unconventional means to fabricate ZnO TFTs, mostly via wet and non-vacuum processes that could be better suited for depositing on flexible substrates.

Perhaps most relevant to the work here, Lee *et. al.* fabricated ZnO TFTs from a ZnO nanoparticle ink precursor.[36] They fabricated nanoparticles by Poul *et. al.*[46] The particles were spun onto a heavily doped silicon wafer with 200 nm of thermal oxide. The nanoparticles were annealed at temperatures from 200 – 600 °C, and the SEMs of the films are shown in Figure 2.15. While they showed some particle sintering at the highest temperature, there was still significant porosity. Consequently, the percolation path could be quite long, increasing the series resistance of the completed devices. It is unclear why they did not anneal at higher temperatures. The devices they fabricated showed relatively

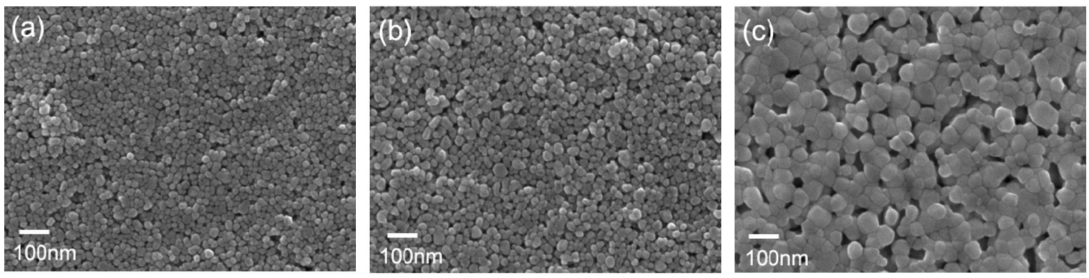


Figure 2.15: ZnO nanoparticle films furnace annealed at (a) 200°C (b) 400°C and (c) 600°C in oxygen[36]

poor performance, with mobilities ranging from $2\times10^{-5}$ to $3\times10^{-3}$ cm$^2$/V-s and $I_{on}/I_{off}$ ratios of 50 to $3\times10^3$ (See transfer curves in Figure 2.16) . The threshold voltages were measured around 30 V, though considering the thick dielectric and poor material quality, such high values are not unexpected. The paper did

not discuss the nature of the defects or why this processing method affected the device performance in any particular way.

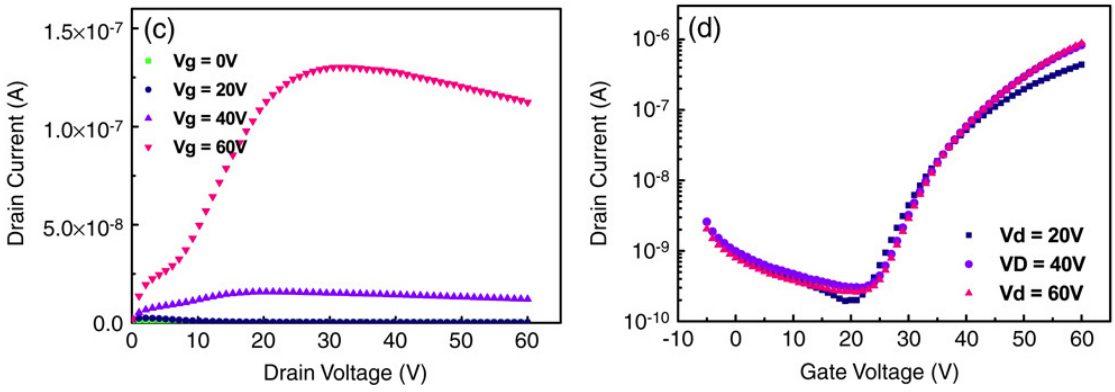


Figure 2.16: Transfer curves for ZnO nanoparticle TFTs annealed at 600°C in oxygen. Note the poor $I_{on}/I_{off}$ ratio and low transconductance.[36]

An alternative method is to synthesize a film directly from solution. One of the most straight forward methods was carried out by Wager's group at OSU. They titrated an aqueous solution of zinc chloride with $NH_4OH$ to form a ZnOH slurry which they deposited onto a substrate using inkjet printing. The films were annealed at 100 to 500°C on a hotplate to decompose the ZnOH into ZnO. They were relatively successful, in that the devices showed excellent $I_{on}/I_{off}$ ratios ($10^6$) and good saturated mobilities (up to 4 $cm^2$/V-s), although the device threshold voltages were still quite high (> 10 V). The transfer curves for a device annealed at 300°C are shown in Figure 2.17.[40]

Other methods include selective sol-gel deposition. Using a mixture of aqueous $Zn(NO_3)_2$, $NH_4OH$, and $H_2O_2$, Subramanian *et. al.* were able to deposit ZnO directly onto a substrate. The green films had poor electrical performance because of porosity and inclusions, but furnace annealing improved the per-

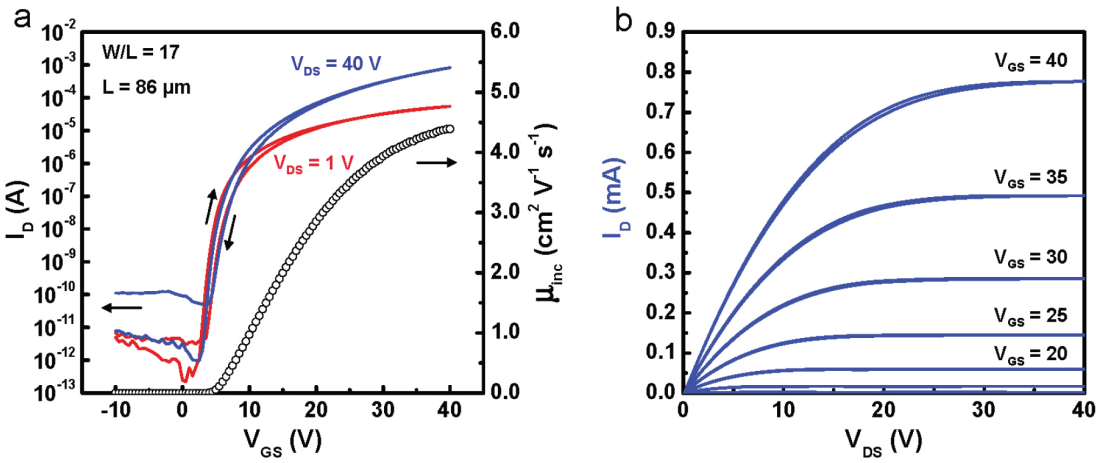


Figure 2.17: Transfer curves for ZnO TFTs fabricated by inkjet printing ZnOH slurries annealed at 300°C in air.[40]

formance to the point where they were able to achieve a saturated mobility of approximately 1 – 2 $cm^2$/V-s for films annealed at 350°C. The disadvantage to this method is that the sol-gel process is relatively slow, and it cannot be done ahead of time (as in nanoparticle deposition), so the throughput of this method is very low.[8] [56]

The final solution method found in the literature is spray pyrolysis. Aqueous solutions of $ZnCl_2$ can be sprayed onto substrates heated from 250°C to 450°C. Upon evaporation of the water, the zinc ions react with air to form ZnO. While their x-ray data proved that crystalline ZnO was formed on the surface, the measurements of the electrical resistivity of the films is unclear. The resistivity decreased by a factor of four as the deposition temperature was increased by 200°C, but this change could be from decreased porosity or increased electronic defects.[61]

CHAPTER 3

# ANNEALING NANOPARTICLE FILMS

## 3.1 Introduction

Large scale printing of inorganic nanoparticle solutions via gravure, microcontact, and inkjet printing is well-documented in literature and quite successfully demonstrated on modest production scales. However, a high temperature post-deposition anneal is required to removal residual solvents, decompose the stabilizing ligands, sinter the nanoparticles into a mechanically cohesive film, and improve electronic transport properties through grain growth. Sintering and grain growth typically require the highest temperature to achieve, which is a particular concern for heat-sensitive flexible substrates. In bulk materials, the temperature necessary for sintering and grain growth generally scales with the melting point of the material. In order to activate large-scale diffusion sufficient to cause sintering and grain growth, the temperature must be approximately 30-50% of the melting point for metals and 50-70% for covalently bonded materials.[49] Although this may seem prohibitively high, on the nanoscale surface effects cause a reduction in melting temperature that varies inversely as the radius.

First proposed in 1909 by Pawlow and based on Gibbs nucleation work, melting point supression was not directly observed until 1986 among low melting temperature metals (Figure 3.1). The authors put forward a theoretical upper and lower bound for the melting point depression based on known physical quantities.[2] The minimum melting temperature requirement assumes that the nucleation of the liquid layer is virtually instantaneous, such that the Gibbs free

energy of the solid and the liquid phase at the interface is equal:

$$\frac{T_m}{T_o} = 1 - \frac{3(\sigma_s/\rho_s - \sigma_l/\rho_l)}{\Delta H_f r} \tag{3.1}$$

where $T_m$ is the observed melting temperature, $T_o$ is the bulk melting temperature, $\sigma_s$ is the surface energy of the solid-gas interface, $\rho_s$ is the density of the solid, $\sigma_l$ is the surface energy of the liquid-gas interface, $\rho_l$ is the density of the liquid, $\Delta H_f$ is the latent enthalpy of fusion, and r is the radius of the particle. Conversely, the maximum temperature supposes melting does not occur until the solid-liquid interface becomes unstable:

$$\frac{T_m}{T_o} = 1 - \frac{\Delta\sigma_{ls}}{\Delta H_f r \rho_s} \tag{3.2}$$

where $\sigma_{sl}$ is the solid-liquid interfacial energy. In both extremes, the melting point depression varies inversely with the particle radius. Since the terms in Equations 3.1 and 3.2 are physically known quantities, the authors were able to show, despite significant uncertainity regarding interfacial energies and variable base pressures in the TEM, that the measured data fell between these extremes. This is consistent with their conclusion that a small driving force was required to melt the particles, but it was much less than would cause interface instability. Figure 3.1 summarizes their results, showing the raw data from bismuth (a) and the least-squares fit slopes for the four pure metals they tested (b).

Despite this helpful nanoscale surface effect that depresses the sintering temperature, refractory semiconductor materials still require optimal processing temperatures prohibitively high for use with most flexible substrates. Conventional furnace and rapid thermal annealing (RTA) processing cannot achieve high enough temperatures to calcine and sinter the semiconductor nanoparticles without damaging flexible substrates. Laser thermal processing can achieve

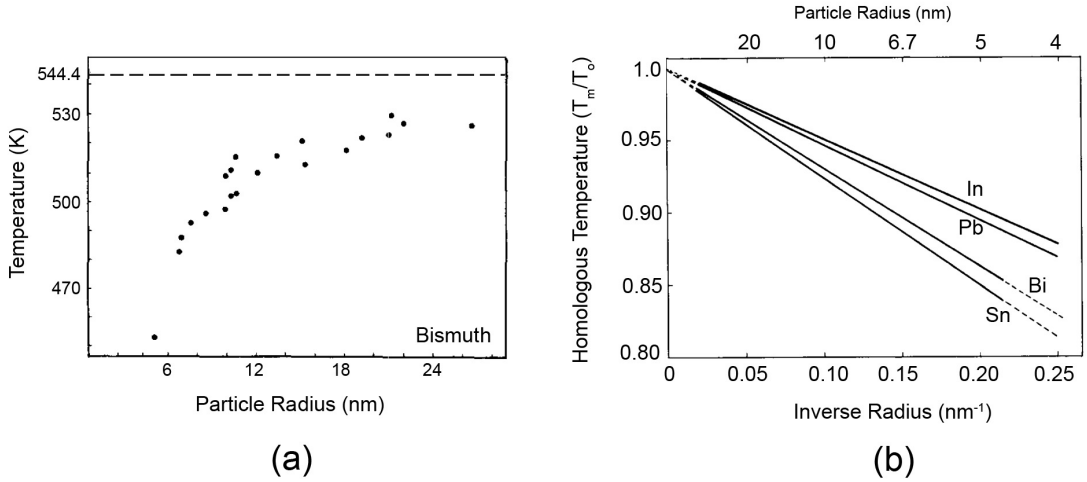


Figure 3.1: First direct observation of the melting of nanoscale metal particles, showing melting point depression. (a) Raw data for the melting temperature of bismuth vs. particle size. (b) Summary of the melting temperature for four types of metal nanoparticles, plotted versus inverse particle radius.[2]

transient elevated temperatures using temperature ramp rates from $10^5$ K/s to $10^{10}$ K/s, with corresponding time at temperature ranging from milliseconds to nanoseconds. The transient nature of the process limits thermal diffusion and enables heating the near surface to temperatures well above the maximum static use limit of the substrate.

## 3.2 Laser Melt Annealing

Laser melt annealing was first applied to crystalline silicon technology as a means to activate dopants above the solubility limit after ion implantation. The technique utilizes a high power, nanosecond laser pulse to induce surface melting of the amorphized silicon layer. The underlying crystalline silicon re-

mains solid and acts as both a seed for epitaxial growth and a thermal quenching medium. The ion-implant damaged area recrystallizes within 10 – 200 ns, incorporating the dopants uniformly onto electronically active lattice sites. While this can be done with various different types of lasers (ruby, Nd:YAG), excited-dimer (excimer) noble gas halide lasers are the most efficient and flexible. Excimer lasers create a population inversion in a high pressure gas chamber by initiating a high voltage discharge, promoting electrons into excited states, which allows the formation of a short lived compound between the noble gas and the halide. The dimer emits a photon at a discrete energy level as it decays back to its ground state, i.e. isolated atoms, and the energy of the photon is determined by the gas species in the chamber. The most common dimers all emit photons in the ultraviolet: ArF ($\lambda$ = 193 nm), KrF ($\lambda$ = 248 nm), XeCl ($\lambda$ = 308 nm), and XeF ($\lambda$ = 351 nm).[58]

Further work on silicon recrystallization by the Thompson group at Cornell University and others led to the development of low temperature polysilicon (LTPS) processing. Despite its superior transport properties compared to a-Si, poly-Si is usually deposited by LPCVD at 600 – 700°C, which prohibits use on temperature sensitive substrates such as polymers or borosilicate glasses. To form poly-Si at lower temperatures, they began by depositing a-Si via PECVD, which can be deposited at 100 – 200°C. Films were annealed with an excimer laser to induce crystallization. They were able to demonstrate full crystallization with localized surface temperatures in excess of silicon melt (1410°C) without the back surface exceeding 200°C for more than 10 $\mu$s, as shown in Figure 3.2. In this case, laser crystallized p-Si was fabricated on a PET substrate, which has a maximum static use temperature of 150°C, without damage.[5] [6]

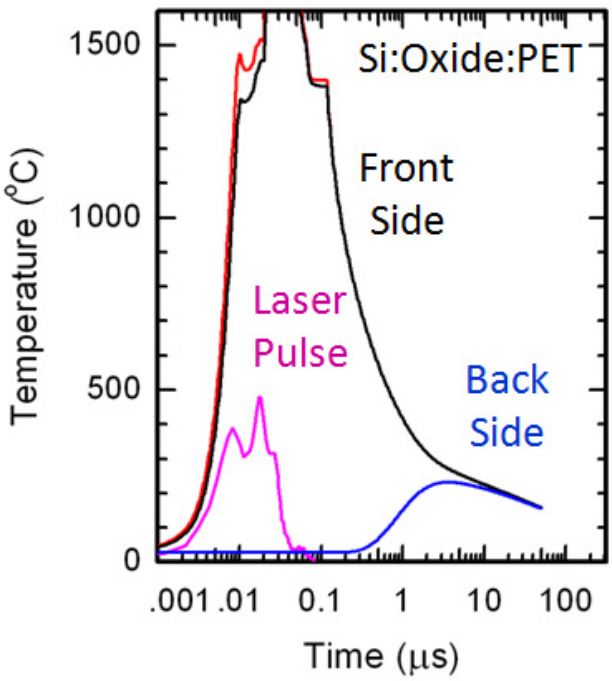


Figure 3.2: XeCl laser irradiation of silicon on PET with a silicon dioxide barrier layer. The temperature of the front side (silicon) and back side (PET) are shown as a function of time after the start of the 30 ns pulse. Note the 1400°C difference between the maximum front and back side temperature.[6]

A setup for the XeCl excimer annealing system is sketched in Figure 3.3. Because the emission wavelength is greater than 200 nm, absorption losses in air are minimal and annealing is performed at room temperature and pressure. Optics can be fabricated of quartz or UV grade fused silica. The lasing cavity emits a pulse at approximately 1 – 100 Hz, depending on the capabilities of the laser and the requirements of the application. Next, the beam is divided into the annealing beam and a timing signal, which is only a small fraction of the beam power (on the order of 0.01%). The energy delivered to the surface is modified by a two-plate attenuator. The first fused silica plate is coated such that the amount of attenuation is proportional to the angle of incidence. An angle perpendicular to the laser direction results in virtually 100% transmission; at the

other extreme, the plate at 45 degrees to the incident laser causes almost 100% reflection. The reflected power is absorbed by the walls of the attenuator. The transmitted power passes through an identical second plate which rectifies the beam to minimize beam shift. Next, the beam passes through a quartz collimator that homogenizes the beam and defines its shape on the sample. Finally, the beam is focused to the desired spot size using lenses. A diode laser beam (650 nm) is reflected off the surface of the sample to detect the melting of the surface. At 25°C, the reflectivity of solid silicon is approximately 35%, while liquid silicon reflects roughly 70%. Thus, it is straight forward to detect the onset of melt in silicon based on the reflected intensity. The sample is mounted vertically on an x- and z-axis motorized stage to minimize particle contamination and facilitate the use of programmed macro routines.

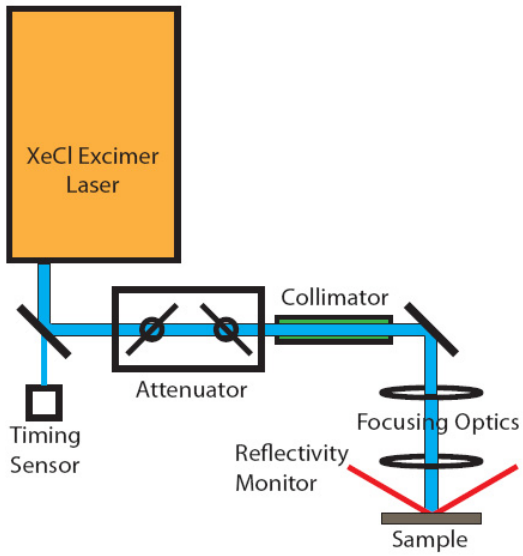


Figure 3.3: Schematic of the XeCl laser annealing system used in this work. The attenuator and homogenizer provide control of pulse power, with computer controlled motorized stage and reflectivity monitoring.

## 3.3 Laser Non-Melt Annealing

Non-melt annealing, as the name suggests, heats a sample with laser sources to temperatures below the melting point. It was developed as an alternative for dopant activation after ion implantation. Although it was developed for the same application as melt annealing, it takes a markedly different approach in the execution. Rather than using nanosecond pulses, non-melt annealing employs a high-power continuous wave laser for longer times, typically 100 $\mu$s to 10 ms. While many laser sources can be used for non-melt annealing, carbon dioxide ($CO_2$) gas lasers are commonly chosen because of their high efficiency and scalablility. The carbon dioxide laser is based on the allowed and disallowed vibrational modes of $CO_2$ to create the population inversion. The uniquely high efficiency, roughly 30%, is due to the addition of $N_2$ and helium to the $CO_2$. Diatomic nitrogen ( $N_2$) has a single bond stretch mode that is very close in energy to the excited state of $CO_2$, so there is an efficient coupling to the upper lasing mode, and the lifetime is on the order of $0.1 - 1$ ms. Carbon dioxide has two decay modes, symmetric and bending, which each emit at its corresponding wavelength, 10.6 $\mu$m and 9.6 $\mu$m, respectively.[52]

As stated earlier, non-melt annealing utilizes continuous rather than pulsed lasers. The transient aspect comes from relative motion between the substrate and the beam. The dwell time of the laser beam can be varied over orders of magnitude because it is determined by the full width half-maximum of the beam (in the direction of motion) divided by the relative velocity of the stage. Figure 3.4 is a simulation using the Cornell Laser Annealing Simulation Package (CLASP) of the beam temperature profile as a function of time (and distance) from the leading edge of the laser beam. In this particular sce-

nario, the nominal dwell is 500 $\mu$s and the laser power density is approximately $7 \times 10^4$ W/cm. Substrate doping is important because pure and lightly-doped silicon does not absorb the sub-bandgap 10.9 $\mu$m radiation. In degenerately doped silicon, free carriers are able to efficiently absorb the radiation. Within 100 $\mu$s, the temperature increases from room temperature to 1400°C, and falls below 200°C five milliseconds after the leading edge passes over a spot. This is where non-melt annealing derives its other name, laser spike annealing (LSA). The inset of Figure 3.4 shows the near-Gaussian shape of the temperature peak on an expanded time scale.[23]

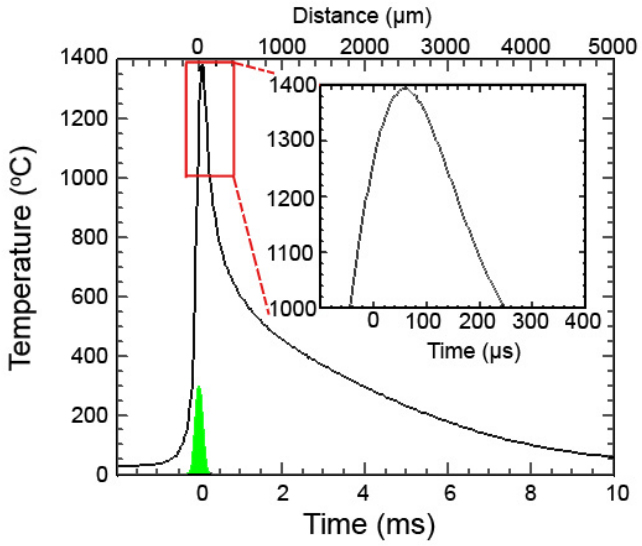


Figure 3.4: CLASP simulation of $CO_2$ laser anneal. The power density for the simulation is $7 \times 10^4$ W/cm and the dwell time is 500 $\mu$s.[24]

The small-scale system used in this study is diagrammed in Figure 3.5. The closed-tube $CO_2$ laser emits a beam at $\lambda = 10.6$ $\mu$m. As this is in the mid infrared, a HeNe (633 nm) targeting laser is mixed to be coincident with the $CO_2$ beam by a dichroic mirror. The targeting aid assists with beam and wafer alignment. Next, an attenuator modulates the beam based on the rotation of a

polarizer. It allows arbitrary power control between 1% and 80% of the full intensity of the beam. A process shutter allows the laser source to remain on and stable throughout the annealing process, but is only directed onto the sample when annealing. The focusing optics include a cylindrical lens which elongates one of the axes, forming an ellipsoid beam profile, which is subsequently focused down to a spot size of 90 $\mu$m (minor axis) x 750 $\mu$m (major axis). The minor axis is parallel to the scanning direction such that short dwell times can be achieved. The stage has three motion axes capable of covering an entire 300 mm silicon wafer, using a step and scan technique. The laser is scanned along one axis and the perpendicular axis steps the width of the beam to create a uniform time-at-temperature profile across the wafer.

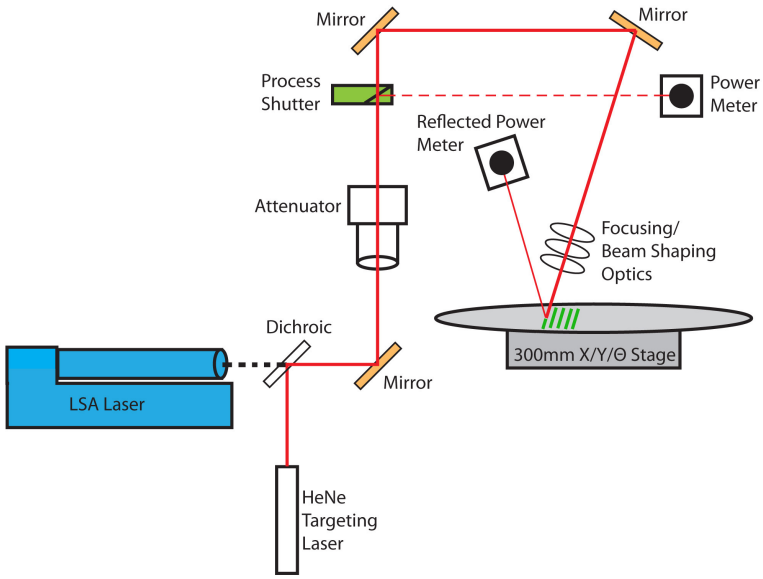


Figure 3.5: Schematic of a research scale $CO_2$ laser system. It is designed to anneal 300 mm silicon wafers with X, Y, and Θ position and laser power control.

### 3.3.1 Non-Melt Laser Annealing Temperature

As with all transient annealing techniques, the temperature profile is of critical importance to understanding the results. In practice, this profile is practically difficult to obtain because of the abbreviated time scale. For non-melt $CO_2$ laser annealing, a combination of continuum modeling confirmed by experimental techniques was used to predict not only maximum temperature, but also the temperature as a function of time and distance from leading edge of the beam. Because it is a scanning laser, time and distance are functionally equivalent. The simulations, developed as a part of CLASP, were designed to predict dopant activation and mechanical stress associated with laser spike annealing at multiple wavelengths based on the thermal, mechanical, and optical properties of the substrate. The theoretical results were verified experimentally using platinum thin film thermistors on heavily doped silicon substrates (Figure 3.6 (a)).[24]

The change in resistance of the 4-point resistors (to eliminate IR losses in the contacts) as a function of temperature is linear, so it can be scaled to measured melting points (in this case silicon and gold) to obtain a high sampling rate, low thermal mass temperature measurement. The result (Figure 3.6 (b)) confirmed that the thermistors easily resolved sub-millisecond changes in temperature and revealed an asymmetric temperature profile, as predicted by simulation, due to the thermal conductivity of the substrate. The theoretical and experimental results match well and allow similar curves to be extrapolated for arbitrary power densities and dwells. Temperature measurements made via this method are utilized extensively in this work to characterize film annealing.

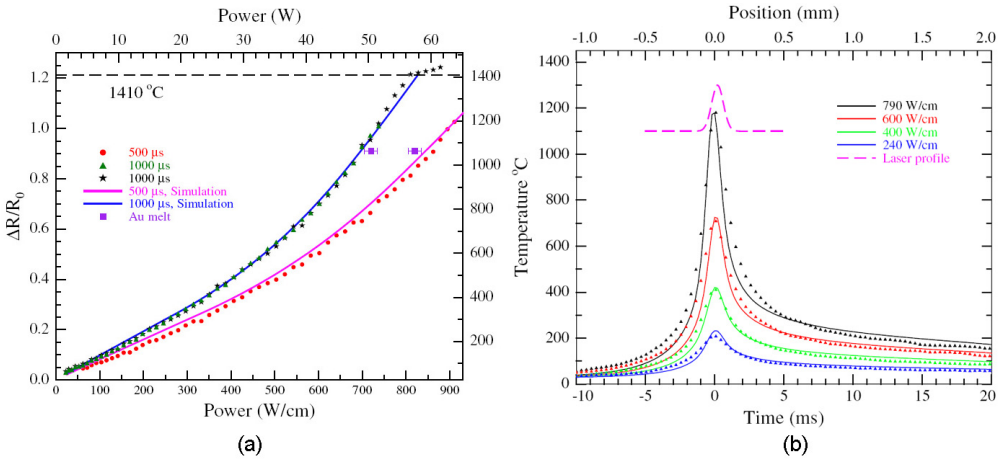


Figure 3.6: (a)Temperature vs. linear power density calibration for $CO_2$ laser annealing. Calibrations are for dwell times of 500 $\mu$s and 1 ms on heavily doped silicon substrates. (b) Time-resolved temperature measurement extracted from the platinum thin film thermistors for several power densities and the Gaussian laser profile (hashed line).[24]

CHAPTER 4

# ZINC OXIDE NANOPARTICLE SYNTHESIS

## 4.1 Requirements

Nanoparticle inks are a potential source material for an inherently flexible, high throughput deposition system. The first challenge was to fabricate or obtain nanoparticles. Due to the demands set by the application, this proved more challenging than initially realized. First, the nanoparticles had to be high purity, with low concentrations of elements that could diffuse rapidly or cause charged defects. Second, the particles had to be of relatively uniform size and be relatively equiaxed, although not strictly spherical. Equiaxial particles tend to pack better in random arrangements with fewer large pores and voids. Furthermore, the exact size was not as critical as the repeatability of the size from one synthesis run to the next. Vastly different sized particles could cause differences in perceived bulk diffusion or melting points due to surface energy. Lastly, the particles had to be available in quantity. Quantities sufficient to fill a TEM field or disperse in solution to make a spectrometer sample are miniscule compared to the gram quantities necessary to coat wafers and other large substrates. To this end, the reaction had to be relatively straight forward, involve air stable reactants, and have reasonable yields. Zinc oxide was a logical nanomaterial choice because of its prominence as a wide bandgap semiconductor, its stability, and numerous chemical routes to synthesis. A literature review of ZnO particle synthesis found numerous articles describing numerous potential synthesis routes, which will be summarized briefly below.

The fundamental concept for virtually all monodispersed nanoparticle

synthesis was pioneered by Murray and Bwendi in the early 1990s with their work on organometallics and chalcogenides.[41] The conceptual process illustrated in Figure 4.1 can be extended to create a wide variety of nanoparticle compositions, sizes, and shapes. In the synthesis, one reactant is dissolved in a solvent with a small quantity of stabilizing ligand. The reaction vessel is sealed to prevent any oxygen or water vapor from entering. Once the reaction temperature is reached, the second reactant is injected into the reaction vessel. This supersaturates the solution and causes a slight drop in the temperature. Nuclei, also called nanoclusters, form rapidly, and they consume enough of the precursors during nucleation that the solution is no longer supersaturated and no new clusters can form. The nuclei grow by incorporating the remaining precursors in solution. The stabilizing ligands are present in the solution to prevent the nuclei from interacting and fusing with each other. Through careful control of reactants, ligands, concentration, time, and temperature, this template has virtually unlimited permutations to fabricate nanoparticles.

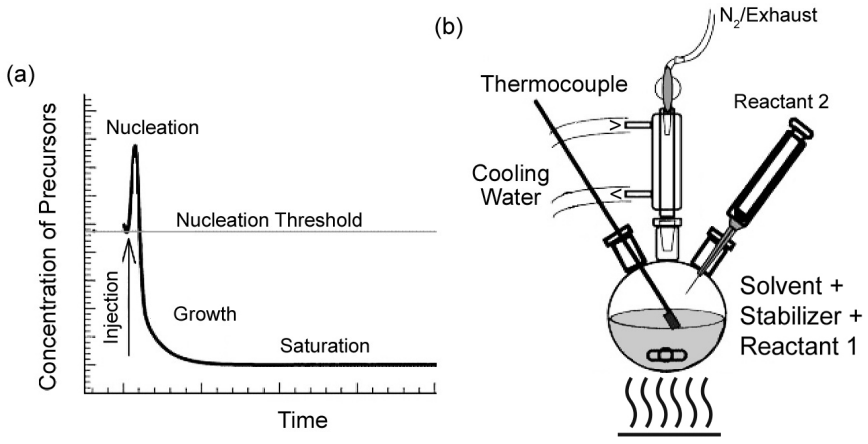


Figure 4.1: Conceptual diagram for the general reaction to create monodispersed nanoparticles.(a) Graph showing the precursor concentration with time. (b) Schematic of the reaction vessel.Adapted from Murray *et. al.*[41]

In the specific case of ZnO, the preferred precursors are hydrated zinc salts, typically zinc acetate[46] and zinc chloride[3]. Oleate, citrate, nitrate, and sulfate salts have also been used. This is primarily due to lower cost and convenience; when dissolved, zinc is already ionized and will bond readily. Because the reaction does not have to break the ether bond of an organometallic precursor, it can be performed at a lower temperature. Virtually all of the routes are two step reactions, the first being hydrolysis and the second being condensation. In ZnO synthesis, hydrolysis shows the widest variety of routes, but ZnOH is the typical product. The hydrolyzer is generally a strong base, LiOH, NaOH, KOH, and $NH_4OH$ are common. Other routes employ coordinated solvents such as polyols. Zinc hydroxide then enters into a common condensation reaction which forms the zinc-oxygen-zinc 3D networks necessary to form nanoparticles. The relative rates of these two reactions determine the morphology of the final particles, as shown in Figure 4.2.[49] Faster hydrolysis will yield more equiaxed particles, while slower hydrolysis tends to grow into more extended structures. Faceting usually indicates that the particular stabilizing ligands have strong binding to a particular crystallographic plane of the particle.

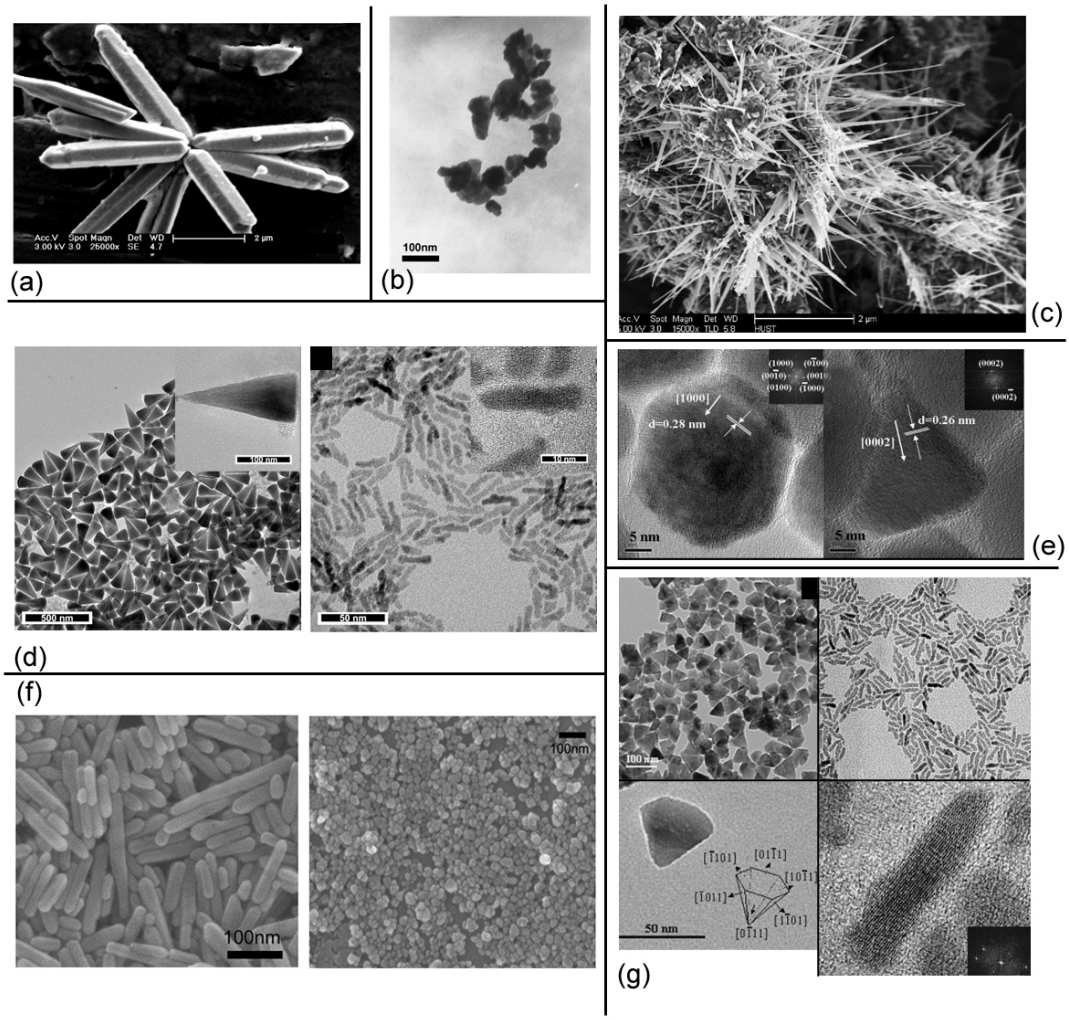


Figure 4.2: Examples of various ZnO nanoparticle morphologies and synthesis methods by SEM and TEM: (a) Star clusters, synthesized hydrothermally[3], (b) Spheroid, hydrothermally grown from zinc nitrate and ammonium hydroxide[7], (c) Needles, fabricated from fine ground zinc power mixed with hydrogen peroxide,[15] (d) cones and rods, formed using a coordinating solvent dodecanediol to hydrolyze zinc acetate,[27] (e) hexagonal particles formed using a zinc chloride and sodium oleate complex[10], (f) rods and spheroids from the same reactants, just changing when the reactants are added,[36] (g) hexagonal cones and rods from the same reactants, only changing the coordinating solvent and stabilizer.[31]

## 4.2 ZnO Synthesis by the Polyol Method

The polyol method was discussed briefly in the previous section as a possible source for high quality crystalline ZnO nanoparticles with diameters in the 20-40 nm range. As such, it is worth discussing in greater detail. Unlike most other synthesis methods that use a strong polar solvent such as water or methanol, the polyol method, as its name suggests, uses a coordinating organic solvent with multiple alcohol groups. These alcohol functional groups act as nucleophiles to hydrolyze the zinc salt (see Figure 4.3).

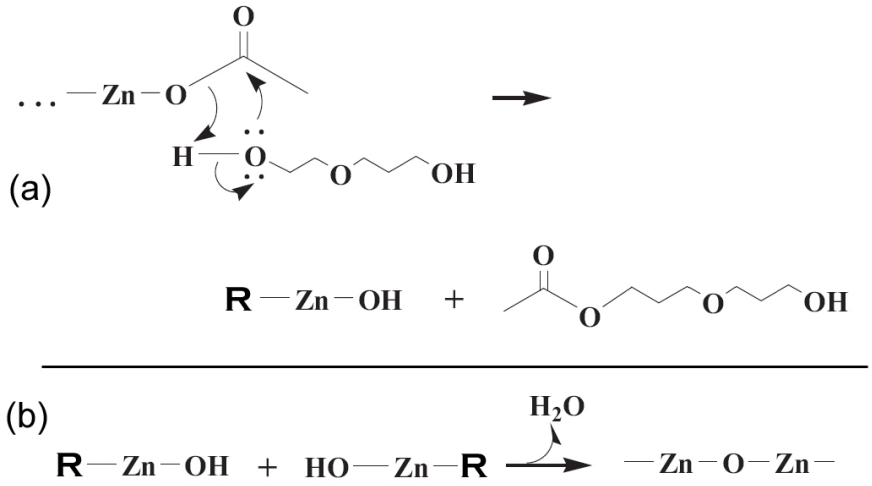


Figure 4.3: Reaction mechanism for hydrolysis and condensation of the polyol synthesis method. (a) Illustration of diethylene glycol acting as a nucleophile to hydrolyze zinc acetate. (b) Subsiquent condensation reaction to form ZnO.

The primary advantage of the polyol synthesis is that the coordinating solvent (diethylene glycol, in this case) has a much higher boiling point, allowing the reaction to be performed at elevated temperatures (180°C). Not only can the reaction proceed faster than most other synthesis methods, it uses water to ini-

tiate the condensation reaction rather than a strong base. This eliminates the hydroxide counter ion in solution (usually sodium or potassium) that can be a possible source of contamination and charged defects in the completed device.

### 4.2.1 Procedure

The polyol synthesis for nanonparticles is as follows.[46] Six grams of poly(vinylpyrrolidone) (PVP) (Aldrich #PVP10) with a molecular weight of 10,000 g/mol was added to 250 mL of diethylene glycol (Aldrich #32160) in a 3-arm flask with a recondensing column. The flask was heated to 70°C under nitrogen while stirring. After all of the PVP dissolved, 3.29 g of zinc acetate (Aldrich #379786) was added to the flask, and the temperature was ramped up to 180°C. Once the reaction temperature was reached, 1.08 g of DI water was injected into the flask to initiate the hydrolysis step. The particles were allowed to grow for 30 minutes, and then were plunged into an ice bath to terminate the reaction. Once at room temperature, the particles were precipitated by adding 40-60 mL of ethanol. The suspension was centrifuged at 10,000 rpm to isolate the particles. The supernatant was poured off and the particles were redispersed in ethanol and centrifuged three times to clean any remaining solvent and reactant byproducts from the solution. The particles were then dried overnight in a vacuum oven at 50°C. The process resulted in approximately 0.8 g of ZnO nanoparticles, approximately 50% of theoretical yield.

## 4.3 ZnO Synthesis via Sol-gel Method

Sol-gel synthesis is another synthetic route to ZnO nanoparticles. Rather than reacting with a coordinating solvent, the reaction is performed in an inert solvent, such as methanol. The temperature is also lower, only 60°C, because the boiling point of methanol is 65°C. The reaction takes longer, but literature suggests that the resulting particles will be smaller and easier to disperse in simple solvents. The hydrolysis and condensation reactions are illustrated in Figure 4.4. The primary difference between this and the preceding route is that the hydrolysis step uses a strong base rather than a coordinating diol. Additionally, the zinc counter ion acetate acts as both a stabilizer during growth and as a surface ligand in suspension.[4] [9]

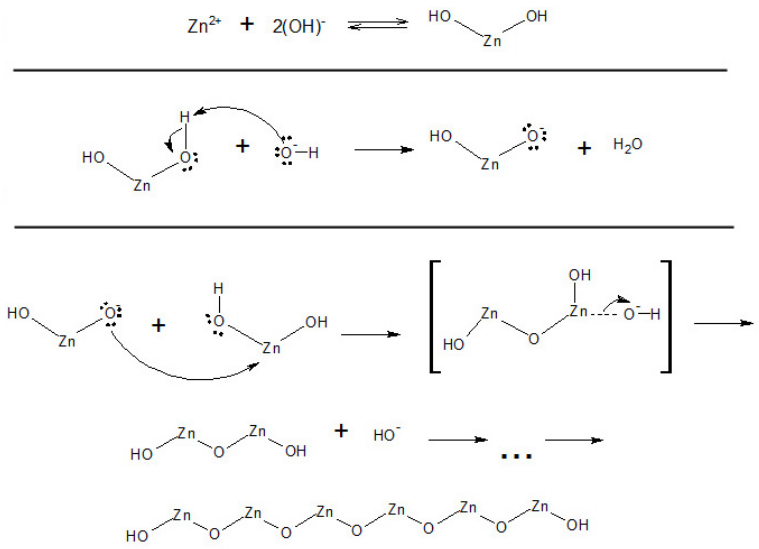

Figure 4.4: ZnO sol-gel hydrolysis and condensation

All glassware was rinsed with spectroscopic grade methanol (OmniSolv #MX0488-6) and blown dry with nitrogen. This reaction is performed in air, so

a simple volumetric flask was substituted for a 3-neck flask. Next, 4.26 g of zinc acetate dihydrate (Aldrich #379786) was combined with 190 mL of spectroscopy grade methanol and put on the hotplate at 60°C. While heating, 2.18 g of potassium hydroxide (Aldrich #306568) was mixed with 97 mL spectroscopy grade methanol, using sonication to fully dissolve the KOH pellets. At the reaction temperature of 60 °C, the KOH solution was poured into the zinc acetate solution. After 2.5 to 3.5 hours, the solution becomes turbid, indicating the particles have nucleated. Fifteen minutes after the solution turns turbid, the solution was removed from the heat and the reaction was quenched with an ice bath. The particles were centrifuged at 9000 rpm for seven minutes, and the supernatant was poured off. The nanoparticles were redispersed with anhydrous methanol (Aldrich #322415) and centrifuged again. The last step was performed at least 3 times to clean the particles of any residual reactants. In order to prevent agglomeration, the nanoparticles were not dried in a vacuum oven; they were immediately dispersed in 10 g of chloroform ($CHCl_3$).

Since the dry mass of the product could not be determined for each synthesis, the amount of product was estimated based on a standard run and then approximated at 5-10 wt% for all subsequent runs.

## 4.4 Nanoparticle Characterization

Particles produced via both synthesis routes were evaluated by dynamic light scattering (DLS), electron microscopy, and thermo-gravometric analysis (TGA) to assess the results of the synthesis and the respective suitability for laser sintering. Additional analysis was performed on the sol-gel synthesized

particles, including x-ray diffraction and UV-visible absorbtion analysis.

### 4.4.1 Dynamic Light Scattering (DLS)

Dynamic light scattering (DLS) was performed with a Malvern Zetasizer Nano-ZS. The principle behind DLS, Brownian motion of small particles in a fluid, is inversely related to its size according to the Einstein-Stokes equation:

$$r(H) = \frac{k_B T}{3\pi\eta D} \tag{4.1}$$

where $r(H)$ is the hydrodynamic radius of the particle, $k_B$ is Boltzmann's constant, $T$ is temperature, $\eta$ is the fluid viscosity, and $D$ is the diffusivity. The diffusivity is determined by comparative measurement of the Rayleigh scattering of coherent light. When particles are significantly smaller than the wavelength of the light, the intensity of the scattered light is given by:

$$I = I_o \left( \frac{1 + \cos^2 \theta}{2R^2} \right) \left( \frac{2\pi}{\lambda} \right)^2 \left( \frac{n^2 - 1}{n^2 + 2} \right)^4 r^6 \tag{4.2}$$

where $R$ is the distance to the particle from the source, $\theta$ is the scattering angle, $\lambda$ is the wavelength of the light, $n$ is the index of refraction of the particles, and $r$ is the radius of the particles. DLS make use of the fact that the intensity varies to the sixth power with particle radius. Measurements over time can distinguish intensity shifts when particles drift in and out of the illuminated volume. Based on these measurements, an aggregate diffusivity is found and the particle size distribution is calculated.[50]

Standard indices of refraction of the suspension medium and ZnO were used, along with standard viscosity of the suspension medium. The suspensions for DLS were dilute; therefore, the solids loading was unlikely to appre-

ciably affect the flow characteristics of the suspending medium. The Zetasizer system was calibrated to a 100 nm polystyrene bead standard.

### Polyol Particles

In the case of the polyol particles, the vacuum dried particles were dispersed at 0.1 wt % in tetrahydrofuran (THF). The suspension was sonicated for 5 minutes, filtered with a 5 micron filter (to remove any dust or debris), and dispensed into a standard quartz cuvette for the Zetasizer. The particle size was sequentially measured eleven times to rule out any aggregation or dissolution of the particles over time. The results are averaged and presented in Figure 4.5. The data is bimodal, with a sharp peak between 100 and 200 nm and a broad peak from approximately 300 nm to 1000 nm. The larger aggregates (> 300 nm) were likely due to the vacuum drying process, and the aggregates were only loosely bound by van der Waals forces. These clusters could be dispersed through the proper dispersion medium and ultrasonication.

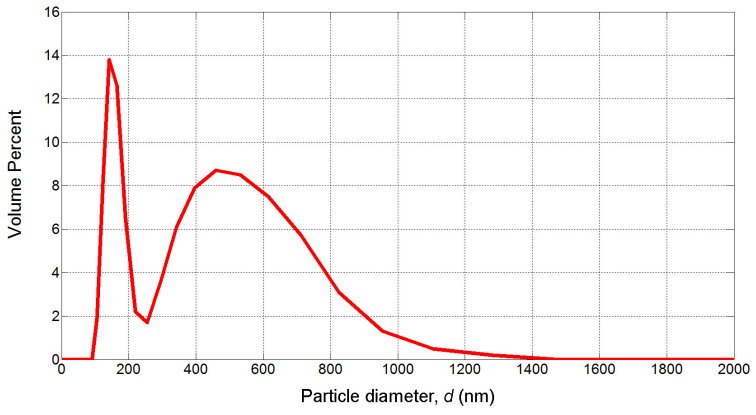


Figure 4.5: DLS particle size by volume for particle synthesized via polyol route. Bimodal distribution of the data indicated the particles were 100 – 200 nm with larger aggregates consisting of several particles.

**Sol-gel Particles**

The sol-gel synthesized particles were dispersed in chloroform ($CHCl_3$) at approximately 0.1wt%. Like the polyol particles, the suspension was sonicated for 5 minutes, filtered with a 5 micron filter (to remove any dust or debris) and dispensed into a standard quartz cuvette for the Zetasizer. The particle size was sequentially measured eleven times, and the average of the measurements is presented in Figure 4.6. The sol-gel nanoparticles were significantly smaller, with the number average reported at 5.9 ± 0.87 nm and the volume average was 7.6 ± 1.5 nm. The close agreement between the number average and volume average indicated a narrow size distribution.

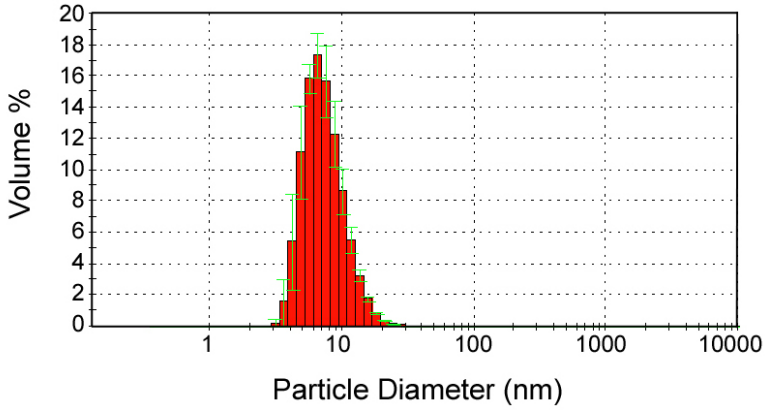


Figure 4.6: DLS particle size by volume for nanoparticles synthesized via sol-gel route. The particles were monodispersed with a volume average diameter of 7.6 ± 1.5 nm

### 4.4.2 Electron Microscopy

#### Polyol Particles

Scanning electron microscopy (SEM) images, as shown in Figure 4.7, were of significant aid in explaining the reason for the varying particle size. All SEM images were taken with a LEO 1550 FESEM at an accelerating voltage of 5 – 8 keV. The particles, as measured by DLS, were actually agglomerations of particles. Furthermore, the individual particles in the agglomerations were approximately 20 – 30 nm, which is consistent with the sizes reported for this synthesis in literature. Because of the roughly spherical shape and uniform size, the aggregation must have occurred in solution, not during drying.

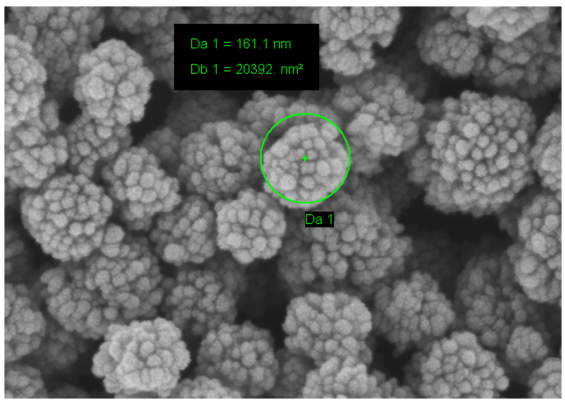


Figure 4.7: SEM of ZnO nanoparticles formed by a polyol synthesis, displaying aggregation of 30 nm particles into larger structures 100 – 200 nm.

To stop the larger structures from forming, additional PVP surfactant was added to the initial reaction and/or the concentration of reactants was lowered. However, in those cases, no product formed. Another possible source for additional ZnO aggregation was condensation (water) dripping down from the column or temperature variation over the course of the run. Runs were attempted

without the condensation column (the arm usually attached to the column was stoppered). The protocol was also altered so that the 3-arm flask was immersed in a silicone oil bath to minimize any temperature variation over the course of the synthesis. Neither of these changes altered the particle size or morphology. Efforts to break up these particles into the 20 – 30 nm constituents by chemical or mechanical means were also unsuccessful.

**Sol-gel Particles**

Scanning and transmission electron microscopy confirmed the approximate size and morphology of the particles. The TEM image in Figure 4.8 (a) was prepared by dropping a dilute solution of nanoparticles onto a carbon covered TEM grid and allowing the solvent to evaporate for 1 hr. The instrument was a FEI T12 at 100 keV. The approximate particle size was measured in-situ using software tools, with an average diameter of three particles being 4.8 nm. This is significantly smaller than the values reported by DLS. This result is not surprising, as TEM only shows $Z$ contrast, hence the ligands (which scatter light in DLS) are not apparent against the background carbon coating. Also, oxygen in the ZnO will not show up well in TEM either. Therefore, the DLS, x-ray, and TEM measurements are all consistent with one another and confirm the approximate size of the particles.The SEM image Figure 4.8 (b) was prepared by dropping a concentrated solution onto the surface of a heavily doped silicon wafer, providing a film composed of many monolayers. The image is undifferentiated because the particle size is near the resolving power at the 5 keV accelerating voltage.

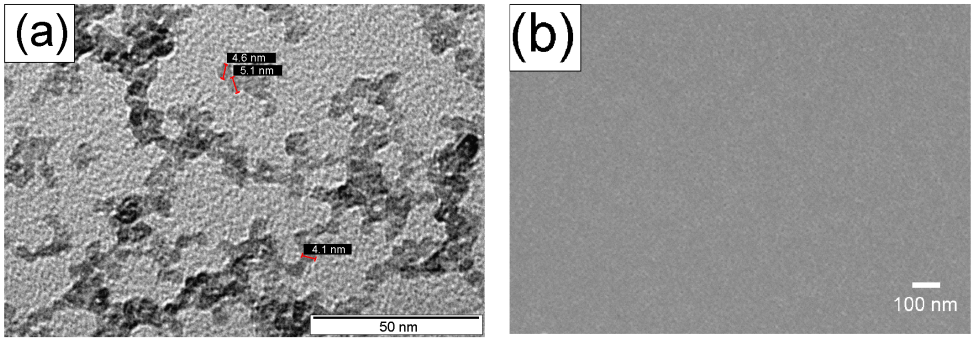


Figure 4.8: Electron microscope images of sol-gel synthesized nanoparticles. (a) TEM, three measurements in the field indicate the average particle size to be 4.6 nm (b) SEM, multiple monolayers appear flat without distinguishing agglomerations or voids.

### 4.4.3 Thermo-gravimetric Analysis (TGA)

Thermogravometric analysis (TGA) measures the loss of volitile components as the sample is heated. In addition to quantifying the total mass lost, the temperature at which the mass changes can give indication of the species being evaporated or decomposed. The TGA swept temperature from room temperature to 550°C or 600°C at 10°C/min. The microbalance sampled the mass at 2 Hz and the results were recorded as total mass and mass fraction remaining.

**Polyol Particles**

Results for polyol synthesized particles are shown in Figure 4.9. There is relatively little mass loss over the temperature range (4%), indicating low organic content. This makes the film more stable under excimer illumination. Roughly 0.5-1.0% of mass loss is due to adsorbed water (ZnO is hydrophilic). The large 3% drop from 275 – 375°C is likely from residual DEG or the reaction product diethylene glycol monoacetate (also called 2-[2-(acetyloxy)ethoxy]

ethanol). The final reaction component, poly (vinylpyrrolidone) decomposes at 470-500°C, but no mass loss was observed in this region. As the particles were washed in ethanol several times and PVP is soluble in ethanol, PVP in the dried particles was not expected.

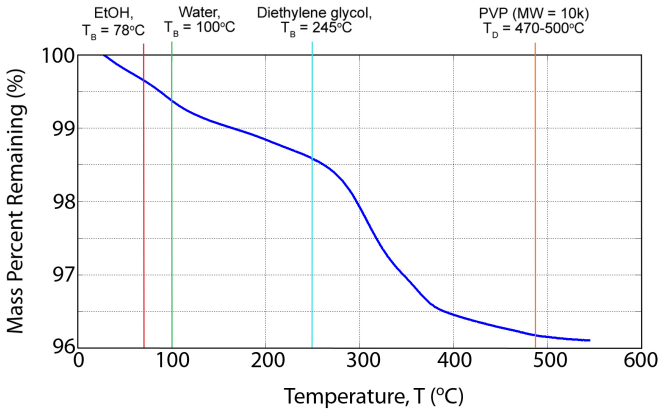


Figure 4.9: TGA analysis of ZnO particles up to 550°C.The bulk boiling points of ethanol, water, and diethylene glycol are indicated, along with the decomposition temperature range of poly(vinylpyrrolidone).

Overall, this shows the particles have a very low percentage of residual organics, approximately 3%, which is adventageous for annealing because there is relatively little out gassing or volume loss during annealing. However, the lack of any surface ligand chemistry makes the particles hard to disperse, unstable in solution, and limited to low solids loading.

**Sol-gel Particles**

The TGA for the sol-gel synthesized particles was consistent with prior literature.[4] The mass fraction lost as a function of temperature is shown in Figure 4.10. Like the polyol synthesized particles, the sol-gel synthesized particles

had adsorbed water on the surface. A higher percentage (2-3%) was observed in the sol-gel case because the particles were smaller, so they had a greater surface area per mass. The literature indicated that the acetate ions would covalently bind to the nanoparticles and act as stabilizing ligands. The TGA corroborates this because there is an approximately 9% mass loss in the temperature range where acetate is expected to break down. In contrast to the polyol particles, the

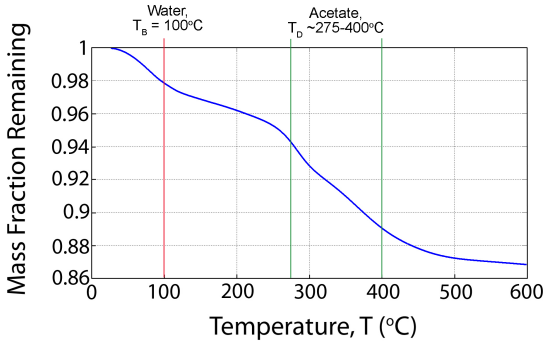


Figure 4.10: Thermo-gravimetric analysis (TGA) of sol-gel synthesized ZnO nanoparticles. The 10% mass lost from 275 to 400°Cis most likely the decomposition of the acetate ligands bonded to the surface of the nanoparticles.

organic content in the sol-gel synthesized particles was much higher. The sample lost a total of 13% of its mass by 600°C. As subsequent excimer annealing will heat the ZnO films to temperatures in excess of 1000°C in less than 10 ns, it was necessary to remove the organic material by some other means before excimer annealing. With this large organic loading, film damage is very likely during laser annealing.

### 4.4.4 X-ray Diffraction (XRD) of Sol-gel Particles

X-ray diffraction measurements were made as offset $2\theta$ scans from 25-45 degrees on a Rigaku Smartlab x-ray diffractometer. An offset $2\theta$ scan had the x-ray source offset by two degrees from the typical $2\theta$ scan to eliminate the single crystal silicon substrate peaks, which would normally overwhelm the ZnO peaks by several orders of magnitude. The detector still picks up the polycrystalline peaks, albeit at the offset angle, but the substrate peaks are completely eliminated. As shown in Figure 4.11, peaks identified were consistent with the 2 strongest peaks of the wurtzite ZnO structure. The peaks are broad because the small size of the polycrystals. The Debye-Scherrer integrated area method estimated the crystallite size at 6.0 nm, consistent with size inferred by other methods.

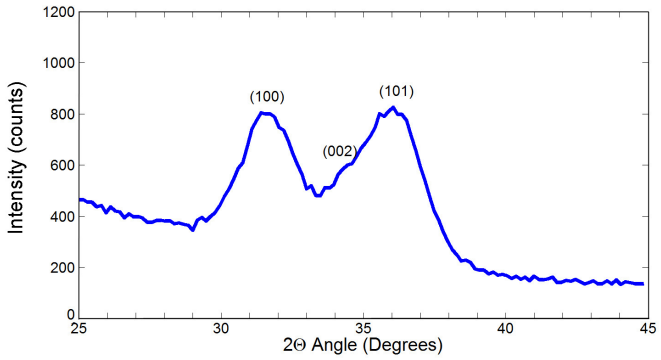


Figure 4.11: Offset $2\theta$ scan of sol-gel synthesized nanoparticles showing characteristic peaks of wurtzite ZnO along with peak broading consistent with the known particle size.

### 4.4.5 UV-Visible Absorption of Sol-gel Particles

Ultraviolet-visible absorption was done on the CCMR Shimadzu UV-Vis-NIR Spectrometer, sweeping from 800 nm to 200 nm wavelength. Sol-gel ZnO nanoparticles were spun onto a clean fused silica substrate with no additional processing or annealing. The spectrometer was configured in the transmission mode to eliminate constructive and destructive interference caused by interfaces. In Figure 4.12, the band edge of ZnO was clearly visible at a wavelength of approximately 360 nm. This corresponds to a bandgap of 3.4 eV, which is slightly higher than the accepted literature value for ZnO (3.1 – 3.3 eV). The

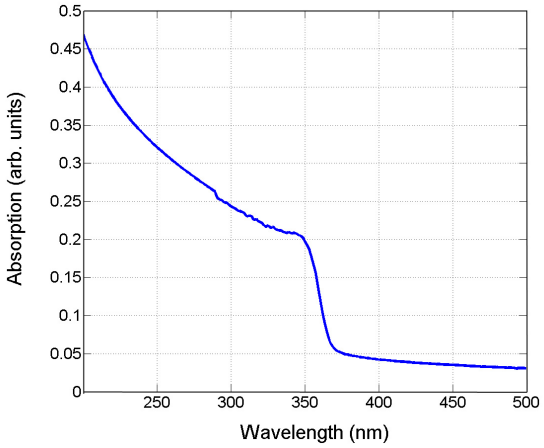


Figure 4.12: UV-vis absorption spectrum for as-spun sol-gel particles on a fused silica substrate, showing a conduction band absorption edge at 3.4 eV.

increased bandgap is likely due to quantum confinement effects. The particles were less than 10 nm in diameter, so one would expect the bandgap of the particles to increase slightly, according to the Kayanuma approximation:[60]

$$\Delta E_{dot} = \left(\frac{\pi a_B}{a}\right)^2 R_y - 1.79\frac{a_B}{a}R_y \tag{4.3}$$

where $a_B$ is the Bohr radius of the semiconductor, $a$ is the radius of the particle, and $R_y$ is the Rydberg energy of the exciton. For ZnO, the accepted literature

values for the Bohr radius and exciton energy are 2.34 nm and 59 meV, respectively. Therefore, one would anticipate the $\Delta E$ for the synthesized particles to be approximately 0.17 eV. This is further corroboration that the nanoparticles are ZnO wurzite with a low concentration of defects or trap states. Additionally, the nanoparticles can be approximated as isolated 0-D quantum wells with an extent of roughly 8 nm.

## 4.5 Nanoparticle Dispersal

Once the particles were synthesized and cleaned, it was necessary to stabilize them to remain in suspension. As discussed previously, ligands introduced onto the surface of the particles create an ionic and/or steric barrier between the particles. Without stabilizing ligands or surfactants, the particles would quickly aggregate and precipitate out of suspension. Nanoparticle ink depositions would be non-uniform and could potentially damage equipment (i.e. inkjet print heads or PDMS stamps).

### 4.5.1 Ligand and Surface Chemistry

Because there was no reliable method until recently to view ligand-surface interactions directly, ligand and surfactant chemistry is as much art as science. Empirical data gathered over many iterations of trial and error led to formulas that worked for one class of surfaces, but not for another. Little formalism exists beyond "rules of thumb". By applying density functional theory (DFT) calculations, Choi *et. al.*[9] were able to begin to understand why nanoparti-

cles and ligands interact as they do and constructed nanoparticle superlattices with ligand scaffolds to direct placement. In a recent paper, they modeled surface densities and bonding energies for different crystal surfaces of cubic PbS nanoparticles and acetate ligands. These conclusions are extensible to the ZnO system to first order because the zincblende {111} facets have the same atomic density and configuration at the wurtzite {0001} basal planes. There are also similiarities between the {1120} prism faces of wurtzite and the {100} facets of the zincblende structure of PbS in that they are both low index, low atomic density surfaces. Figure 4.13 shows how acetate binds to the low index surfaces of the low index surfaces of PbS. The first conclusion from their work is that the surface energy is lowest when the both surfaces are cation terminated, but the {100} surfaces actually have only half of the cations of a full populated {100} surface.[9] Secondly, the acetate ligands bind differently to the surfaces. On the

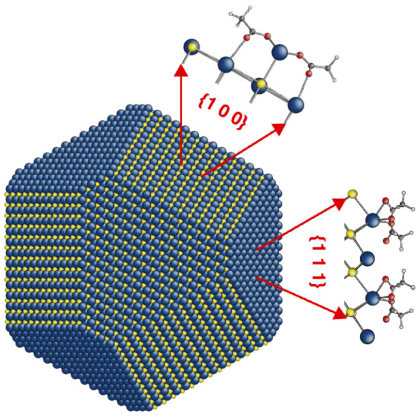


Figure 4.13: DFT calculation showing the binding of acetate ligands to the {111} and {100} facets of PbS nanoparticles. Cations (Pb) are blue and anions (S) are yellow.[9]

{111} facet, the acetate ligands bond 2 at a time to alternating cations, but on the {100} faces, they form a bridge between the top layer of cations and the layer of cations underneath. Lastly, Choi *et. al.* also calculated the binding energy to

be 0.616 eV/cation and 0.962 eV/cation, for the {100} and the {111} surfaces, respectively. While these absolute numbers would not hold for similar ZnO surfaces, they would be on the same order. Thus, on ZnO, there would be little loss to desorption with binding energies of that order (roughly $25 \times k_b T$ at room temperature), and acetate ligands should offer a robust dispersion mechanism.

## 4.6 Dispersion and Spin Casting

### 4.6.1 Polyol Particles

The polyol synthesized nanoparticles, without any ligand chemistry, proved to be difficult to use further. The goal of the polyol particles was to keep organic inclusions in the film to a minimum to aid laser annealing later. Because the particles were dried in the vacuum oven before they were redispersed, precise weight percent calculations were possible and are cited for the suspensions.

Numerous solvents, mixtures of solvents, and dispersants were attempted. Some of the results of spin casting the dispersions are summarized in Figure 4.14. Early dispersions in tetrahydrofuran ($C_4H_8O$), ethanol ($C_2H_5OH$), methanol ($CH_3OH$), dichloromethane ($CH_2Cl_2$), and ethylene glycol monomethyl ether (EGME) ($C_3H_8O_2$) were somewhat successful in dispersing the particles, but the solids loading was insufficient to allow complete monolayers to form. Mixing EGME along with ethanol or ethanolamine ($C_2H_7NO$) were among the best dispersions, allowing 1-2 monolayers of particles per spin casting step. Several commercial dispersion formulations, such as Dupont® FSO-100 dispersant, were tested at various concentrations but showed only marginal

improvement over pure solvents.

Ultimately, EGME diluted with ethanol was selected as the best dispersant. Results of the mixture were roughly equivalent to the commercial dispersants with the advantage of known composition and minimal risk of electrically active impurities.

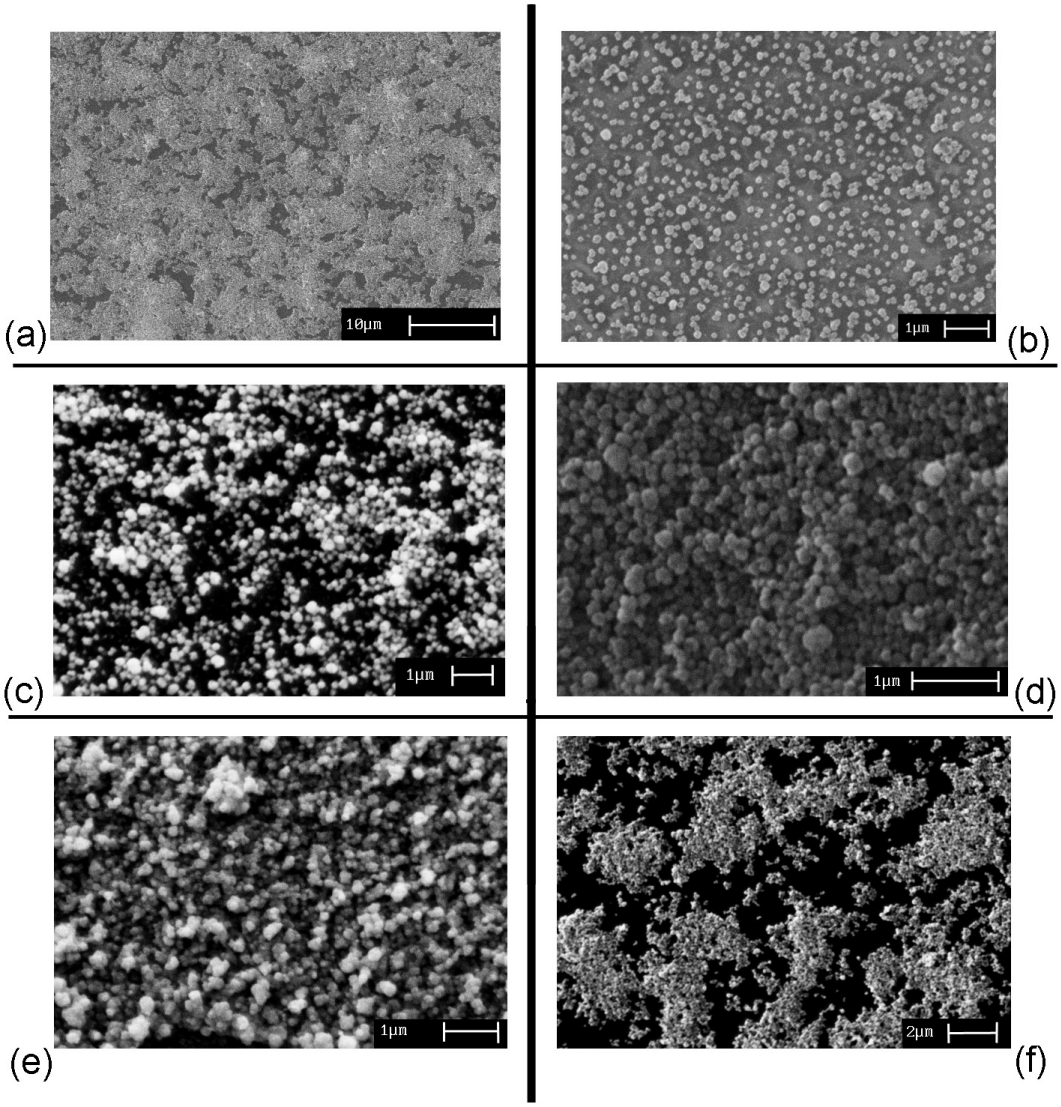


Figure 4.14: Dispersions of polyol-synthesized nanoparticles:
(a) 2 wt% ZnO in tetrahydrofuran (THF),
(b) 2 wt% ZnO in a mixture of 50 wt% ethanol (EtOH) + 50 wt% dichloromethane,
(c) 2 wt% ZnO in ethylene glycol monomethyl ether (EGME),
(d) 5 wt% ZnO in a mixture of 50 wt% EGME + 50 wt% EtOH,
(e) 5 wt% ZnO in a mixture of 90 wt% EGME + 10 wt% ethanolamine,
(f) 5 wt% ZnO in a mixture of 99.9 wt% ethanol + 0.1 wt% Dupont® FSO-100 dispersant

### 4.6.2 Sol-gel Particles

For the particles synthsized via sol-gel with the acetate capping ligands, dispersion was more straight forward. The particles were centrifuged a final time, and the supernatant was poured off, leaving a small amount of methanol and the particles. While the nanoparticles were not stable in water or simple alcohols, common general solvents like dimethylformamide (DMF) and dimethylsulfoxide (DMSO) were moderately successful in suspending the particles uniformly. However, the suspensions would become cloudy and precipitate out within hours without agitation. Polar aprotic solvents such as fluorocarbons (dichloromethane and chloroform) and ethers (tetrahydrofuran and EGME) were generally the most successful. Ultimately, chloroform (Aldrich # 288306) was added to disperse the particles, yielding approximately 10-15 mL of solution containing 5-10 wt% ZnO nanoparticles for each synthesis. The suspension was optically clear and stable for several weeks.

The resulting suspensions were filtered and deposited on substrates dropwise. Virtually all of the suspensions were spun cast at 1000 rpm for 30 sec. Lower spinning rates caused large scale inhomogenities in thickness and higher spin rates only thinned the final spun-on films. The resulting film was baked on a hotplate in air at 90°C for 60 seconds to remove residual solvent. The results are shown in Figure 4.15. The image shows no voiding, gaps, or steps; it appears, to the resolution of the SEM, to be flat except for surface debris. The green films were later determined to be 100-150 nm in thickness per spin cast, contigent on the solids loading in the particular suspension. Thicker films were formed by sequentially building up spun cast layers. This technique offered diminishing returns as materials restrictions prevented spinning in a cleanroom

enviroment. Two to three coatings were optimal, leading to relatively thick green film (200 – 400 nm). Additional coatings would increase the chance of debris being incorporated into the film and disrupt spinning of subsequent layers.

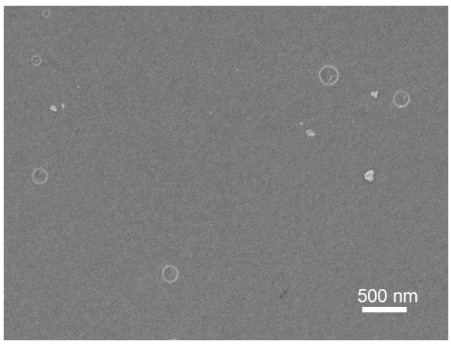


Figure 4.15: As-spun (1000 rpm, 30 sec) sol-gel particles under SEM. The surface showed no remarkable features such as voiding, steps or inclusions, indicating excellent dispersion and spinning parameters

Due to higher solids loading and more stable suspensions allowed by using the smaller sol-gel synthesized particles capped with acetate ligands, most of the subsequent annealing experiments used the smaller sol-gel fabricated ZnO nanoparticles.

## 4.7 Electrophoretic Deposition

Electrophoretic deposition is a novel way to deposit nanoparticles that could be a low-cost, material efficient, and high-throughput solution process compatible with flexible substrates. The process is adapted from a biological analysis technique to separate macromolecules by charge. With the acetate capping ligands, the sol-gel synthesized nanoparticles are charged and only slightly

larger than the radius of gyration of a biological macromolecule. Therefore, much of the knowledge can be leveraged to create high-quality inorganic films. The work reported here draws heavily on related work by the Dickerson group at Vanderbilt University. They have demostrated electrophoretic deposition using a number of different nanoparticles and structured oligmers on several different substrates.[37] [54] [17] A schematic of the technique is shown in Figure 4.16.

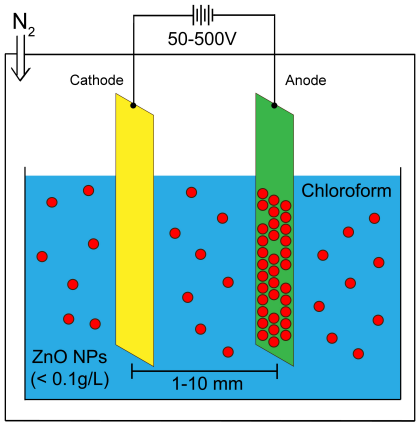


Figure 4.16: Schematic of nanoparticle electrophoretic deposition. Large electric fields between the plates deposit the charged particles on the surface, where they are neutralized and adhere to the substrate. Typical deposition rates were 50-200 nm/min.

The nanoparticle supension in the reservoir is orders of magnitude more dilute than the suspension for spin casting, only about 0.1 g/L. The plate capacitor, consisting of two heavily doped silicon wafers for the anode and the cathode, was dipped into the solution and subjected to a DC electric field. The space between the electrodes was maintained by a 4.7 mm Teflon spacer. A high voltage DC source, in this case a repurposed photomultiplier source, provided the electric field. The system was enclosed to reduce contamination from particulates in the air, evaporation of the solvent, and to control the drying of the

solvent. The partial pressure of the solvent over the solution was controlled by regulated input of a slight overpressure of dry nitrogen gas. In chloroform, the negatively charged particles, by virtue of the stabilizing ligand chemistry, was attracted to and oxidized by the anode. Different solvents (DMF and DMSO) were investigated that generated different behavior. In DMF, deposition occured on the cathode, while in DMSO, deposition was observed simultaneously on both electrodes. Chloroform was found to create the most stable suspensions and reproducible films.

### 4.7.1 Deposition

The deposition rate in electophoresis is controlled by the flux of particles onto the surface of the electrode. The flux is the product of the particle concentration and the steady state particle velocity. The steady state velocity is given by the Henry equation:

$$\nu = \mu E = \frac{2\epsilon\zeta \cdot f_H(\kappa a)}{3\eta} \tag{4.4}$$

where $\epsilon$ is the dielectric constant of the solvent, $\eta$ is the viscosity of the solvent, $\zeta$ is the zeta potential, and $f_H$ is the Henry function.[37] [1] The Henry function is the product of the Debye length ($\kappa$) with the units of inverse length and the particle size ($a$). The result is a unitless value that is a ratio of the particle size to the double layer thickness. Two limiting cases for the ratio are typically used: the Huckle approximation and the Smoluchowksi approximation. The Huckle approximation is useful for non-polar solvents and assumes the double layer is very thick compared to the particle size. Conversely, the Smoluchowski approximation applies to aqueous solutions, and it assumes the double layer is very thin. Because chloroform is only slightly polar, the value for the Henry

function is likely not satified by either approximation. Attempts to measure the zeta potential and particle mobility directly using the Malvern zeta sizer used for DLS measurements were unsuccessful.

For acetate capped ZnO particles in chloroform, it was found that voltages of 60 to 120 V generated reasonable deposition rates of 50-200 nm/min, and which scaled quadratically with voltage (see Figure 4.17). The Henry equation, (Equation 4.4) states that deposition rate only scales linearly with voltage. This implies that the Henry function in this particular case may also be a function of applied voltage. More investigation with lower applied voltages, lower solids loading, and various solvents would be required to make a definitive conclusion. With typical deposition times of 2-5 minutes, 1 micron films were easily achieved, at typical voltages significantly lower than those reported in literature. This is probably due to the low viscosity of the solvent, as compared to non-polar hydrocarbons, and the small hydrodynamic radius of the particles. The particles were relatively small, 7 nm, and the acetate capping ligands were also small, unlike the larger organic molecules used in the literature.

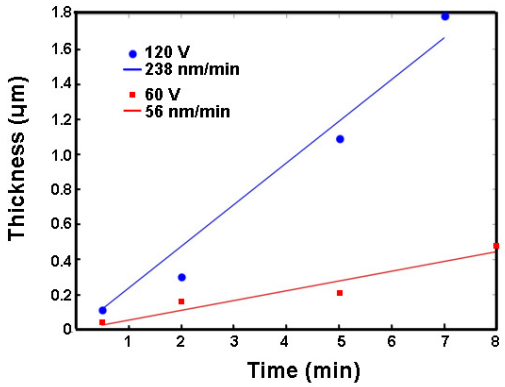


Figure 4.17: Deposition rate for 0.1 g/L ZnO nanoparticles in chloroform at 60 V and 120 V.

### 4.7.2 Film Drying and Cracking

One of the main challenges to overcome was volume shrinkage during drying, which caused large-scale cracking and delamination from the substrate. As one would expect, thicker films presented more of a problem than thin films. Figure 4.18 exhibits the severity of the problem for a two micron film with room temperature drying in air.

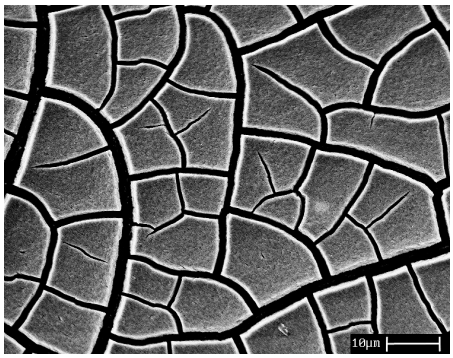


Figure 4.18: Unacceptable ZnO film cracking from an early sample of electrophorically deposited film dried in air.

Controlled evaporation of the solvent was necessary to reduce film cracking, so an enclosure was built around the deposition apparatus to control the atmosphere around the samples. During and immediately after deposition, the solvent was allowed to reach equilibrium with the gas in the chamber, meaning the partial pressure of the gas was roughly equal to the vapor pressure of the solvent at room temperature. In order to dry the film, dry nitrogen was introduced slowly (controlled via a flow meter) to lower the partial pressure of the solvent and initiate drying. Over 10 minutes the flow of nitrogen was gradually increased until the films were dry. With controlled drying, cracking was not eliminated completely, but films up to 300 nm thick were produced that were suitable for laser annealing (see Figure 4.19 (a) and (b)).

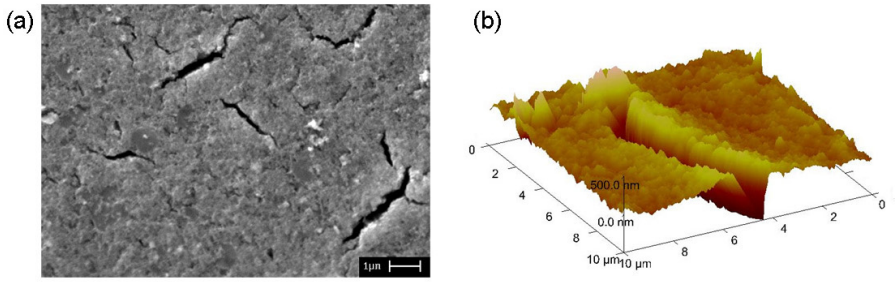


Figure 4.19: Results of electrophoretic deposition. (a) SEM showing the green film after controlled drying (approximate film thickness is 300 nm). (b) Atomic Force Microscopy (AFM) 3D reconstruction (isometric view) showing cracking.

### 4.7.3 Lithographically Patterned Depostion

Because of materials restrictions in the cleanroom, it was necessary to pattern ZnO films before deposition, and the selective deposition on conductive areas offered by electrophoresis was a potential route. Figure 4.20 illustrates the result of the process with a lithographically defined ZnO film. The first step to creating this film was to spin, bake, expose, and develop photoresist using standard processes. In this case, Shipley 1813 was chosen because it is a well characterized i-line resist. After developing the pattern, the wafer was hard baked at 140°C for 10 minutes to increase its solvent resistance. Electrophoresis was performed for 2 minutes at 90 V, and the sample was dried for 10 minutes. Areas devoid of resist and conductive (heavily doped substrate) accumulated nanoparticles as usual, but the areas covered in photoresist did not conduct, thus, no deposition occured. The wafer was immersed in acetone for several minutes to remove the photoresist, and what remained was a negative image of the photoresist in ZnO nanoparticles. The pattern fidelity was excellent, but film uniformity was poor. Edges of the film which abutted the photoresist were

significantly thicker ( 20% ) than the bulk film away from the edge, likely due to the transport-limited edge effects. The edges had access to greater volume of solution with the greater flux yielding thicker films.

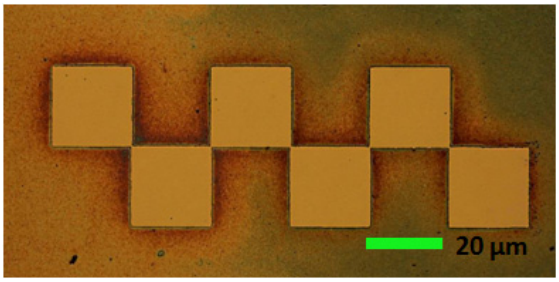


Figure 4.20: Optical image of lithographically patterned electorphoretic deposition, negative image of offset 20 micron blocks. The coloration is the optical interference pattern from the film, and it indicates a large thickness increase near the edges of the pattern.

A significant drawback to this technique was that the photoresist was slightly soluble in chloroform, and small concentrations of the dissolved photoresist poisoned the solution. After one deposition, the entire reservoir of nanoparticles and solvent would have to be discarded, and suspension could not be reused. One potential solution would have been a ligand exchange that would make the particles stable in an aqueous solution. A different resist system with greater solvent resistance to chloroform might have also been more successful, but selecting a solvent and process capable of stripping the resist after deposition without dissolving or otherwise modifying the nanoparticle films would be difficult.

While electrophoretic deposition showed many benefits for a roll-to-roll flexible process, ultimately the technique was not used in this study for nanoparticle deposition for TFTs, as it required a deposition substrate that was conductive. If the substrate could not dissipate the charge of the deposited par-

ticles, additional particles would be screened from the field and would not adhere. Although a thin seed layer would have been sufficient, the geometry of backagate TFTs made this untenable. Any seed layer would have been a low resistivity electrical path in parallel with the semiconductor channel. The off current for devices fabricated in this manner would have been high and the device performance would suffer. However, an AC deposition technique that resolves the charging problem may make this deposition technique viable for future flexible substrates.

CHAPTER 5

# ZINC OXIDE NANOPARTICLE FILMS

## 5.1 Introduction

In order to utilize nanoparticle inks as precursor materials for thin film electronics, a thermal annealing step is required. Flexible TFTs create a dilemma for conventional annealing techniques such as furnace and rapid thermal annealing (RTA), as polymers like PET and PEN are sensitive to temperatures in excess of 200°C. In order to realize the performance benefits of inorganic semiconductors including high mobility, low leakage, and environmental stability, the semiconductor inks must be annealed at temperatures at or above 600°C. The anneal must volatilize any remaining solvent, decompose the organic stabilizing ligands (referred to as calcining), and sinter the nanoparticles into a mechanically and electrically cohesive film. As discussed earlier, laser annealing is ideally suited to provide transient temperatures that can achieve all of these goals without exceeding the static temperature limit of the substrate.

## 5.2 Annealing Polyol Nanoparticles

The sintering behavior of polyol particles, the first ZnO particles synthesized, was studied using furnace annealing and excimer sintering. Due to the large size of the particles and the relatively low solids loading possible with the polyol particle dispersions, the goal was not to develop high quality densified films per se, but rather to explore the phase space and determine the effects of excimer

annealing on ZnO.

### 5.2.1 Furnace Sintering

Prior to furnace annealing, polyol synthesized particles were dispersed in a 50:50 mixture of EGME and ethanol at a solids loading of 5 wt%. The films were cast as described in the previous chapter, at 1000 rpm for 60 seconds and baked out at 90°C, with the cycle repeated three times. Furnace annealing of the polyol particles was performed at 1100°C for 60 mins in 100% oxygen ambient. An SEM image (Figure 5.1) of the resulting film shows significant diffusion and grain growth. The surface appears rough (although height contrast in SEM can be deceiving), consistent with the Oswald ripening.

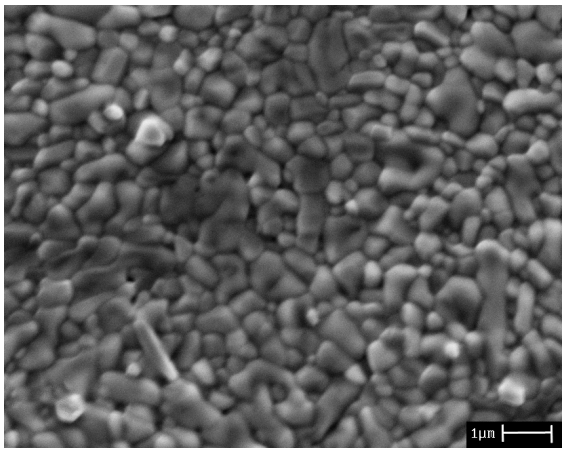


Figure 5.1: SEM image of polyol ZnO particles annealed in oxygen ambient at 1100°Cfor 1 hour. Clear signs of significant diffusion and Oswald ripening are visible; however, the surface is still rough, indicating no liquid phase transisitions.

These films showed a low resistivity of $\sim 0.95\ \Omega \cdot \text{cm}$, which indicated a high concentration of electrically active defects. At such low resistivities, these

films are unsuitable for MOS devices. Capacitance measurements showed significant leakage (milliamps) through a prototype gate dielectric, which likely resulted from diffusion of zinc into the dielectric (zinc forms a midgap state in silicon dioxide).

### 5.2.2 Excimer Sintering

Polyol synthesized particles were also annealed utilizing excimer laser irradiation, with mixed results. The TGA results (Section 4.4.3) indicated there was a small amount of retained organic material that would outgas during annealing, so it was believed that excimer annealing would be straight forward. The spin casting procedure was similar to that used for the furnace annealed samples in the previous section. They were cast at 1000 rpm for 60 seconds, baked out at 90°C, and the process was repeated 3 times to increase film thickness. The samples were annealed at various powers of 100 – 700 mJ/cm$^2$ and a range of pulse counts. The results are summarized in Figure 5.2. The unannealed film, despite the relatively large particles, showed good substrate coverage. Even at low energy, 100 mJ/cm$^2$, there is evidence of significant material loss; however the material also showed evidence of diffusion and possible melting. As the energy per pulse increased, it was evident that additional material was being ablated, but some areas appeared to form fully dense islands.

Ultimately, while this particular methodology led to films that were not uniformly sintered and showed strong tendency to form islands, several intriguing avenues were suggested by these tests. The excimer laser coupled strongly enough to the ZnO layer to cause diffusion and densification, indicating that the

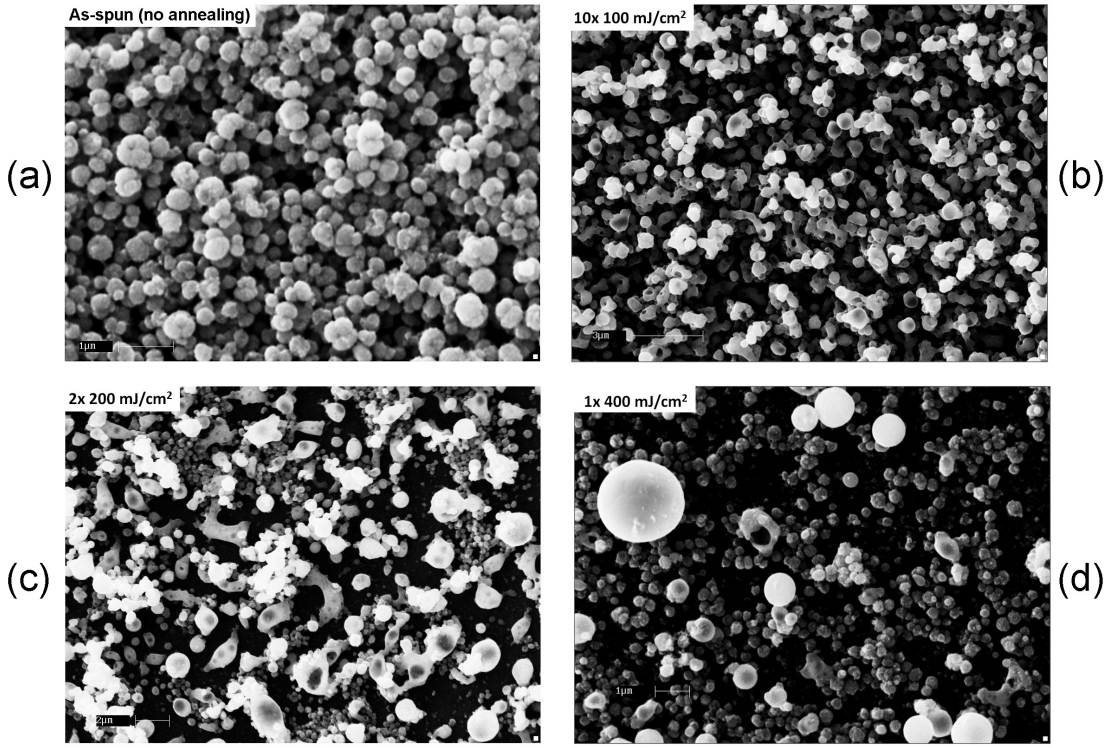


Figure 5.2: ZnO nanoparticle films annealed via excimer laser: (a) As-spun nanoparticle film with no annealing (b) 10 pulses at 100 mJ/cm$^2$, (c) 2 pulses at 200 mJ/cm$^2$, (d) 1 pulse at 400 mJ/cm$^2$

general process was viable. Additionally, the excimer laser caused significant ablation despite there being relatively little organic material in the film, suggesting that an intermediate annealing step may be required to reduce material loss during excimer annealing. Lastly, the films, particularly at higher fluences, appeared to be melting. Melting is an unexpected result because liquid ZnO is not an equilibrium phase at any temperature in air. Under static heating and in ambient air ($p_{O_2} \approx 0.21$), ZnO decomposes at 1975°C.

## 5.3 Sol-gel Particles

As suggested by the preliminary results in the last section, a different approach would be necessary to successfully anneal ZnO particles into fully densified films. Sol-gel synthesized nanoparticles were smaller and able to be suspended at higher concentrations than the polyol-particles; this increased the thickness and density of the green ZnO film. In order to better manage any outgassing or material removal, a two-step annealing process, consisting of a calcining step to remove any residual organic material followed by a high power sintering step, was attempted with significantly improved results in film morphology and electrical properties. Figure 5.3 shows a schematic of the two-step process.

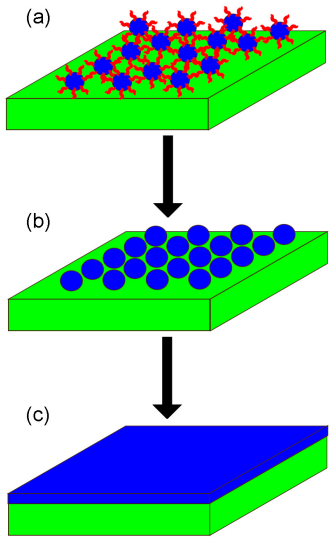


Figure 5.3: Two step nanoparticle ink annealing process (a) As-spun nanoparticle film (b) Calcining: oxygen plasma or non-melt annealing decompose the stabilizing ligands, but do not significantly alter film morphology (c) High power sintering

### 5.3.1 Calcining via $CO_2$ Laser Non-Melt Processing

These films were spun cast as previously described. ZnO particles suspended at 5 – 10 wt% in chloroform were spun cast onto oxidized silicon wafers at 1000 rpm for 30 seconds. The samples were then baked out at 90°C for 2 minutes. Next, the films were annealed with a $CO_2$ laser at 40 W and 500 $\mu$s dwell (according to the calibration methods discussed in Chapter 2, 567°C) with a track spacing of 0.11 mm. Because the non-melt laser system was a scanning system, each track was overlayed with the previous to produce a uniform time at temperature profile for the entire annealing area. Annealing at temperatures in excess of 700°C by accessing longer dwell times or higher beam power caused visible film damage and surface roughening.

Comparing the $CO_2$ laser annealed sample in Figure 5.4 with the as-spun sample in Figure 4.15, they look similar to each other, except for the void spaces. As supported by X-ray diffraction and FTIR measurements (below), there is little morphological change to the particles themselves; however, the acetate ligands are decomposed by annealing. Because the ligands represent a significant volume fraction ($\approx$ 11 vol% by theoretical calculations), the void space formed once the ligands were removed is expected. The voids do not seem to adversely affect the films for subsequent processing steps.

#### XRD of Calcined Films

The x-ray diffraction offset $2\theta$ scan of a $CO_2$ laser (Figure 5.5) annealed sample was overlayed with the previously presented as-spun sample (Figure 4.11). Both traces show broad peaks corresponding to the two strongest reflections

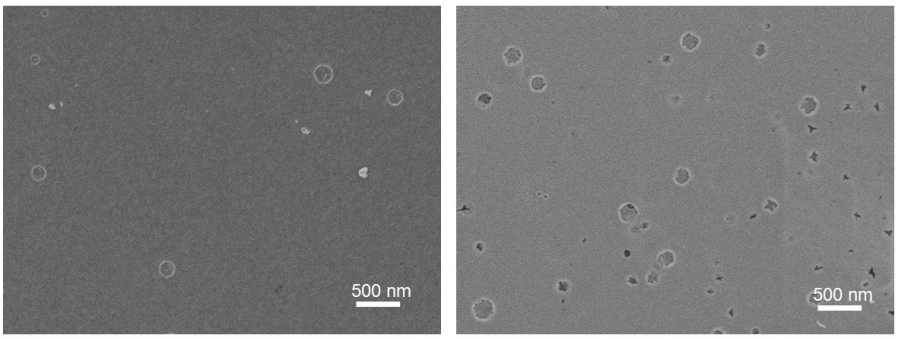


Figure 5.4: ZnO nanoparticle film (a) as-spun and (b) calcined via $CO_2$ laser, 500 $\mu$s dwell.

from crystalline wurtzite ZnO. Peak broadening indicates small crystallite size, estimated by the Debye-Scherrer method to be approximately 8 nm, which is reasonably consistent with XRD, TEM, and light scattering measurements of the precursor particles. Non-melt laser annealing did not significantly alter the microstructure of the film, though the signal-to-noise ratio does improve. The improved SNR is likely due to a purer sample, which is consistent with the organic contaminent being removed.

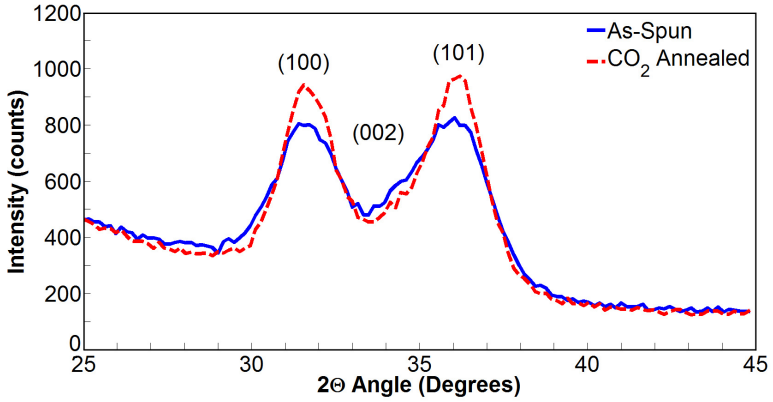


Figure 5.5: X-ray diffraction of ZnO film, as-spun and $CO_2$ annealed, 500 $\mu$s dwell

**FTIR of Calcined Films**

The primary means to directly detect the presence, and hence the removal of the ligand chemistry, was Fourier Transform Infra-Red (FTIR) spectroscopy. Like most IR spectroscopies, FTIR relies on characteristic phonon bending and stretching modes to identify organic molecules. Scans are typically performed in the mid-IR "fingerprint" region from wavelengths of 2.5 $\mu$m to 16 $\mu$m, which is typically expressed in wavenumbers ($1/\lambda$) of 4000 $cm^{-1}$ to 600 $cm^{-1}$, respectively. The most prominent absorption peaks for acetate are asymmetric bond stretching modes at 1580 – 1550 $cm^{-1}$ and 1460 – 1410 $cm^{-1}$, but these peaks can shift slightly, depending on the environment around the molecule.

The instrument used to generate the absorption spectra was a Brueker Hyperion FTIR microscope connected to a Brueker Tensor 27 nitrogen-cooled detector in simple reflection mode. The sample spot size can be varied from 20 – 250 $\mu$m, and was typically kept around 200 $\mu$m for these measurements, depending on sample conditions. Nitrogen was flowed over the sample to reduce variations due to water vapor in the beam path. Despite meticulous care to remove the water in background measurements, much of the scatter seen in the extracted FTIR plots is due to water vapor. The FTIR was used to measure samples annealed for 1000, 500, and 250 $\mu$s at a range of powers from zero to damage threshold for each dwell time. The full analysis is presented for the 1000 $\mu$s dwell in Figure 5.6. To aid explanation of the data, only the final integrated area graphs are presented for 500 $\mu$s and 250 $\mu$s dwells.

The small insets along the top and right side of the figure are the raw FTIR spectra for various annealing powers from 1300 – 1600 $cm^{-1}$. Note that as the annealing power increases from 15 W to 39 W, which corresponds to a peak

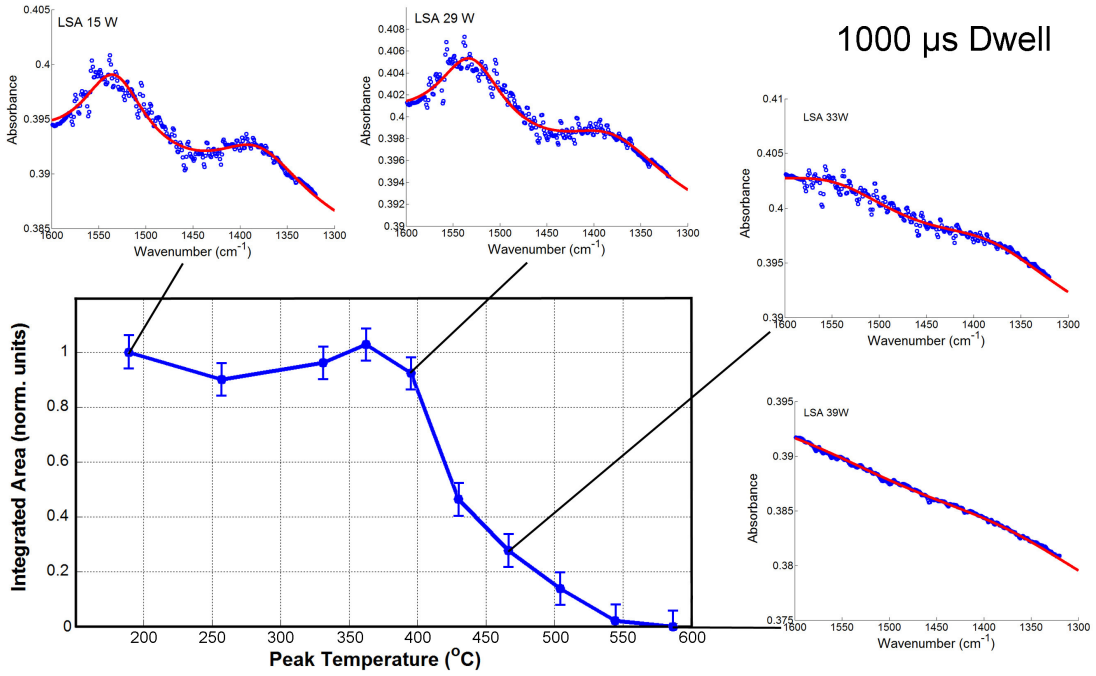


Figure 5.6: FTIR analysis of the integrated area of the paired acetate peaks at 1380 $cm^{-1}$ and 1520 $cm^{-1}$, ZnO film anneal with $CO_2$ laser, 1000 $\mu$s dwell

temperature of 280°C increasing to 680°C, the amplitude of the characteristic acetate peaks decrease. To quantify the loss of ligand chemistry, a fit (shown in red) of the form:

$$f(x) = \frac{A}{\pi\left((x-x_1)^2 + A^2\right)} + \frac{B}{\pi\left((x-x_2)^2 + B^2\right)} + Cx + D \tag{5.1}$$

was integrated for each power tested and normalized to the lowest non-zero $CO_2$ annealing power. The results are presented in the large bottom left graph. The data was not normalized to the as-spun condition because adsorbed water on the surface interfered with the fit. The lowest laser power was sufficient to evaporate any adsorbed water and provide a baseline relatively independent of ambient humidity during spin casting. This data showed complete ligand removal around 500°C, which is higher than the normal decomposition temper-

ature (275-400°C, see TGA of sol-gel synthesized particles in Figure 4.10) under conventional heating, but similar results have been shown for unrelated research in the Thompson group by Jung *et. al.*[28] during laser post exposure bake of polymer photoresists. The polymer photoresists can survive undamaged under non-melt laser annealing at transient temperatures several hundred degrees Celsius above the static decomposition temperature of the polymer.

In a similar way, the acetate loss for 500 $\mu$s and 250 $\mu$s (Figure 5.7) dwells are shown in Figure 5.7, was quantified as a function of temperature. As dwell time decreased, the peak temperature required to completely remove the ligands increased. At 1000 $\mu$s dwells, the ligands were removed by 500°C, but temperatures in excess of 650°C and 770°C were necessary to remove the ligands at 500 $\mu$s and 250 $\mu$s, respectively. This data is also consistent with the work of Jung *et. al.*.

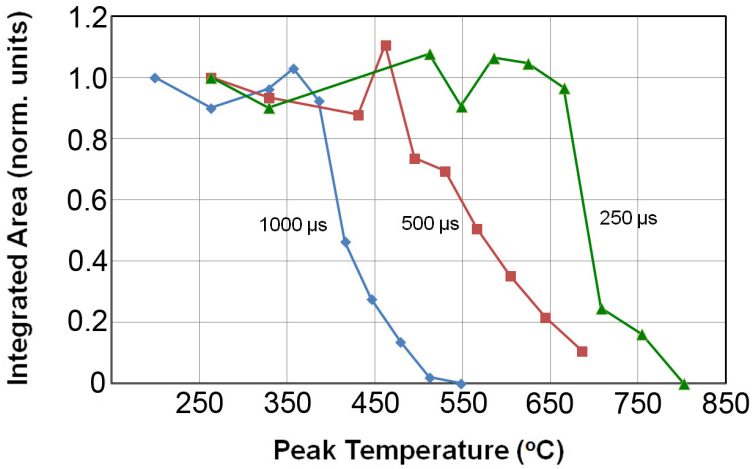


Figure 5.7: FTIR analysis of the integrated area of the paired acetate peaks at 1380 $cm^{-1}$ and 1520 $cm^{-1}$ for ZnO films annealed with a $CO_2$ laser at 1000 $\mu$s dwell, 500 $\mu$s dwell, and 250 $\mu$s dwell.

### 5.3.2 Calcining via Oxygen Plasma Treatment

While thermal decomposition is one method to remove organic compounds from thin films, another method is chemical decomposition with a highly active species. While not strictly an annealing process, oxygen plasma treatment was found to be functionally equivalent as a calcining step for the green nanoparticle films, as suggested by Glass *et. al.*[14] and Sohn *et. al.*[53] The room temperature process takes place in a highly oxidizing plasma, in which oxygen radicals react with any organic material to form gaseous carbon dioxide and water. The organic material is removed without high temperature or a reducing environment which would increase the defectivity of the zinc oxide films. The oxygen plasma treatment is well able to decompose a monolayer of small organic molecules. There are strong process advantages to substituting an oxygen plasma treatment for a scanning laser annealing step. One, it can be done at room temperature. Two, because it is at room temperature, it does not introduce the vacancies or interstitial defects associated with temperature in non-oxidizing environments. Three, it is much simpler to integrate into a roll to roll system than a $CO_2$ laser system. Oxygen plasma offers higher throughput and better uniformity over large areas than a scanning laser. Finally, oxygen plasma works regardless of the type of substrate; depending on the wavelength of the non-melt laser system, certain substrates may not strongly couple to the laser energy.[23]

To test the hypothesis, oxidized silicon substrates were coated with ZnO nanoparticle films using the spin coating process described above for sol-gel synthesize particles. The films were exposed to oxygen plasma for 5 minutes at 100 W, 200 W, and 400 W in the Glenn 100 asher on a floating shelf. The

films were imaged with SEM to examine the morphology and analyzed with reflection FTIR to compare the efficacy of oxygen plasma to non-melt annealing for ligand removal. Figure 5.8 shows the film calcined in oxygen plasma for 5 minutes at 200 W. It is remarkably similar in qualitative appearance to the films annealed by $CO_2$ laser. The film has the same voids associated with loss of the acetate volume fraction, and the particles themselves look unaltered. There was no damage to the film evident after the oxygen plasma treatment.

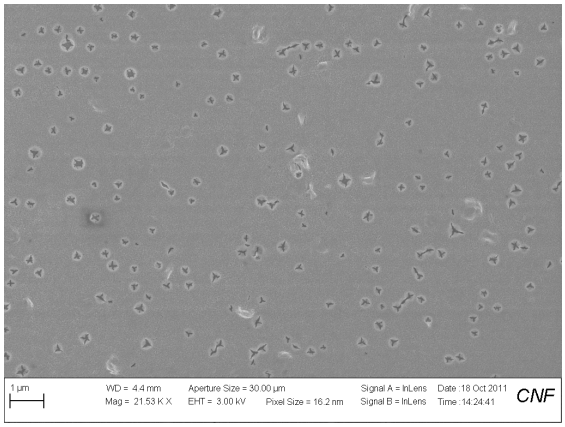


Figure 5.8: ZnO nanoparticle film treated 200 W oxygen plasma for 5 mins. Void space is due to decomposition of ligand chemistry. The morphology of the film is very similar to the results of non-melt laser annealing.

The FTIR analysis (shown in Figure 5.9) was performed in a similar manner to the $CO_2$ laser annealing analysis, and it confirmed that the acetate ligands were removed by oxygen plasma. Simple reflection mode was used to sample through the thickness of the calcined films. The Glenn asher successfully removed virtually all traces of acetate for all powers tested 100 – 400 W. In order to ensure that all of the organic material was removed, subsequent samples to be sintered by high power excimer laser were treated with oxygen plasma for 5 minutes at 200 W.

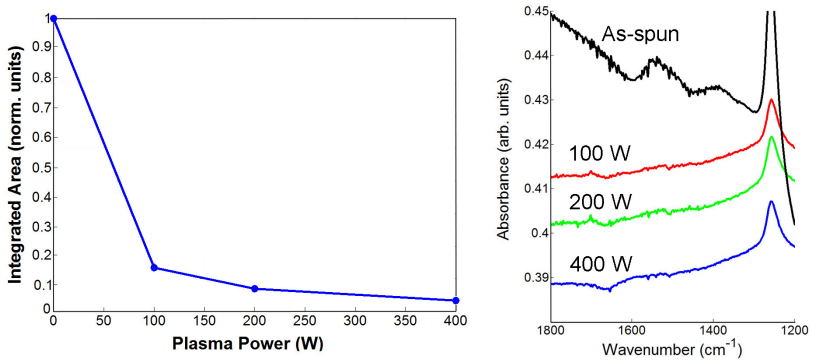


Figure 5.9: FTIR analysis of ZnO films calcined in oxygen plasma for 5 minutes at the indicated powers. The as-spun sample is included for comparison. For every power tested, nearly all of the acetate ligands were removed after 5 minutes.

The electrical conductivity of the calcined films was examined for a wide variety of conditions. Neither the thermally calcined or the chemically calcined particles had appreciable electrical conductivity. There were few, if any, percolation paths, indicating the particles in the film were still isolated. In order to obtain measurable electrical activity the films had to be sintered. It is also possible, although less likely, that the conductivity was too low to measure with the probe station configuration available. Attempts to lithographically pattern metal contacts to reduce contact resistance caused signficant material removal, reducing film thickness by greater than 50%, indicating that the film had poor adhesion to the substrate.

### 5.3.3 Excimer Laser Sintering

Once the organic material was removed from the sol-gel synthesized nanoparticle films, they were exposed to a high-power excimer laser sintering step. Pulses were varied in number and fluence over the phase space.

Figure 5.10 shows a selection of images from films annealed at fluences from 75 mJ/cm$^2$ to 250 mJ/cm$^2$. In contrast to the polyol particles, little ablation or voids were observed after excimer annealing below 250 mJ/cm$^2$, though some surface roughening was observed at higher fluences. Above 300 mJ/cm$^2$, the films degraded in quality due to delamination and cracking, likely due to high thermal gradients. Uniformity was highest near 200 mJ/cm$^2$. The films appeared extremely flat and featureless, with little indication that the film had been made up of discrete crystallites.

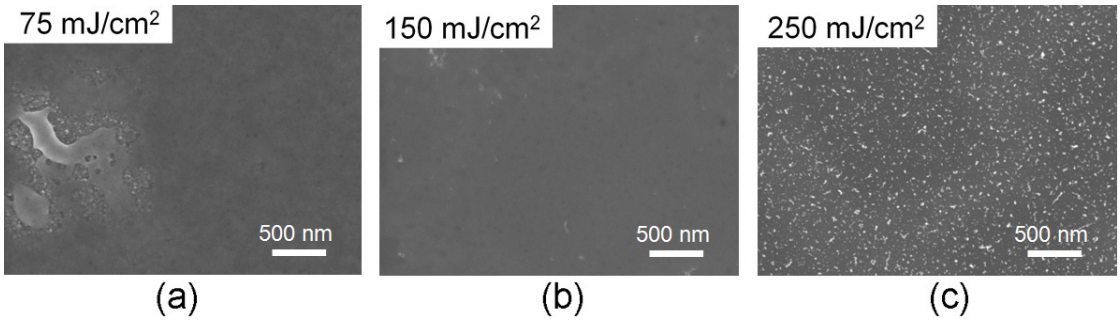


Figure 5.10: SEM images of excimer annealed ZnO films, (a) 75 mJ/cm$^2$ , (b) 150 mJ/cm$^2$ , and (c) 250 mJ/cm$^2$

**Structure Properties of Calcined and Sintered Films**

Figure 5.11 shows the effect of excimer annealing on the crystal structure of the films. Films annealed at 75 mJ/cm$^2$ transformed to large polycrystalline grains with an estimated size of 240 nm, using the Debye-Sherrer method. The peaks indentified are consistent with the 3 strongest peaks of wurtzite zinc oxide. However, the relative intensity of the peaks were inconsistent with a randomly oriented grain structure. In the films, the relative intensity of the (100) and the (101) peaks was approximately equal. MDI JADE Powder diffraction

files indicate that the (101) peak should be almost twice the height of the (100) peak.[22] Usually this is an indication of texture, but a cursory 2-D X-ray scan with a general area diffraction detector (GADDS) showed no obvious texture in the film. At high fluences, films developed an amorphous character, becoming completely amorphous above 250 mJ/cm$^2$. These results suggest it is possible to melt ZnO films in ambient conditions using short duration pulses of an excimer laser. Under normal static heating, ZnO decomposes into zinc and oxygen vapor above 1900°C. Additionally, this data shows it is possible to covert a polycrystalline ZnO film into the preferred amorphous phase using laser irradiation.

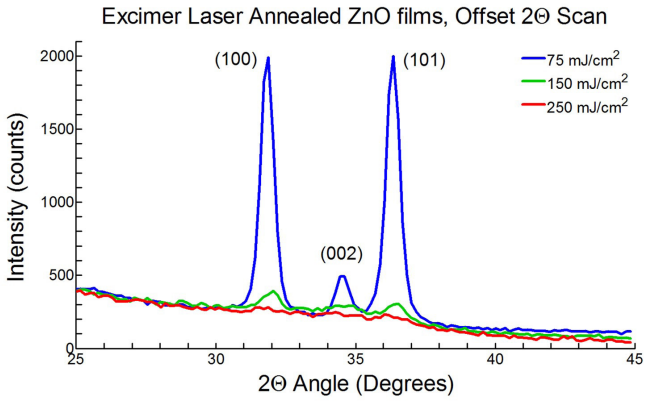


Figure 5.11: X-ray diffraction of ZnO film, excimer sintered at 75 mJ/cm$^2$ , 150 mJ/cm$^2$ , and 250 mJ/cm$^2$

There was concern that ablation at the higher fluences could have removed the entire ZnO film. In order to confirm that a ZnO film was still present and to assess defects, such as cracking or voiding, a Hitachi FB2000A focused ion beam (FIB) was used to cut a window through the film to observe the cross section in SEM. The films were annealed with a $CO_2$ laser at 40 W and 0.5 ms dwell (570°C) and sintered with an excimer laser at 200 mJ/cm$^2$ for 5 shots. The FIB etched out a 512 micron x 512 micron area to 1 micron in depth. The window was sufficient

to expose the cross section of the ZnO film, the oxide, and the silicon below it. Once the material was removed, the area of interest was polished using a quick low-fluence pass with the FIB to improve the surface quality (hence the ZnO being set back from the edge of the $SiO_2$). The SEM image in Figure 5.12 was taken with the stage at a $45^o$ tilt to examine the film in cross section. Accounting for the tilt, the ZnO film was measured to be 140 nm thick. As initial green films were 200 – 300 nm, densification and some material loss was observed, but a majority of the film remained intact at high fluences. The film appeared uniform throughout with no apparent cracking or voids. This data confirms the presence of ZnO and the X-ray identification of laser-induced amorphization at high fluences.

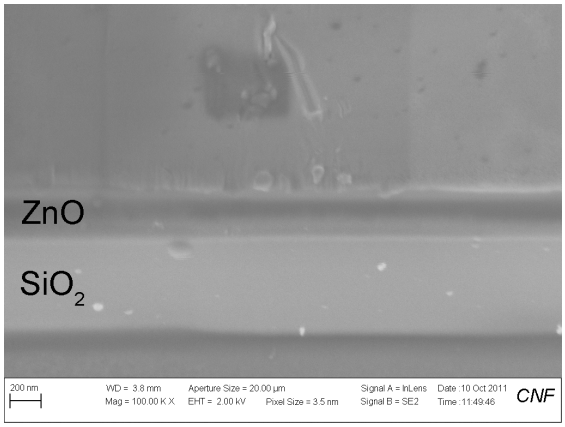


Figure 5.12: SEM image of a fully sintered ZnO film on silicon dioxide, showing uniformity throughout the thickness. The cross-section was exposed by FIB and imaged at a tilt of 45° to the normal.

**Electronic Properties of Calcined and Sintered Films**

To measure the resistivity of the nanoparticle films, samples were calcined by a $CO_2$ laser system at 40 W, 500 $\mu$s dwell and then sintered by the excimer

laser irradiation at 200 – 250 mJ/cm$^2$. The final film thickness was measured by several profilometry line scans to be 65-77 nm thick, with an average thickness of 68 nm. The resistivity was measured using a 4-point probe configuration with current-voltage sweeps. Figure 5.13 indicates that all of these films were conductive, with resistivities in the $10^{-1}$ to $10^{-2}$ Ω-cm range. For comparison, indium-tin oxide (ITO), a common doped-oxide conductor, typically has a resistivity of $2 \times 10^{-4}$ Ω-cm.

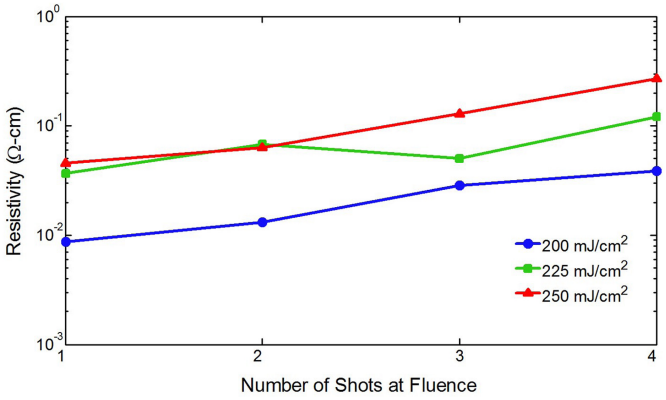


Figure 5.13: Resistivity measurements of ZnO films calcined via $CO_2$ laser at 40 W, 500 $\mu$s dwell and sintered via excimer pulsed laser at 200 – 250 mJ/cm$^2$

Films should have been nominally undoped with high resistivity. The observed low resistivities indicated that either the LSA calcining or excimer sintering introduced a large number of defects, likely due to oxygen vacancies or zinc interstitials created by high temperature heating in air. With increasing time at temperature (i.e. more shots or higher fluence), the resistivity increases slightly. Although there are several potential reasons for the increased resistivity, a likely cause is increased damage from the excimer irradiation reducing the mobility without compensating increases in the free carrier concentration. These trends contradict excimer sintering of magnetron sputtered ZnO by Mal *et. al.* where

they observed a decrease in resistivity as a function of repeated laser pulses at a fluence of 200 mJ/cm$^2$.[38]

With resistivities this low, it is not feasible to fabricate logic devices from films; however, these results are still interesting because Al doped ZnO is an inexpensive alternative to ITO, and combining Al doping with LSA annealing might result in a competitive transparent conductive oxide (TCO).

Films calcined under oxygen plasma showed resistivities 3-5 orders of magnitude higher than films calcined using LSA, as shown in Figure 5.14. These results indicate that the charged defects associated with low resistivity of the ZnO films are the result of the $CO_2$ laser calcining step and not the excimer sintering. The $CO_2$ laser annealing, despite being at moderate temperatures, is still on a time scale that permits the formation of oxygen vacancies approaching equilibrium with the partial pressure of oxygen in the ambient. Excimer laser annealing, occuring over nanosecond time scales, is much more kinetically limited and there is insufficient time to substantially change the composition.

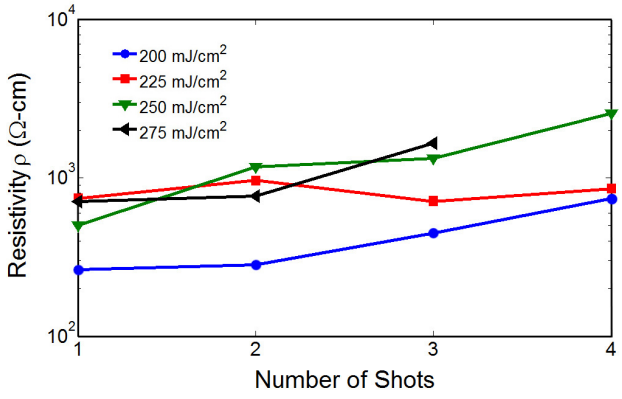


Figure 5.14: Resistivity measurements of ZnO films calcined via oxygen plasma at 200 W for 5 minutes and sintered via excimer pulsed laser at 200 – 275 mJ/cm$^2$

**Excimer Laser Sintering Temperature Measurement**

To estimate the temperature during excimer annealing, a method described by Kittl *et. al.* was attempted.[30] The sample configuration for these measurements is shown schematically in Figure 5.15. Fused silica substrates were coated with LPCVD poly-Si (80 nm) and LPCVD silicon nitride (50 nm). The ZnO films were spun on as described earlier, followed by oxygen plasma treatment at 200 W for 5 minutes. The excimer laser was incident from the backside (through the transparent fused silica) at a range of powers sufficient to melt the poly-Si film for various durations. A reflectivity monitor detected the change in reflectivity associated with the solid to liquid transition in the silicon, providing a quantitative measurement of the melt duration. The silicon here acts as a susceptor for the excimer energy, but because the thickness of the fused silica is 200 microns, the entire surface, including the ZnO film, is essentially isothermal with the Si film. Therefore the ZnO film was at approximately the silicon melt temperature for the duration of the melt. Below the silicon melt threshold, the behavior of the ZnO could be observed as a function of the peak temperature (linearly extrapolated from the melt temperature). Above the melt threshold, the behavior is observed as a function of time at 1410°C, the melting temperature of silicon. After annealing, the morphology of the resulting ZnO films can be compared qualitatively to those irradiated directly with the excimer laser. The main limitation of this technique is the highest controlled annealing temperature possible is 1410°C.

Figure 5.16 shows a series of SEM images of ZnO films after backside annealing. At 180 mJ/cm$^2$, the sample showed no morphological changes. At 400 mJ/cm$^2$, the film was damaged due to delamination of the underlying lay-

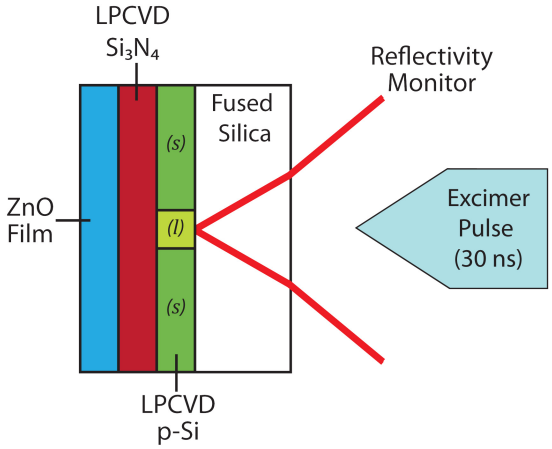


Figure 5.15: Schematic of backside annealing. The silicon layer, which has a well characterized optical characteristic during melt, absorbs the excimer energy and heats the ZnO film.

ers. In undisturbed areas of the surface where particles remain, there is no evidence of aggregation or mass transport. The data indicates that the silicon melt temperature is not sufficiently high to cause melting or recrystallization of ZnO nanoparticles, at least within the time durations accessible prior to film damage (150 ns).

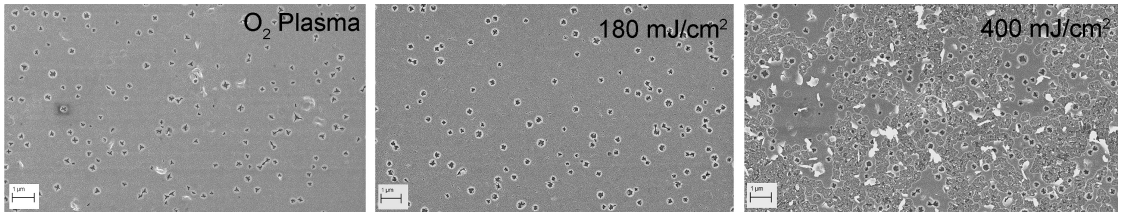


Figure 5.16: SEM images of ZnO films excimer annealed indirectly from the backside. (a) Pristine film calcined via $O_2$ plasma treatment, (b) films annealed at 180 mJ/cm$^2$ (corresponding to 1410°C for approximately 75 ns) with no morphology change, (c) film damage due to delamination of the underlying silicon and nitride layers at a fluence of 400 mJ/cm$^2$ (substantial overheating of the silicon)

To access higher temperatures, the poly-Si film was replaced with molybdenum, a higher melting point material. However, the nitride film had very poor adhesion to the molybdenum and delaminated even before ZnO nanoparticles could be spun on.

The temperature of the ZnO during laser sintering was also estimated from the front-side irradiation experiments. We assume that the incident excimer energy is converted to heat within the ZnO film, as it strongly couples to the excimer energy at 308 nm and is on the order of 100 nm thick. Given an absorption length of 100 nm, 63% of the laser energy is absorbed directly by the ZnO. Given the absorbing volume of $1 \times 10^{-5}$ cm$^3$ and a molar heat capacity of ZnO of 50 J/K-mol over the temperature range,[19] an upper limit to the amorphization temperature of ZnO can be obtained:

$$\Delta T \approx (0.63)\, \frac{M_{ZnO} \times E_{excimer}}{V \times \rho_{ZnO} \times C_{p-ZnO}} \tag{5.2}$$

$$= (0.63)\, \frac{\left(81.4084 \text{ g/mol}\right)(0.15 \text{ J})}{\left(1 \times 10^{-5} \text{ cm}^3\right)\left(5.675 \text{ g/cm}^3\right)(50 \text{ J/mol-K})} \tag{5.3}$$

$$= 2720 \text{ K} \tag{5.4}$$

While this temperature would be reduced by the thermal conduction of the heat from the particles into the substrate and by the enthalpy of melting of ZnO (unknown), the result indicates that the beam can heat the ZnO to 2720 K in 30 ns, likely sufficient to melt the ZnO. From the temperature experiments and estimate above, a lower bound for the maximum temperature is 1410°C and an upper bound of approximately 3000°C.

Various sources have attempted to estimate the temperature and pressure conditions under which ZnO would melt, though none have been wholly successful. Modern sources suggest that the triple point for ZnO is only

slightly higher than the temperature and pressure of decomposition (1975 °C at 0.2 bar $O_2$), perhaps 2100 – 2200 °C and 2 bar.[16] [32] Because solid and liquid ZnO are incompressible phases, the Clausius-Clapeyron relation between the two phases is practically vertical, indicating that the peak excimer annealing temperature must be at least 2100-2200°C. This is consistent with the above estimates.

CHAPTER 6

# ZNO NANOPARTICLE TFTS

## 6.1 Introduction

Thin film transistors (TFTs) are the most basic element of active circuits, with Figure 6.1 showing a simple bottom-gate transistor. They are a fundamental and practical demonstration of the viability of a novel semiconductor material or process. Bottom-gate refers to the fact that the gate is on the bottom of the device and is the first structure patterned. Figure 6.1 (a) depicts a metal gate transistor, while transistors such as those in Figure 6.1 (b) use the silicon substrate as a blanket gate. The latter device is easier to simpler to fabricate for testing TFT materials. A TFT has three voltage inputs, with the source voltage ($V_s$) at ground by convention and the drain voltage ($V_{ds}$) across the conducting channel, which induces a current ($I_{ds}$). The gate voltage ($V_{gs}$) modulates source-drain current ($I_{ds}$) in either enhancement mode or depletion mode devices.

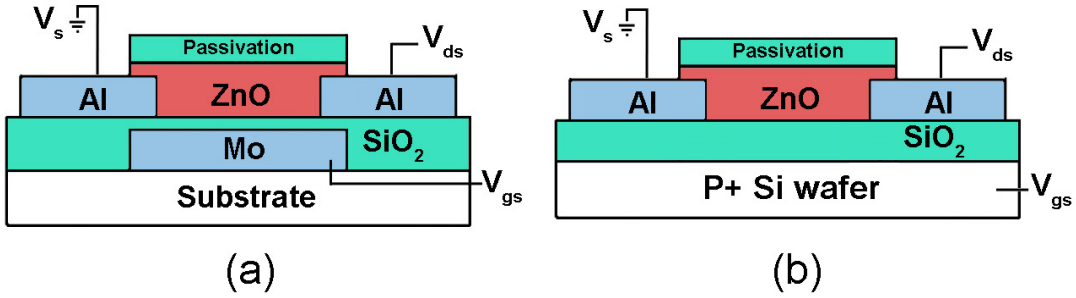


Figure 6.1: Bottom gate TFT designs (a) metal gate and (b) silicon blanket gate

TFTs are also used as diagnostic tools to determine properties of semi-

conductor materials, including threshold voltage, mobility, current on/off ratio, transconductance, and subthreshold slope. The threshold voltage ($V_T$) is the gate voltage at which the conductive channel first begins to form under the gate. It is usually extrapolated from a graph of $I_{ds}$ versus $V_{gs}$.

The mobility is a key performance metric and is given by:[48]

$$\mu_n = \frac{v_d}{E} = \frac{q\tau}{m_e} \tag{6.1}$$

where $v_d$ is drift velocity, $E$ is the electric field, $q$ is the fundemental charge, $\tau$ is the mean relaxation time between collisions, and $m_e$ is the effective mass of the electron. In a TFT, the drain current is proportional through the mobility in the triode region (linear region) via the equation:

$$I_{ds} = \frac{\mu_n \epsilon_{ox}}{t_{ox}} \frac{W}{L} \left[ (V_{gs} - V_T) V_{ds} - \frac{1}{2} V_{ds}^2 \right] \tag{6.2}$$

In the saturation region the relation changes, and the current is proportional to the mobility as:

$$I_{ds} = \frac{\mu_n \epsilon_{ox}}{2t_{ox}} \frac{W}{L} \left( V_{gs} - V_T \right)^2 \tag{6.3}$$

In both expressions, $\epsilon_{ox}$ is the dielectric constant of the gate dielectric, $t_{ox}$ is the thickness of the gate dielectric, $W$ is the transistor width, and $L$ is the transistor length.

The current on/off ratio (often abbreviated $I_{on}/I_{off}$) is another a key metric of TFT performance and is the ratio between the saturation current and the subthreshold leakage current:

$$I_{on}/I_{off} = \frac{I_{ds}^{sat}}{I_{ds}^{off}} \tag{6.4}$$

Acceptable $I_{on}/I_{off}$ ratios are at least $10^4$, but higher ratios are considered better. The ratio serves a good metric of the defect density of the semiconducting

material. Low concentration of charge defects will keep the off current low and prevent scattering of injected charges at the high current level.

The subthreshold slope is measured below the triode region, and is usually related to the concentration of defects in the gate dielectric. It is extrapolated from the logarithm of ($I_{ds}$) versus $V_{gs}$:[48]

$$\left(\frac{d}{dV_{gs}} ln(I_{ds})\right)^{-1} = \frac{k_B T}{q} ln\left[10(1+\alpha)\right] \tag{6.5}$$

where $\alpha$ is an ideality factor that is related to the parasitic capacitances of the device. The factor $\frac{k_B T}{q} ln(10)$ is a constant equal to 60 meV/decade.

While these equations and standards are well established, care must be taken with oxide semiconductor measurements as they are in a dynamic equilibrium with oxygen in the air. Consequently, oxide semiconductors have a known threshold bias instability if not fabricated and handled correctly. Wager, in a letter to the Journal of the Society for Information Display, discusses how poor measurement protocols can easily lead to misleading results.[59] He recommends the following procedures to detect hysteresis and the presence of mobile charge traps:

1. Only test mobility on a patterned channel to prevent fringing currents and an underestimation of channel width.
2. Sweep gate voltages ($\pm V_{gs}/t_{ox} \geq 2$ MV/cm) at a low source drain current ($\leq 0.1V$) to test integrity of the dielectric.
3. Perform multiple scans of the $I_{ds}$ vs. $V_{gs}$ to determine if the device is at equilibrium and if the performance characteristics are steady-state or non-steady state. The three possible cases are shown in Figure 6.2. Only steady state, equilibrium devices should be reported in literature.

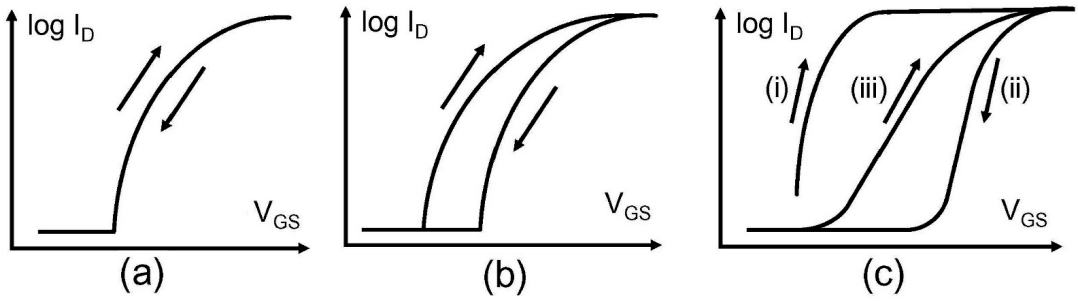


Figure 6.2: Schematic of potential transfer curves for oxide transistors (a) devices in equilibrium, (b) device not in equilibrium, but steady-state, (c) device neither in equilbrium nor steady-state.[59]

## 6.2 Procedure

Due to concerns about contamination of CMOS materials in the Center for Nanoscale Fabrication (CNF), only a subset of the tools were available for use in ZnO TFT fabrication. As such, all of the devices fabricated were bottom-gate devices. The process flow for a metal bottom-gate TFT is included in Appendix B. Modfications were made to the process flow to fabricate ZnO with silicon bottom-gates, but the mask set and general processing parameters were kept as similar as possible. Changes are noted in the description below.

Heavily-doped, p-type silicon wafers ($R_s$ = 0.01 – 0.02 Ω/□) were MOS cleaned and placed in the oxidation furnace. For metal gate devices, the wet oxidation with HCl program was was run for 30 minutes at 1000°C to grow approximately 200 nm of field oxide. Next, the gate metal (100 nm of molybdenum with 5 nm of titanium as an adhesion layer) was evaporated. The gate metal was patterned via i-line contact lithography followed by a $SF_6/CF_4$ reactive ion etch (RIE). Then, the roughly 50 nm of gate dielectric, usually PECVD silicon dioxide

or silicon nitride, was deposited. Next, the wafers were removed from the clean room for nanoparticle ink deposition and annealing. The inks were spun cast as described in Chapter 4, baked, calcined via oxygen plasma treatment, and sintered via excimer laser irradiation. Wafers were returned to the clean room for patterning and etching of the densified ZnO film using a dilute aluminum etch solution. Next the gate via was etched through the gate dielectric to expose the molybdenum gate metal. The source-drain contacts were patterned last using evaporated aluminum (with a titanium adhesion layer) and lift-off to prevent aluminum etchant from damaging the ZnO layer. A capping layer to protect the back channel could not be added due to CNF material restrictions, but the devices were stored in a constant humidity environment (21°C, 40% RH) of the cleanroom or in a nitrogen dry box.

For silicon blanket gate devices, the dry oxidation recipe with HCl was run for 30 minutes at 1000°C to grow approximately 50 nm of gate oxide. Gate patterning and the PECVD gate dielectric deposition was not required. Contact was made to the silicon wafer with the source-drain evaporated metal. All other steps were peformed similarly.

## 6.3 Results

Best results were obtained with silicon blanket gate devices using thermally grown gate dielectrics. Excimer laser sintering did induce signficant damage to the underlying gate dielectric. Silicon dioxide and silicon nitride grown via PECVD exhibited breakdown at fields of $< 10^6$ V/cm, with little correlation to excimer sintering fluence or number of shots. Leakage currents were on

the order of microamps to even milliamps for the larger area devices. While thermally grown oxide was more robust, it too would breakdown if exposed to multiple excimer sintering shots.

In devices where leakage was limited and gating behavior was observed, the device characteristics were still unstable, with no discernable trend with laser fluence or number of shots. Threshold voltage varied from -10 V to +30 V, likely due a large number of charged defects in the gate dielectric. Possible sources of these defects include the extremely high transient temperatures induced during excimer laser sintering, as well as general processing steps. Due to logistical considerations, the nanoparticle deposition and annealing steps were performed outside of the cleanroom, introducing a large number of particle and contact contaminants that could not be fully mitigated.

An example of one of the best devices is shown in Figure 6.3. This TFT ($W = 200\ \mu\text{m}, L = 20\ \mu\text{m}$) was sintered with a single excimer laser pulse at 200 mJ/cm$^2$.

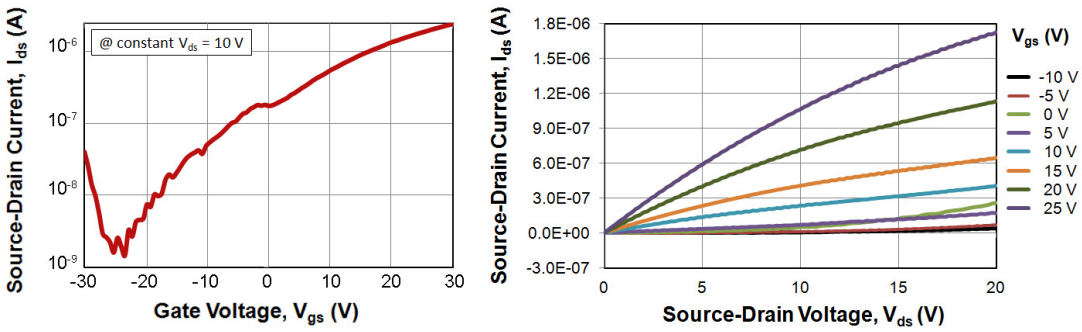


Figure 6.3: Transfer curves for a ZnO nanoparticle TFT, excimer laser annealed 200 mJ/cm$^2$, (a) $I_{ds}$ vs. $V_{gs}$ for $V_{ds} = 10$ V (b) $I_{ds}$ vs. $V_{ds}$ for $V_{gs} = -10$ to $+25$ V

The threshold voltage of approximately 7 V is somewhat higher than ideal but within acceptable limits. Using Equation 6.3, the saturated mobility of the transistor was found to be 0.26 $cm^2/Vs$, the highest value reported for any nanoparticle ink based ZnO transistor; however, it is still an order of magnitude below similar devices fabricated using PLD or sputtering. The $I_{on}/I_{off}$ ratio of $10^3$ is somewhat low, but may be limited by the unpassivated back channel. The subthreshold slope was a poor 10 V/decade, indicating extensive damage to the dielectric and the dielectric-semiconductor interface.

While the mobility was better than others of this type reported previously, its $I_{on}/I_{off}$ ratio and substhreshold slope indicate that there is signifcant damage as a result of excimer annealing. As this damage arises during the excimer laser sintering step, top gate TFTs, where the gate dielectric is deposited after sintering, would likely exhibit better performance.

# CHAPTER 7

# CONCLUSIONS

This work demonstrated an integrated process to sinter and densify zinc oxide (ZnO) films suitable for thin film tranistors (TFTs) fabricated from ZnO nanoparticle inks. The particles were synthesized, dispersed, and deposited on substrates to form green films greater than 200 nm thick. Two ZnO nanoparticle synthesis routes were demonstrated. Particles synthesized via the polyol route were approximately 100 to 200 nm in diameter. Due to a lack of capping ligands, particle agglomerates formed readily and dispersion was challenging. Particles synthesized via the sol-gel route were smaller (approximately 7 nm) and more readily dispersed due to covalently bonded capping ligands. The capped particles dispersed readily in polar aprotic solvents, such as chloroform and ethylene glycol monomethylether, and remained in solution for extended periods of time. The particles were characterized by electron microscopy, dynamic light scattering, X-ray diffraction, and thermogravometric analysis (TGA). The crystallite size was confirmed by multiple techniques and the composition was found to be wurzite ZnO. The acetate capping ligands, approximately 8 w.t.% of the dry ZnO particles, were found to be unstable at static temperatures above 300°C.

The green films were calcined to remove organic ligands via a transient thermal process, non-melt laser annealing, or via a chemical process, oxygen plasma treatment. Non-melt laser annealing heated the film on the millisecond time scale up to 700°C without film or substrate damage. Ligand removal in the films was confirmed via reflection mode FTIR. Despite the high temperature, the particles showed little evidence of diffusion or Oswald ripening. However, later four point probe measurements showed that the thermal process intro-

duced a significant concentration of electrically active defects. Conversely, films calcined via oxygen plasma treatment at room temperature showed defect concentrations orders of magnitude lower than films calcined via laser annealing.

The calcining step was followed by a high temperature sintering step performed using pulsed excimer laser irradiation. This step was shown to cause large-scale diffusion, including recrystallization, Oswald ripening, and amorphization at high enough fluences. As a function of fluence, excimer sintering created four distinct regions. Below roughly 100 $mJ/cm^2$, the nanoparticles underwent Oswald ripening, resulting in larger grained polycrystalline films. From roughly $100 - 200$ $mJ/cm^2$, the film transitioned from polycrystalline to amorphous film. In the $200-300$ $mJ/cm^2$ range, the films were fully amorphous. Above 300 $mJ/cm^2$, film damage from thermal shock and CTE mismatch caused cracking and delamination.

Data suggests that the ZnO films were melted and resolidified on time scales of 100 ns in ambient atmosphere during the laser sinter. On normal time scales, zinc oxide decomposes at 1975°C without a large overpressure of zinc and oxygen.

Finally, a bottom gate TFT was demonstrated with the ZnO nanoparticle films as the active region. The mobility reported is the highest known to date for a ZnO nanoparticle film transistor. However, many of the transistor performance metrics were limited due to damage to the gate dielectric. Electrical characterization indicated that the gate dielectric, particularly the PECVD deposited gate dielectrics, was broken down under multiple excimer laser exposures due to the extremely high transient temperatures.

**Future Work**

Moving forward, this project might be best addressed as several divergent projects. In order to determine the actual performance of laser sintered ZnO nanoparticle TFTs, top gate devices would need be fabricated. The high temperatures, probably on the order of 2000°C, of excimer sintering of ZnO coupled with zinc diffusion into the gate dielectric mean that bottom gate devices will not have comparable performance to other ZnO TFTs fabricated by physical vapor deposition methods. Top gate devices would allow excimer annealing before the deposition of the gate dielectric. Unfortunately, top gate devices could not be fabricated in the cleanroom due to concerns regarding zinc cross-contamination of CMOS devices.

The additional project would be focused on developing ZnO and its alloys as transparent conducting oxides to replace indium tin oxide (ITO). The high price and scarcity of indium make an alternative based on inexpensive materials extremely desirable. The use of non-melt $CO_2$ calcining was shown to introduce a large number of electrically active defects without changing the film's overall morphology or integrity. Undoped ZnO films treated with the laser had resistivities in the range of $10^{-2}$ to $10^{-3}$ Ω-cm. Aluminum and gallium are excellent extrinsic n-dopants in ZnO, but aluminum and gallium at their solubility limit do not increase the conductivity sufficiently to compete with ITO.[35] [34] Combining the extrinsic doping with non-melt laser processing may have synergistic effects that can deliver similar conductivities to ITO at a much lower price point, particularly as indium becomes scarcer.

A final extension of this work was proposed as a result of discussions regarding superlattices. This project would require collaboration with a research

group that could supply a variety of nanoparticle formulations for superlattices. While several groups have created superlattices of nanoparticles with unique optical or thermal properties, most of the superlattice literature consists of HR-TEM pictures of a catalog of different configurations without a strong sense of where the field is going or specific methodology to move to the next step. The full potential of the superlattice structures can not be realized because charge transport between the particles is virtually zero. Optical and thermal properties can be manipulated to great effect with superlattices because the photon and phonon states are much more extended than those of electrons and holes. To access novel electronic properties, the ligands must be removed and the nanoparticles merged into continuous structures. Coupling structured self-assembly with calcining by transient laser processing may create electronic superlattices with potentially enhanced utility and functionality.

APPENDIX A

# SOL-GEL NANOPARTICLE SYNTHESIS ROUTE

Below is the protocol for the sol-gel nanoparticle synthesis route adapted from Choi *et. al.* [9] [4]. The reaction is generally reliable and consistently yields sub-10 nm crystalline ZnO particles in a reasonable time frame, but the results are strongly dependent on minimizing residual water in the reagents and on the glassware and equipment.

**Required Chemicals:**

- Zinc acetate dihydrate (Sigma-Aldrich #379786)
- Methanol (spectroscopic grade)
- Methanol (reagent grade)
- Potassium hydroxide (Sigma-Aldrich #306568)
- Silicone oil (Sigma-Aldrich #85409) for oil baths
- Chloroform (Sigma-Aldrich # 288306)

**Lab Glassware and Equipment:**

- Temperature controlled hotplate with external probe and stirring
- Balance
- Ring stand and clamp(s)
- 500 mL volumetric flask
- 100 mL graduated cylinder
- 250 mL Erlenmeyer flask

- Small funnel
- Crystallizing dish 125x65mm
- (2) Stir bars (at least 30 mm)
- Small beaker for rinsing methanol
- Weighing dishes, scoops
- Parafilm
- Centrifuge
- (8) 50 mL centrifuge tubes with caps

**Important Notes:**

- This reaction involves highly flammable solvents and caustic chemicals. Due care and use of adaquate protection is required.
- All glassware must be clean and completely dry.
- All precautions must to taken to avoid contamination with water. If glassware or gloves get wet, replace them.
- Use spectroscopic grade methanol in the reaction. Reagent grade has too much residual water.
- The shelf life of a bottle of spectroscopic grade methanol is about 1 month if the methanol is stored under nitrogen. Longer periods will result in a failed reaction. Shelf life can be extended using 3Å molecular sieves, but be sure to filter the methanol with a $\leq 1$ $\mu$m filter before use to ensure the sieve material does not contaminate the reaction.

- When using the centrifuge, the tubes must have the same quantity of the nanoparticle suspension, or the centrifuge may become unbalanced. An unbalanced centrifuge can cause serious injury and/or permanent damage to the equipment.

**Procedure:**

1. Pour silicone oil in into the crystallizing dish to a depth of approximately 25 mm. Preheat the hotplate with the crystallizing dish on it to 60°C. Ensure the external probe is plugged in and probe tip is in the silicone bath. Failure to do so may cause the hotplate to register the wrong temperature or overheat.
2. Rinse all the glassware and stir bars with a small amount of spectroscopic grade methanol
3. Weigh out 4.26 g of zinc acetate dihydrate and pour it into the volumetric flask. Place a stir bar into the flask.
4. Measure out 190 mL of spectroscopic grade methanol into the volumetric flask and place the flask onto the oil bath. Cover the flask with Parafilm. Clamp the flask to the ring stand at the proper height. The flask should be mostly submerged, but the oil bath should not overflow. Add or remove silicone oil if necessary.
5. Weigh out approximately 2.19 g of potassium hydroxide and pour it into the Erlenmeyer flask.
6. Pour 97 mL of spectroscopic grade methanol into the Erlenmeyer flask to dissolve the potassium hydroxide completely. This will take a few minutes with agitation (stirring or ultrasonic).

7. When the temperature of the zinc acetate solution has stabilized at 60°C and the solid has completely dissolved, pour the potassium hydroxide solution into the volumetric flask (the funnel is useful here). Recover the volumetric flask with Parafilm to prevent contamination or evaporation of the solvent.
8. Within a minute, the solution will become turbid and then clear gradually as the zinc hydroxide is dissolved.
9. Allow the reaction to proceed for 2.5 to 4 hours until the solution becomes turbid again. The reaction time varies strongly on trace water concentration, so monitor the reaction after 2.5 hours for turbidity. Wait an additional 15 minutes.
10. Remove the solution from heat and allow to cool to room temperature while continuing to stir. Another stirplate or hotplate (at room temperature) is useful here.
11. When cool, pour 37.5 mL into each centrifuge tube. Ensure that the tubes have the same amount of solution so the centrifuge is not unbalanced.
12. Centrifuge the suspension at 9000 rpm for 7 minutes.
13. Pour off the excess methanol in a waste container, taking care not to pour off the particles themselves
14. Refill each tube with reagent grade methanol (approximately 30 mL) and agitate to re-suspend the particles
15. Repeat steps 12-14 at least 2 additional times to clean the particles, but on the last iteration do not add additional methanol and resuspend the particles.

16. Measure out approximately 10 g of chloroform or solvent of choice on the balance and pour it into each tube and aggitate to disperse the particles. The small amount of residual methanol in the tubes is ok and will help stabilize the suspension.

The protocol yields approximately 10-15 mL of solution containing 5-10 wt% ZnO nanoparticles in a chloroform-methanol solvent suspension. This suspension is stable for several weeks if stored in a cool, dark place.

APPENDIX B

# ZNO TFT PROCESS FLOW

The following pages are an example run sheet for a bottom-gate ZnO TFT process flow. The process described below includes a metal bottom gate. Modifications to fabricate silicon bottom-gate TFTs were made as necessary, but the same general process and mask set were used.

Table B.1: ZnO TFT [Metal backgate] process flow

| Section | Step | Process Title | Description | Process Tool | Time |
|---|---|---|---|---|---|
| 1 | | Wafer MOS Clean | | MOS clean wet bench | |
| | a | Base Clean | 10:1:1 Water:$NH_4OH$:$H_2O_2$ | | 10 min |
| | b | Rinse | 2 rinse cycles | | 5 min |
| | c | Acid Clean | 10:1:1 Water:HCl:$H_2O_2$ | | 10 min |
| | d | Rinse | 2 rinse cycles | | 5 min |
| | e | HF Dip | 10:1 Water:HF | | 10 sec |
| | f | Rinse | 2 rinse cycles | | 5 min |
| | g | Spin Dry | Rinse and dry | | 3 min |
| 2 | | Wet HCl Oxidation | | Tube Furnace B2 | |
| | a | Load | Load wafers | | 5 min |
| | b | Pre-Dep | Temp ramp and gas mixing | | 15 min |
| | c | Deposition | 'Wet HCl Oxide' program | | 30 min |
| | d | Anneal | Post-dep anneal | | 10 min |

*Continued on next page*

Table B.1 – *Continued from previous page*

| Section | Step | Process Title | Description | Process Tool | Time |
|---|---|---|---|---|---|
| | e | Cool-down | Ramp down to 850°C | | 60 min |
| | f | Unload | Unload wafers | | 5 min |
| 3 | | O2 plasma clean | O2 plasma clean | Glenn Asher | 5 min |
| 4 | | Gate Metal Deposition | | SC4500 Evaporator | |
| | a | Load | | | 5 min |
| | b | Pump down | | | 60 min |
| | c | Cr or Ti deposition | 10 nm adhesion layer | | 10 min |
| | d | Mo deposition | 100 nm gate metal | | 15 min |
| | e | Cool down | | | 5 min |
| | f | Vent | | | 5 min |
| 5 | | Gate Metal Patterning | | | |
| | a | Spinning | P10, S1813, 4000 rpm | Area 1 spinners | 30 sec |
| | b | PAB | Resist bake out, 90°C | Hotplate | 60 sec |
| | c | Exposure | Mask 1: ZNO_GATE | Suss MA6 | |

*Continued on next page*

Table B.1 – *Continued from previous page*

| Section | Step | Process Title | Description | Process Tool | Time |
|---|---|---|---|---|---|
| | d | PEB | PEB, 90°C | Hotplate | 60 sec |
| | e | Develop | Develop, AZ 726MIF | Hamatech Developer | 5 min |
| 6 | | Gate Metal Etch | | Oxford 81 | |
| | a | Vent/Load | Vent/Load | | 5 min |
| | b | Run | 20sccm SF6, 20 sccm CF4, 40 mtorr pressure | | 1 min |
| | c | Vent/Unload | Vent/Unload | | 5 min |
| 7 | | Resist Strip | | Resist Strip Hood | |
| | a | Hot solvent bath #1 | | | 5 min |
| | b | Hot solvent bath #2 | | | 5 min |
| | c | Rinse | 2 rinse cycles | | 5 min |
| | d | Spin Dry | Rinse and dry | | 5 min |
| 8 | | Gate Dielectric Deposition | | GSI PECVD | |
| | a | Predeposition | Low Dep rate oxide | | 5 min |
| | b | Deposition | Gate dielectric deposition | | 20 sec |

*Continued on next page*

Table B.1 – *Continued from previous page*

| Section | Step | Process Title | Description | Process Tool | Time |
|---|---|---|---|---|---|
| | c | Clean | chamber clean | | 10 min |
| 9 | | Dicing | | | |
| | a | Spinning | P10, S1813, 4000 rpm | Area 1 spinners | 30 sec |
| | b | PAB | Resist bake out, 90°C | Hotplate | 1 min |
| | c | Dicing | Si blade | KS 7100 Dicing Saw | 10 min |
| 10 | | Resist Strip | | Resist Strip Hood | |
| | a | Hot solvent bath #1 | | | 5 min |
| | b | Hot solvent bath #2 | | | 5 min |
| | c | Rinse | 2 rinse cycles | | 5 min |
| | d | Spin Dry | Rinse and dry | | 5 min |
| 11 | | ZnO Ink Spin Cast | | | |
| | a | Prime squares | 2 mL $CH_2Cl_2$, 1000 rpm | Ober lab spinner | 30 sec |
| | b | Spin ink | 2 mL of ink, 1000 rpm | Ober lab spinner | 30 sec |
| | c | Bake out | 90°C | Hotplate | 60 sec |

*Continued on next page*

Table B.1 – *Continued from previous page*

| Section | Step | Process Title | Description | Process Tool | Time |
|---|---|---|---|---|---|
| | d | Spin ink | 2 mL of ink, 1000 rpm | Spin coater | 30 sec |
| | e | Bake out | 90°C | Hotplate | 60 sec |
| 12 | | ZnO Ink Anneal | | | |
| | a | Plasma clean | Ligand removal, 200 W | Glenn Asher | 2 min |
| | b | Blanket excimer anneal | 75 mJ/cm$^2$ | XeCl excimer laser | 5 min |
| | c | High-power anneal | 200 - 300 mJ/cm$^2$ | XeCl excimer laser | 5 min |
| 13 | | Active Layer Patterning | | | |
| | a | Spinning | P10, S1813, 4000 rpm | Area 1 spinners | 30 sec |
| | b | PAB | Resist bake out, 90°C | Hotplate | 60 sec |
| | c | Exposure | Mask 2: ZNO_ACTIVE | Suss MA6 | |
| | d | PEB | PEB, 90°C | Hotplate | 60 sec |
| | e | Develop | Develop, AZ 726MIF | Hamatech Developer | 5 min |
| 14 | | Active Layer Etch | | | |
| | a | Dilute Al etch | 1000:1, $H_2O$: Al etch | Wet bench | 20 sec |

*Continued on next page*

Table B.1 – *Continued from previous page*

| Section | Step | Process Title | Description | Process Tool | Time |
|---|---|---|---|---|---|
| 15 | | Resist Strip | | Wet bench | |
| | a | Acetone | Acetone dip | | 2 min |
| | b | IPA | IPA dip | | 2 min |
| | c | $N_2$ dry | $N_2$ dry | | 1 min |
| 16 | | Gate Via Patterning | | | |
| | a | Spinning | P10, S1813, 4000 rpm | Area 1 spinners | 30 sec |
| | b | PAB | Resist bake out, 90°C | Hotplate | 60 sec |
| | c | Exposure | Mask 3: ZNO_Via1 | Suss MA6 | |
| | d | PEB | PEB, 90°C | Hotplate | 60 sec |
| | e | Develop | Develop, AZ 726MIF | Hamatech Developer | 5min |
| 17 | | Gate Via Etch | | | |
| | a | BOE etch | 30:1 BOE | Wet bench | |
| 18 | | Resist Strip | | Wet bench | |
| | a | Acetone | Acetone dip | | 2 min |

*Continued on next page*

Table B.1 – *Continued from previous page*

| Section | Step | Process Title | Description | Process Tool | Time |
|---|---|---|---|---|---|
| | b | IPA | IPA dip | | 2 min |
| | c | $N_2$ dry | $N_2$ dry | | 1 min |
| 19 | | Source/Drain Patterning | | | |
| | a | Spinning | P10, S1813, 4000 rpm | Area 1 spinners | 30 sec |
| | b | PAB | Resist bake out, 90°C | Hotplate | 60 sec |
| | c | Exposure | Mask 4: ZNO_METAL | Suss MA6 | |
| | d | PEB | PEB, 90°C | Hotplate | 60 sec |
| | e | Develop | Develop, AZ 726MIF | Hamatech developer | 5 min |
| 21 | | O2 plasma clean | O2 plasma clean | Glenn Asher | 60 sec |
| 20 | | S/D Metal Deposition | | SC4500 Evaporator | |
| | a | Load | | | 5 min |
| | b | Pump down | | | 60 min |
| | c | Ti deposition | 10 nm adhesion layer | | 10 min |
| | d | Al deposition | 100 nm gate metal | | 10 min |

*Continued on next page*

Table B.1 – *Continued from previous page*

| Section | Step | Process Title | Description | Process Tool | Time |
|---|---|---|---|---|---|
| | e | Cool down | | | 5 min |
| | f | Vent | | | 5 min |
| 22 | | Lift-Off | | Wet Bench | |
| | a | Acetone Lift-off | Acetone lift-off | | 8 hr |
| | b | Ultrasonic clean | Ultrasonic clean in acetone | | 1 min |
| | c | IPA | IPA dip | | 2 min |
| | d | $N_2$ dry | $N_2$ dry | | 1 min |
| 23 | | Electrical Testing | I-V and capacitance as necessary | Probe Station | |

## BIBLIOGRAPHY


[1] Zeta potential: An introduction. Malvern Instruments, 2002.

[2] G.L. Allen, R.A. Bayles, W.W. Gile, and W.A. Jesser. Small particle melting of pure metals. *Thin Solid Films*, 144 (2):297–308, 1986.

[3] Babita Baruwati, D. Kishore Kumar, and Sunkara V. Manorama. Hydrothermal synthesis of highly crystalline ZnO nanoparticles: A competitive sensor for LPG and EtOH. *Sensors and Actuators B*, B119:676–682, 2006.

[4] Waldo J. E. Beek, Martijn M. Wienk, Martijn Kemerink, Xiaoniu Yang, and Rene A. J. Janssen. Hybrid zinc oxide conjugated polymer bulk heterojunction solar cells. *Journal of Physical Chemistry B*, 109:9505–9516, 2005.

[5] P.G. Carey, P.M. Smith, M.O. Thompson, and T.W. Sigmon. Polysilicon thin film transistors fabricated at 100 degrees C on a flexible plastic substrate. In IEEE Electron Devices Society, editor, *IEEE Device Research Conference Digest*, volume 55, pages 58–59. IEEE Publication Services, 1997.

[6] P.G. Carey, P.M. Smith, P. Wickboldt, M.O. Thompson, and T.W. Sigmon. Polysilicon TFT fabrication on plastic substrates. In J. Morreale, editor, *International Display and Research Conference*, pages M36–M39. Society of Information Display, 1997.

[7] Yu Chen, Runzhou Yu, Qian Shi, Jingli Qin, and Feng Zheng. Hydrothermal synthesis of hexagonal ZnO clusters. *Materials Letters*, 61:4438–4441, 2007.

[8] Hua-Chi Cheng, Chia-Fu Chen, and Cheng-Chung Lee. Thin-film transistors with active layers of zinc oxide (ZnO) fabricated by low-temperature chemical bath method. *Thin Solid Films*, 498:142–145, 2006.

[9] Joshua J. Choi, Yee-Fun Lim, Mitk'El B. Santiago-Berrios, Matthew Oh, Byung-Ryool Hyun, Liangfeng Sun, Adam C. Bartnik, Augusta Goedhart, George G. Malliaras, Hector D. Abruna, Frank W. Wise, and Tobias Hanrath. PbSe nanocrystal excitonic solar cells. *Nano Letters*, 9:3749–3755, 2009.

[10] Sang-Hyun Choi, Eung-Gyu Kim, Jongnam Park, Kwangjin An, Nohyun Lee, Sung Chul Kim, and Taeghwan Hyeon. Large-scale synthesis of hexagonal pyramid-shaped Zno nanocrystals from thermolysis of Zn-oleate complex. *Journal of Physical Chemistry B*, 109:14792–14794, 2005.

[11] Gregory Philip Crawford. *Flexible Flat Panel Displays*. John Wiley & Sons, Chichester, West Sussex, England; Hoboken, NJ, 2005.

[12] S. B. Fuller, E. J. Wilhelm, and J. M. Jacobson. Ink-jet printed nanoparticle microelectromechanical systems. *Journal of Microelectromechanical Systems*, 11(1):54–60, 2002.

[13] G.K. Giust and T.W. Sigmon. Polysilicon thin film transistors fabricated from laser-processed sputtered silicon films. In IEEE Electron Devices Society, editor, *IEEE Device Research Conference*, volume 56, pages 104–105. IEEE Publication Services, 1998.

[14] Roman Glass, Martin Mller, and Joachim P Spatz. Block copolymer micelle nanolithography. *Nanotechnology*, 14(10):1153, 2003.

[15] Yanghai Gui and Changsheng Xie. A novel simplified method for preparing ZnO nanoneedles via H2O2 pre-oxidation. *Materials Chemistry and Physics*, 93:539–543, 2005.

[16] Gustav F. Haettig and Karl Toischer. Die naturkonstanten des stabilen zinkoxyds. *Zeitschrift fuer Anorganische und Allgemeine Chemie*, 207(3):273–288, 1932.

[17] Saad A. Hasan, Dustin W. Kavich, Sameer V. Mahajan, and James H. Dickerson. Electrophoretic deposition of CdSe nanocrystal films onto dielectric polymer thin films. *Thin Solid Films*, 517:2665–2669, 2009.

[18] B. Hekmatshoar, K. H. Cherenack, S. Wagner, and J. C. Sturm. Amorphous silicon thin-film transistors with DC saturation current half-life of more than 100 years. In *Proceedings of the International Electron Devices Meeting*, pages 1–4, 2008.

[19] Wolfgang H. Hirschwald. Zinc oxide: An outstanding example of a binary compound semiconductor. *Accounts of Chemical Research*, 18(8):228–234, 1985.

[20] R. L. Hoffman, B. J. Norris, and J. F. Wager. ZnO-based transparent thin-film transistors. *Applied Physics Letters*, 82:733–735, 2003.

[21] Hsing-Hung Hsieh and Chung-Chih Wu. Amorphous ZnO transparent thin-film transistors fabricated by fully lithographic and etching processes. *Applied Physics Letters*, 91:013502/1–4, 2007.

[22] Materials Data Inc. IDCC PDF 36-1451. Jade software database, 2012.

[23] Krishna Iyengar. *Modeling Sub-Millisecond Laser Spike Annealing Processes*. PhD thesis, Cornell University, 2012.

[24] Krishna Iyengar, Byungki Jung, Michael Willemann, Paulette Clancy, and Michael O. Thompson. Experimental determination of thermal profiles during laser spike annealing with quantitative comparison to 3-D simulations. *Applied Physics Letters*, 100(21):211915–3, 2012.

[25] Chung Jaewon, J. H. Seunghwan Ko, Nicole R. Bieri, Costas P. Grigoropoulos, and Dimos Poulikakos. Conductor microstructures by laser curing of printed gold nanoparticle ink. *Applied Physics Letters*, 84(5):801–803, 2004.

[26] Anderson Janotti and de Walle Chris G. Van. Fundamentals of zinc oxide as a semiconductor. *Reports on Progress in Physics*, 72:126501/1–126501/29, 2009.

[27] Jin Joo, Soon G. Kwon, Jung H. Yu, and Taeghwan Hyeon. Synthesis of ZnO nanocrystals with cone, hexagonal cone, and rod shapes via non-hydrolytic ester elimination sol-gel reactions. *Advanced Materials*, 17:1873–1877, 2005.

[28] Byungki Jung, Jing Sha, Florencia Paredes, Christopher K. Ober, Michael O. Thompson, Manish Chandhok, and Todd R. Younkin. Sub-millisecond post exposure bake of chemically amplified resists by CO2 laser heat treatment. In SPIE, editor, *Proceedings of SPIE: Advances in Resist Materials and Processing Technology XXVII*, volume 7639, pages 76390L–76390L, 2010. 10.1117/12.848418.

[29] Toshio Kamiya and Hideo Hosono. Material characteristics and applications of transparent amorphous oxide semiconductors. *NPG Asia Materials*, 2:15–22, 2010.

[30] J. A. Kittl, R. Reitano, M. J. Aziz, D. P. Brunco, and M. O. Thompson. Time-resolved temperature measurements during rapid solidification of Si-As alloys induced by pulsed-laser melting. *Journal of Applied Physics*, 73(8):3725, 1993.

[31] Soon Gu Kwon and Taeghwan Hyeon. Colloidal chemical synthesis and formation kinetics of uniformly sized nanocrystals of metals, oxides, and chalcogenides. *Accounts of Chemical Research*, 41:1696–1709, 2008.

[32] R. H. Lamoreaux, D.L. Hildenbrand, and L. Brewer. High temperature vaporization behavior of oxides II. oxides of Be, Mg, Ca, Sr, Ba, B, Al, Ga, In, Tl, Si, Ge, Sn, Pb, Zn, Cd, and Hg. *Journal of Physical Chemistry and Chemical Reference Data*, 16:419, 1987.

[33] Michael Layani, Michael Grouchko, Shai Shemesh, and Shlomo Magdassi. Conductive patterns on plastic substrates by sequential inkjet printing of silver nanoparticles and electrolyte sintering solutions. *Journal of Materials Chemistry*, 22(29):14349–14352, 2012.

[34] Hsin-Ying Lee and Wen-Ming Shien. Investigation of Al-doped ZnO channel layer in ZnO-based transparent thin-film transistors. *Japan Journal of Applied Physics*, 51:026502/1–026502/4, 2012.

[35] Jin-Hong Lee and Byung-Ok Park. Transparent conducting ZnO:Al, In and Sn thin films deposited by the sol-gel method. *Thin Solid Films*, 426:94–99, 2003.

[36] Sul Lee, Sunho Jeong, Dongjo Kim, Sookhyun Hwang, Minhyon Jeon, and Jooho Moon. ZnO nanoparticles with controlled shapes and sizes prepared using a simple polyol synthesis. *Superlattices and Microstructures*, 43:330–339, 2008.

[37] S. V. Mahajan, D. W. Kavich, M. L. Redigolo, and J. H. Dickerson. Structural properties of electrophoretically deposited europium oxide nanocrystalline thin films. *Journal of Materials Science*, 41:8160–8165, 2006.

[38] Siddhartha Mal, J. Narayan, Sudhakar Nori, J. T. Prater, and D. Kumar. Defect-mediated room temperature ferromagnetism in zinc oxide. *Solid State Communications*, 150:1660–1664, 2010.

[39] George Malliaras and Richard Friend. An organic electronics primer. *Physics Today*, 58(5):53–58, 2005.

[40] Stephen T. Meyers, Jeremy T. Anderson, Celia M. Hung, John Thompson, John F. Wager, and Douglas A. Keszler. Aqueous inorganic inks for low-temperature fabrication of ZnO TFTs. *Journal of the American Chemical Society*, 130:17603–17609, 2008.

[41] C. B. Murray, C. R. Kagan, and M. G. Bawendi. Synthesis and characterization of monodisperse nanocrystals and close-packed nanocrystal assemblies. *Annual Review of Materials Research*, 30:545–610, 2000.

[42] Kenji Nomura, Hiromichi Ohta, Akihiro Takagi, Toshio Kamiya, Masahiro Hirano, and Hideo Hosono. Room-temperature fabrication of transparent flexible thin-film transistors using amorphous oxide semiconductors. *Nature*, 432:488–492, 2004.

[43] Milton Ohring. *Materials Science of Thin Films : Deposition and Structure*. Academic Press, San Diego [u.a.], 2008.

[44] U. Ozgur, Ya I. Alivov, C. Liu, A. Teke, M. A. Reshchikov, S. Dogan, V. Avrutin, S. J. Cho, and H. Morkoc. A comprehensive review of ZnO materials and devices. *Journal of Applied Physics*, 98(4):041301–103, 2005.

[45] Bong Kyun Park, Dongjo Kim, Sunho Jeong, Jooho Moon, and Jang Sub Kim. Direct writing of copper conductive patterns by ink-jet printing. *Thin Solid Films*, 515(19):7706–7711, 2007.

[46] Laurence Poul, Souad Ammar, Noureddine Jouini, Fernand Fivet, and Franoise Villain. Metastable solid solutions in the system ZnO and CoO: Synthesis by hydrolysis in polyol medium and study of the morphological characteristics. *Solid State Sciences*, 3:31–42, 2001.

[47] Joerg Puetz and Michel A. Aegerter. Direct gravure printing of indium tin oxide nanoparticle patterns on polymer foils. *Thin Solid Films*, 516(14):4495–4501, 2008.

[48] Jan M. Rabaey. *Digital Integrated Circuits: A Design Perspective*. Prentice Hall, Upper Saddle River, N.J., 1996.

[49] M. N. Rahaman. *Ceramic Processing and Sintering*. M. Dekker, New York, 2003.

[50] Alan Rawle. Basic priniciples of particle size analysis. Malvern Instruments, 1994.

[51] Venugopal Santhanam and Ronald P. Andres. Microcontact printing of uniform nanoparticle arrays. *Nano Letters*, 4:41–44, 2003.

[52] A. E. Siegman. *Lasers*. University Science Books, Mill Valley, Calif., 1986.

[53] Byeong-Hyeok Sohn, Jeong-Min Choi, Seong Il Yoo, Sang-Hyun Yun, Wang-Cheol Zin, Jin Chul Jung, Masayuki Kanehara, Takuji Hirata, and

Toshiharu Teranishi. Directed self-assembly of two kinds of nanoparticles utilizing monolayer films of diblock copolymer micelles. *Journal of the American Chemical Society*, 125(21):6368–6369, 2003.

[54] Suseela Somarajan, Saad A. Hasan, Chinessa T. Adkins, Eva Harth, and James H. Dickerson. Controlled electrophoretic deposition of uniquely nanostructured star polymer films. *Journal of Physical Chemistry B*, 112:23–28, 2008.

[55] Kris V. Srikrishnan. Smart-cut process for the production of thin semiconductor material films, 1999.

[56] V. Subramanian, T. Bakhishev, D. Redinger, and S. K. Volkman. Solution-processed zinc oxide transistors for low-cost electronics applications. *Journal of Display Technology*, 5(12):525–530, 2009.

[57] D. Sung, A. de la Fuente Vornbrock, and V. Subramanian. Scaling and optimization of gravure-printed silver nanoparticle lines for printed electronics. *IEEE Transactions on Components and Packaging Technologies*, 33(1):105–114, 2010.

[58] Joseph Thomas Verdeyen. *Laser Electronics*. Pearson Education, Taipei, 2003.

[59] John F. Wager. Transfer-curve assessment of oxide thin-film transistors. *Journal of the Society for Information Display*, 18:749–752, 2010.

[60] Annabel Wood, Michael Giersig, Michael Hilgendorff, Antonio Vilas-Campos, Marz Liz, Luis M. n, and Paul Mulvaney. Size effects in ZnO: The cluster to quantum dot transition. *Australian Journal of Chemistry*, 56(10):1051–1057, 2003.

[61] A. Zaier, F. O. El Az, F. Lakfif, A. Kabir, S. Boudjadar, and M. S. Aida. Effects of the substrate temperature and solution molarity on the structural opto-electric properties of ZnO thin films deposited by spray pyrolysis. *Materials Science in Semiconductor Processing*, 12(6):207–211, 2009.

[62] E. Ziegler, A. Heinrich, H. Oppermann, and G. Staever. Electrical properties and non-stoichiometry in ZnO single crystals. *Physica Status Solidi (A)*, 66(2):635–648, 1981.